Titre: Title:	Practical Terahertz Waveguides for Advanced Light Management
Auteur: Author:	Tian Ma
Date:	2017
Type:	Mémoire ou thèse / Dissertation or Thesis
Référence: Citation:	Ma, T. (2017). Practical Terahertz Waveguides for Advanced Light Management [Thèse de doctorat, École Polytechnique de Montréal]. PolyPublie. https://publications.polymtl.ca/2475/

UNIVERSITÉ DE MONTRÉAL

PRATICAL TERAHERTZ WAVEGUIDES FOR ADVANCED LIGHT MANAGEMENT

TIAN MA

DÉPARTEMENT DE GÉNIE PHYSIQUE

ÉCOLE POLYTECHNIQUE DE MONTRÉAL

THÉSE PRÉSENTÉE EN VUE DE L'OBTENTION

DU DIPLÔME DE PHILOSOPHIAE DOCTOR

(GÉNIE PHYSIQUE)

JANVIER 2017

UNIVERSITÉ DE MONTRÉAL

ÉCOLE POLYTECHNIQUE DE MONTRÉAL

Cette thèse intitulée

PRACTICAL TERAHERTZ WAVEGUIDES FOR ADVANCED LIGHT MANAGEMENT

présentée par : MA Tian

en vue de l'obtention du diplôme de : Philosophiae Doctor

a été dûment acceptée par le jury d'examen constitué de :

M. GODBOUT Nicolas, Ph. D, président

M. SKOROBOGATIY Maksim A., Ph. D, membre et directeur de recherche

M. PETER Yves-Alain, D. Sc., membre

M. AZANA José, Ph. D, membre externe

ACKNOWLEDGEMENTS

I would like to express my heartfelt gratitude to my supervisor and research director Prof. Maksim Skorobogatiy for his guidance and supports during my Ph.D. study, especially when I struggled in the predicaments. Maksim's help allowed me to pursue successfully my scientific dream, become more mature, and enrich my curiosity.

I would like to thank all my friends and colleagues in Engineering Physics, Ecole Polytechnique de Montreal, Xin Lu, Hang Qu, Jingwen Li, Hichem Guerboukha, Katirvel Nallapan and others. I would like to thank them for the helpful discussions, constructive interactions and mutual support in the past four years. I also would like to thank the technicians in our group, Francis Boutet and Yves Leblanc, for their plenty of technical assistance.

Finally, I wish to thank my parents and Xin for their support during my doctoral study. They have always been understanding and patient, and I could always address to them for the encouragement and support when I needed it.

RÉSUMÉ

Avec la demande croissante de bandes passantes plus larges et de taux de transfert de données plus élevés, l'utilisation des térahertz (THz) pour les communications sans fil a connu un regain d'attention ces récentes années. En raison de ses faibles absorption et dispersion, le gaz est souvent vus comme les meilleurs médium pour transmettre la radiation THz. Aujourd'hui, de nombreux systèmes de communication THz se basant sur propagation à l'air libre ont été développés et étudiés, démontrant des taux de 100 Gbit/s pour des fréquences de porteuses sous 0.6 THz. Cependant, l'application de ces systèmes sont encore limités en raison des défis inhérents posés par une propagation en espace libre, tels qu'une forte dépendance aux conditions atmosphériques, une divergence rapide du faisceau THz (spécialement à basses fréquences) et le besoin de matériel optique distinct et d'alignement parfait. De plus, en raison de la forte directionalité des faisceaux THz, l'accès aux zones partiellement bloquées peutêtre compliqué et requiert des solutions additionnelles de manipulation des THz pour une communication fiable.

D'un autre côté, les guides d'ondes diélectriques offrent des solutions aux limitations d'une propagation à l'air libre. En particulier, la propagation dans les fibres THz scellés permet d'éviter les problèmes de communication liés à l'influence des conditions atmosphériques. De plus, ces fibres sont flexibles et permettent ainsi d'accéder à des zones physiquement obstruées. Finalement, la taille de ces fibres est comparable à la longueur d'onde, permettant des liens de communication compacts. Cependant, aucun système de communication basés sur les fibres n'existe actuellement. Les principales raisons sont les fortes absorptions et la dispersion dans ces guides d'onde.

Au cours de la dernière décennie, plusieurs fibres THz ont été proposées pour réduire les pertes. On peut donc considérer que ce problème est résolu. Cependant, la gestion de la dispersion est encore très peu étudiée dans la littérature. Dans cette thèse, j'explore différents types de guides d'onde diélectriques pour réduire à la fois les pertes et la dispersion dans le spectre des THz.

Premièrement, je présente un guide d'onde THz à cœur creux à bande interdite qui utilise des réflecteurs positionnés suivant une distribution hyperuniforme. La motivation première de ce guide d'onde est d'explorer la possibilité d'utiliser le design à cœur creux qui possède des larges bandes interdites potentiellement plus grandes que celle atteignables avec des structures simplement périodiques. En particulier, nous démontrons théoriquement qu'en utilisant la combinaison des matériaux résine/air à faible contraste d'indice 1.67/1, il est possible de désigner

un guide d'onde désordonné hyperuniforme avec une bande interdite de 90 GHz (21%) centrée à 0.41 THz. Ceci est comparable aux meilleurs records pour ses contreparties périodiques. Nos guides d'onde à cœur creux sont fabriqués en utilisant une impression 3D. Le diamètre du guide d'onde est ~20 mm alors que celui du cœur creux est de ~5 mm. En raison des limitations dans l'impression 3D, la résolution a été limitée à 100 μm, nous permettant d'imprimer des structures avec des ponts plus larges que 200 μm. Les résultats expérimentaux démontrent que les guides d'onde fabriqués ont des larges bandes interdites (jusqu'à 15%) et de faibles pertes de transmission (<0.10 cm^{-1}) dans les bandes interdites.

Ensuite, nous démontrons un nouveau guide d'onde à gradient d'indice spécifiquement désigné pour la gestion de la dispersion dans les THz (THz GI-POF). La fibre est faite de polyéthylène et contient une distribution non uniforme de trous de différentes tailles. Tous ces trous sont sous longueur d'onde, résultant en un indice de réfraction effectif dans le médium. La forte porosité du guide d'onde permet en plus de limiter les pertes d'absorption du matériau. Ces dernières varient de 0.025 cm^{-1} à 0.3 THz jusqu'à 0.15 cm^{-1} à 1.5 THz. La dispersion modale des modes individuels a été réduite sous 1 ps/(THz cm) dans la région d'opération, en raison de l'utilisation de matériaux poreux et dûe à un large cœur. Quant à elle, la dispersion intermodale a été réduite sous 2 ps/(THz cm), en raison du choix d'un profil à gradient d'indice. Finalement, les résultats à la fois numériques et expérimentaux confirment que le THz-GI-POF a des propriétés optiques considérablement supérieures à une fibre de même porosité de même dimension, mais à trous uniformes. Le guide d'onde proposé ouvre la voie vers le design de fibres de large bande à faibles pertes et dispersions.

Finalement, je démontre un guide d'onde THz de Bragg pour la compensation de dispersion dans les liens de communications. Le guide d'onde de Bragg proposé est basé sur un tube de métal creux avec une surface interne périodiquement ondulée. Il est fabriqué à partir d'une résine photosensible en utilisant la stéréolithographie 3D et subséquemment métallisé avec une couche d'argent en utilisant la chimie liquide. Pour ce guide d'onde, un guidage monomode et une dispersion négative pour le mode fondamental HE_{11} sont atteignables proches de la fréquence d'opération de ~140 GHz. Le guide d'onde fabriqué possède une bande de transmission considérable (~7 GHz) pour le mode fondamental et une large dispersion négative (~ -130 ps/(THz cm)) à proximité de 140 GHz, là où le système de communication dans notre laboratoire possède la plus grande puissance et sensibilité de détection. En parallèle, autour de 160 GHz, nous

atteignons également un régime monomode pour la région spectrale de 156 à 162 GHz, avec une dispersion du mode HE_{11} variant entre -1500 ps/(THz cm) à -60 ps/(THz cm).

ABSTRACT

With the demand of wider bandwidths and higher bit rates, the use of terahertz frequencies for wireless communications has experienced a surge of attention in recent years. Due to its low absorption and low dispersion, dry gas has been proven to be the best medium to deliver terahertz radiation. To date, various THz communication systems with carrier frequencies smaller than 0.6THz and data transmission rates of 100Gbit/s have been developed and investigated based on free-space propagation (FSP). However, applications of these THz communication systems are still limited due to inherent challenges posed by the free space propagation modality, such as strong dependence on atmospheric conditions, rapid divergence of the THz beams especially at lower frequencies, and demand of professional alignment and optic hardwares. Additionally, due to strong directionality of the THz beams, wireless communications access to partially blocked areas can be problematic, thus, requiring additional THz steering solutions for reliable communications.

On the other hand, dielectric fibers and waveguides offer solutions to the limitations caused by free-space propagation. Particularly, light propagates through sealed THz fibers, thus, influence of the atmospheric conditions on the communication link quality is minimized. Additionally, THz fibers are flexible, hence, allowing access to even physically obstructed areas. Finally, THz fiber size is typically comparable to the wavelength of light, thus enabling highly compact communication links with small footprint. However, no such waveguide-assisted THz communication system currently exists. The main culprits are high absorption and dispersion of THz waveguides.

In the past decade, various THz fibers have been proposed for low loss guidance, and hence the loss reduction in THz fibers can be considered as a solved problem. However, dispersion management in THz fibers has been rarely studied and remains unsolved. In this thesis, I will explore several types of dielectric waveguides for both loss and dispersion reduction in terahertz frequency range.

First, I present a novel hollow-core terahertz PBG waveguide that uses hyperuniform disordered reflectors. The main motivation of the proposed waveguide is to explore the possibility of designing hollow-core waveguides that feature spectrally broad bandgaps which are potentially superior to those attainable with purely periodic structures. Particularly, we demonstrate theoretically that using a resin/air material combination which offers a relatively low refractive

index contrast of 1.67/1, one can design a hyperuniform disordered reflector exhibiting a 90 GHz (~21%) bandgap centered in the vicinity of 0.41THz, which is comparable to the best record for its periodic counterparts. Hollow core PBG waveguides with the optimized reflector are fabricated using 3D MultiJet printing. The diameter of the fabricated waveguides (reflector size) is ~20 mm, while the diameter of the hollow core is ~5mm. Due to limitations in the 3D printing process that we have used, the resolution was limited to 100μm which allowed us to print structures with bridges thicker than 200μm. Experimental results show that the fabricated waveguides featured relatively wide bandgaps (up to ~15%) and low transmission losses ($<0.10 cm^{-1}$) within their PBGs.

Next, I show a novel graded index porous optical fiber which is specifically designed for the dispersion management in the terahertz spectral range (THz GI-POF). The fiber is made from polyethylene plastic and features a non-uniform array of the variable hole size and hole to hole spacing. All the structural features are in the subwavelength scale, thus resulting in a graded refractive index effective medium. Due to its high porosity, fiber absorption loss is only a fraction of the bulk absorption loss of polyethylene, and in the whole operation range it varies from $0.025 cm^{-1}$ at 0.3 THz to $0.15 cm^{-1}$ at 1.5 THz. Modal group velocity dispersion of the individual modes, also know as individual modal dispersion, has been reduced below 1 ps/(THz·cm) in the whole operational range due to the use of porous materials and the relatively large core size. Meanwhile, intermodal dispersion has been reduced below 2 ps/(THz·cm) due to the choice of the graded index profile. In the end, both experimental and numerical results confirm that THz-GI-POFs have considerably superior optical properties when compared to regular THz porous optical fibers that feature similar geometrical dimensions, however only use a uniform array of holes. The proposed graded index porous optical fibers offer a clear pathway towards designing low-loss, broadband, low dispersion fibers for the THz frequency range.

Finally, I describe a THz waveguide Bragg grating for dispersion compensation in terahertz communication links. The proposed waveguide Bragg grating is based on a hollow core metallized tube with a periodically corrugated inner surface. The proposed waveguide was first fabricated from a photosensitive resin using 3D stereolithography, and subsequently, was metallized with silver microlayers using wet chemistry. For this waveguide, the single mode guidance and negative dispersions for the HE_{11}-like fundamental mode are achievable in the vicinity of the operation frequency of ~140GHz. The fabricated waveguide Bragg grating features a sizable transmission band (~7 GHz) for the fundamental mode and a large negative dispersion (~-130 ps/(THz·cm)) in

the vicinity of 140 GHz, where the terahertz communication system in our lab has highest power and detection sensitivity. Meanwhile, in the vicinity of 160GHz, we also attain a single mode range over the spectral range of 156-162GHz, where the dispersion of the fundamental HE_{11}-mode varies from -1500ps/(THz·cm) to -60ps/(THz·cm).

TABLE OF CONTENTS

LIST OF TABLES

LIST OF FIGURES

LIST OF SYMBOLS AND ABBREVIATIONS

α	Absorption loss coefficient
β	Mode propagation constant
c	Speed of light in vacuum
C_{mn}	Modal coupling by field
D	Dispersion
n_{eff}	Modal effictive refractive index
S_z	Longitudinal flux
υ_g	Group velocity
χ	Hyperuniformity
λ	Wavelength
ω	Frequency
DR	Dynamic range
PC	Polycarbonate
PCs	Photonic crystals
PE	Polyethylene
TE	Transverse electric mode
TM	Transverse magnetic mode
FPG	Free space propagation
GHz	Gigahertz
GVD	Group velocity dispersion
PBG	Photonic bandgap
SEM	Scanning electron microscope
SNR	Signal to noise ratio

THz	Terahertz
mPOF	Microstructured polymer optical fiber
HDPE	High density polyethylene
LDPE	Low density polyethylene
PMMA	Polymethyl methacrylate
PTFE	Polytetrafluoroethylene
PVDF	Polyvinylidene fluoride
CW-THz	Continuous wave terahertz spectroscopy
GI-mPOF	Graded index microstructured polymer optical fiber
THz-TDS	Terahertz time domain spectroscopy

CHAPTER 1 INTRODUCTION

The terahertz (THz) range, with frequencies between 0.1 THz and 10 THz, or wavelengths between 3mm and 30μm, lies between the infrared and microwave bands. The utilization of this spectral range was plagued for a long time owing to the lack of efficient devices for generating and detecting terahertz radiation. In the early 1980s, the emergency of femtosecond lasers and photoconductive antennas made it possible to generate and detect terahertz pulses with picosecond duration [1]. Over the past decades, various terahertz sources [2-7] and detectors [8-11] have been proposed and investigated. The development in the generation and detection of terahertz radiation has greatly advanced the terahertz technology and inspired a great number of research efforts regarding its applications.

Terahertz radiation has great potential in various technological and scientific applications, such as high-bit rate communication [12-13], subwavelength imaging [14-15], chemical and biological sensing [16-17], spectroscopy [18-19], etc. In particular, in the low frequency spectral range where atmospheric transmission windows exist, it is expected that communications with carrier frequencies in the THz range will allow high rate data transmission superior to microwave communication [12]. Specifically, terahertz communication offers a much larger bandwidth which is more than one order of magnitude above the state-of-the-art millimetre-wave communication systems, while the orientation of terahertz communication is also better as terahertz radiation features much shorter wavelengths compared to microwave radiation. Recently, various THz communication systems with carrier frequency smaller than 0.6 THz and data transmission rate up to 100 Gbit/s have been developed and investigated experimentally [20-23].

Considering its low absorption loss and low dispersion in the terahertz regime, dry gas is the most promising medium for THz transmission [24]. As a consequence, most of the current THz communication systems are based on free space propagation (FSP). However, the applications of these THz communication systems are still limited due to inherent challenges posed by the free space propagation (FSP) modality. As terahertz radiation is highly absorbed by water vapour in the atmosphere, and scattered by dusts, clouds, and even atmosphere turbulences, the propagation of THz radiation is strongly dependent on atmospheric conditions. Moreover, THz beams rapidly diverge especially those at the lower carrier frequencies, as well as light-of-sight nature of the links. As a consequence, to realize low divergence THz beams, FSP requires the use of large beam

diameters and focusing optics that can be as big as several tens of centimeter in diameter for even short communication links of several tens of meters. Additionally, due to strong directionality of the THz beams, wireless communications access to partially blocked areas can be problematic, thus, requiring additional THz steering and routing solutions for reliable communications.

On the other hand, dielectric fibers and waveguides offer solutions to the limitations caused by free space propagation. Particularly, when propagating through sealed THz fibers and waveguides, THz radiation is isolated from the surroundings, and hence, influence of the atmospheric conditions on the communication link quality is minimized. Moreover, the majority of THz fibers and waveguides are flexible, allowing us to replace large and cumbersome optical hardwares and navigate THz radiation to even physically obstructed areas. Additionally, the flexibility of THz fibers and waveguides can be further enhanced by various geometrical designs [25]. Finally, THz fibers size is typically comparable to the wavelength of light, thus enabling highly compact communication links with small footprints. However, no such fiber- or waveguide-based THz communication system currently exists. The main culprits are high absorption and dispersion of terahertz fibers and waveguides.

When propagating through a dielectric fiber, the optical signal is invariably affected by both transmission losses and dispersion, and hence rapidly degrade in quality. To analyze the effects of losses and dispersion, I demonstrate the propagation of a terahertz signal with carrier frequency ω_0 in a dielectric fiber with a transmission loss α and a dispersion D. To ease the analysis, I ignore the nonlinear effects in the fiber and assume the fiber is single mode in the vicinity of the carrier frequency ω_0. With the input electric field at $z = 0$ as $E_0(\omega, 0)$, its propagation in the fiber can be written as [26]

$$E(t,z) = \int E_0(\omega, o)\exp[i(\beta z - \omega t)]\, d\omega \tag{1.1}$$

In the vicinity of the carrier frequency ω_0, the modal propagation constant β can be expanded as

$$\beta(\omega_0 + \Delta\omega) = \mathrm{Re}[\beta(\omega_0)] + \frac{\Delta\omega}{v_g} + \frac{\beta_2 \Delta\omega^2}{2} + i\frac{\alpha}{2} \tag{1.2}$$

where $v_g = 1/\beta_1 = (\partial\beta/\partial\omega)^{-1}$ is the modal group velocity, $D = \partial^2\beta/\partial\omega^2$ is the modal dispersion, and $\alpha = 2\mathrm{Im}(\beta)$ is the transmission loss.

Generally speaking, transmission losses result in power attenuation, and, consequently, reduction of the signal to noise ration (SNR). To correct this problem, I estimate the average power at the output end of a fiber-link with $z = L$, which can be given as [26]:

$$\langle P(L)\rangle = \lim_{T\to\infty}\frac{1}{T}\int_{-T/2}^{T/2}|E(t,L)|^2 dt = \langle P_0\rangle \exp(-\alpha L) \tag{1.3}$$

where $\langle P_0\rangle$ is the average power at the input end. Thus, the average output power $\langle P(L)\rangle$ decreases exponentially as the fiber link length L increases. In Figure 1.1(a), I demonstrate the relationship between the losses and the average output power of fiber-links with different lengths. For a fiber-link with a length of 10m, if we need to detect at least 10% of the input power, the maximum transmission loss of the fiber-link should be no bigger than 0.002cm^{-1}. For a typical dielectric THz fiber with a transmission loss of ~0.01cm^{-1}, only ~36% of the input power is left after propagating through a fiber with length of 1m.

On the other hand, dispersion in a fiber-link can chirp the delivered signal, and therefore causes signal distortion and broadens the signal duration. Hence, the achievable data rate of the fiber-link is limited. The relationship between the data rate B, dispersion D, and the maximum transmission distance L_m can be given as follows [26]:

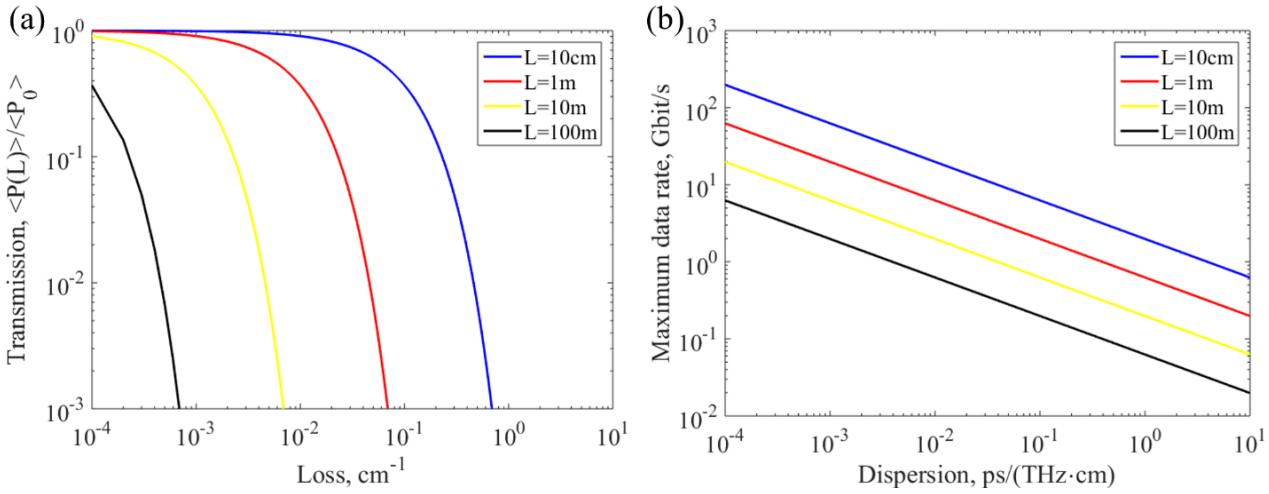

Figure 1.1 (a) The power attenuation caused by transmission losses and (b) the maximum date rate limited by the dispersion for the transmission fiber with length of 10cm (blue), 1m (red), 10m (yellow), and 100m (black).

$$L_m = \frac{1}{16|\beta_2|B^2} = \frac{\pi}{8|D|B^2} \tag{1.4}$$

where β_2 is the group velocity dispersion (GVD) parameter related to the commonly used dispersion parameter D. For a given transmission distance, the maximum data rate is inversely proportional to the square root of the fiber dispersion, as shown Figure. 1.1(b). For a fiber-based transmission link with a length of 10m, to obtain a data rate of 40 Gbit/s, the maximum average dispersion is only 0.04ps/(THz cm). If the link is based on THz plasmonic waveguides whose typical dispersion is only 0.01ps/(THz cm) [26], the maximum transmission distance is only about 20m.

As dry gas offers the lowest absorption for terahertz frequencies, one can minimize the transmission losses of a THz fiber or waveguide by maximizing the fraction of power guided in the gaseous region. Based on this strategy, various THz fibers with low transmission losses (<0.01 cm^{-1}) have been proposed and demonstrated in the past decade. Among these designs, one generally distinguishes subwavelength THz fibers that guide using total internal reflection (TIR) mechanism and hollow core fibers that guide using either photonic bandgap confinement or anti-resonant reflection (ARROW).

However, dispersion management for terahertz communication still remains unsolved. Note that even in the wireless links, dispersion of air at THz frequencies is $D \sim 2.5\times10^{-4}\mathrm{ps}/(\mathrm{THz}\cdot\mathrm{cm})$ [27], thus limiting the 100 Gbit/s wireless link to 400 m. In addition to pulse deformation due to group velocity dispersion, frequency dependent absorption loss due to water vapor will further contribute to pulse deformation. Therefore, while effects of dispersion can be modest in free space links, they are a major limiting factor in waveguide-based interconnects.

In order to counter the dispersion, one can follow two approaches. The first one is minimizing dispersion in THz fibers and waveguides. Most dielectric materials offer almost constant refractive indices in the terahertz frequency range [30]. Hence, dispersions in dielectric THz fibers and waveguides can be reduced by confining THz radiation in a solid core [31-32]. However, the applications of these fibers are limited by their high transmission losses caused by material absorption. Dispersion can also be reduced and flattened by the waveguide's structural design. However, this has rarely been studied in the THz domain.

The other approach to solving the dispersion problem is to insert a dispersion compensator at the end of the link or a dispersion precompensator at the beginning. As the dispersions in free space and most of THz fibers and waveguides are positive, dispersion compensators are generally required to offer large dispersion over a relatively wide frequency range. Moreover, effective coupling with other optical devices and single mode operation in the target frequency range are necessary to ease the implementation of these dispersion compensators. For telecommunications, fiber Bragg gratings, that can effectively cancel the dispersion introduced by transmission fibers with the length of tens of kilometers, have been proposed [33-36]. However, dispersion compensation in the terahertz frequency range is still a challenge.

As a consequence, in order to utilize dielectric fibers in terahertz communication systems, we should minimize both transmission losses and dispersion. In this thesis, I will explore several types of dielectric waveguides for the manipulation of terahertz light. More precisely, I will firstly present a hollow core waveguide featuring hyperuniform reflectors, which can result in sizable bandgaps which are comparable to the best record of its counterparts with periodic reflectors based on photonic crystals. Then, I will demonstrate the design and characterization of a porous fiber featuring an air-hole array with gradually varied diameters and inter-hole separations. This fiber has been proved to be promising for terahertz guidance with both low loss and low dispersion. At last, I will show a periodically microstructured hollow core waveguide which can be used to compensate the positive dispersion of a fiber-based transmission link. To my best knowledge, this is the first time that waveguide-based dispersion compensation has ever been investigated in the terahertz domain. The following paragraphs outline the detailed organization of this thesis:

Chapter 2 begins with a literature review of terahertz fibers with reduced losses. I compare their optical properties based on their guiding mechanisms. In Chapter 2.2, I also review studies on dispersion management, including dispersion flattening and compensation. As dispersion management continues to be a challenge and has not yet been investigated in depth at terahertz frequencies, I will focus on dispersion managing fibers in the visible and infrared range.

Chapter 3 provides the methodology of my study, which follows the procedure of geometrical design based on numerical simulations, waveguide fabrication using different technologies, and optical characterization using both terahertz time-domain spectroscopy (THz-TDS) and terahertz continuous-wave (THz-CW) spectroscopy.

Chapter 4 is based on my paper “3D Printed Hollow-Core Terahertz Optical Waveguides with Hyperuniform Disordered Dielectric Reflectors” published in Advanced Optical Material in 2016. This paper focuses on the study of the utilization of hyperuniform reflectors to produce hollow core waveguides with sizable bandgaps in the terahertz range and includes detailed description of the fabrication and characterization techniques.

Chapter 5 is based on my paper “Graded index porous optical fibers – dispersion management in terahertz range” published in Optics Express in 2015. In this chapter, I present the theoretical and experimental works concerning the management of the intermodal dispersion using a porous fiber in the terahertz range.

Chapter 6 is based on my paper “Dispersion Compensation for Terahertz Communication Using 3D Printed Hollow Core Waveguide Bragg Grating” submitted to Optics Express in 2017. In this chapter, I present the design of a waveguide Bragg grating which can produce a single mode operation range in the vicinity of 140GHz and provide large negative dispersion. The optical characterization of the fabricated waveguide is also presented and discussed.

Finally, a general discussion of the achieved results and future research perspectives are presented.

CHAPTER 2 LITERATURE REVIEW

2.1 Terahertz waveguide with reduced losses

Terahertz radiation can penetrate through a majority of dielectric materials, however, the propagation length is limited by material absorption. For instance, the typical absorption losses of amorphous material suitable for THz fiber fabrication (such as glasses and polymers) are in the range of 0.1-0.3 cm^{-1}, leading to cm-scale maximum propagation lengths. As the lowest absorption loss for THz wave occurs in dry gases, the transmission losses of the THz fibers can be reduced significantly by maximizing the fraction of the THz power guided in the low-loss gas. Based on this strategy, various THz waveguides and fibers have been proposed. According to the guiding mechanics, these waveguides/fibers can be divided into three categories, including index dielectric guiding waveguides/fibers, hollow core dielectric waveguides/fibers, and hybridized waveguides/fibers.

2.1.1 Index guiding dielectric waveguides/fibers

The simplest optical fibers are step index fibers, which comprises of a dielectric core surrounded by a lower refractive index medium. For these fibers, optical light is confined in the dielectric core owing to the total internal reflection, and hence, these fibers can also be named as index guiding fibers. However, the losses of such fibers are almost the same as that of the material absorption. In the optical domain, reducing the fiber core size to the subwavelength scale has proven to be an efficient method for low-loss guidance [37]. The first subwavelength fiber in the THz regime was demonstrated by Chen el al [38]. They used a polyethylene (PE) wire with a diameter of 200 μm for THz guidance. As the guided model field extends far into the air cladding, the attenuation constant of this fiber can be reduced to 0.01cm^{-1}. Later, researchers [39-42] discovered that introducing an array of deeply subwavelength holes into the core of a subwavelength fiber enabled further reduction of both the absorption and bending losses, and broadening of the transmission bandwidth.

In subwavelength fibers, the propagation loss is reduced due to low modal confinement in the lossy, solid-core region. However, the mode of subwavelength fibers is significantly affected

by its environment thus preventing direct manipulation of such fibers. In order to solve this problem, Roze *et al.* [43] proposed the suspension of the subwavelength cores inside of polymer tubes. The presence of the outer cladding provides good protection for the guided mode, thus reducing sensitivity to environmental changes. Because of weak confined model fields, this type of subwavelength fiber has great potential for bio-sensing applications [44]. Nevertheless, the application of subwavelength fibers in terahertz communications is still limited by their significant group velocity dispersions (GVDs) as these fibers typically operate in a frequency range where the guided mode confinement changes dramatically from weak confinement (high presence in the gaseous cladding) at low frequencies, to strong confinement (high presence in the solid core) at high frequencies.

Table 1: The comparison between different types of subwavelength fibers for terahertz guidance.

Waveguide type	Schema	Material	Core size	Loss	Ref.
Solid subwavelength fiber		PE	200μm	$<10^{-2}$cm^{-1} at 310-360GHz	[38]
Porous subwavelength fiber	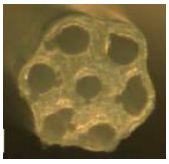	LDPE	700μm	0.022cm^{-1} at 234GHz	[40]
Suspended solid-core subwavelength fiber	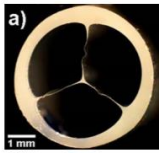	LDPE	150μm	<0.02cm^{-1} at 0.28-0.48 THz	[43]
Suspended porous-core subwavelength fiber	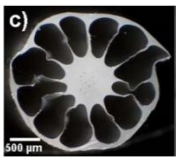	LDPE	900μm	<0.15cm^{-1} at 0.1-0.4THz	[43]

2.1.2 Hollow core dielectric waveguides/fibers

Besides the fibers mention above, low-loss guidance in the terahertz domain can also be achieved by guiding light in a gaseous core. Based on this strategy, various waveguides utilizing different guiding mechanisms, including photonic bandgap (PBG) guidance and anti-resonant reflective guidance, have been proposed.

2.1.2.1 Photonic bandgap waveguides

Typically, hollow core PBG waveguides feature a gaseous core surrounded by dielectric periodic reflectors formed by periodic refractive index variation. Due to the photonic bandgap effects, at frequencies within the photonic bandgaps, optical light cannot pass though the dielectric reflector, and the majority of power is guided as the core guided mode with ultralow losses. Hence, frequency dependent photonic bandgaps are formed. Within these bandgaps, as terahertz radiation is confined in the gaseous core, the transmission losses are negligible. Moreover, the transmission properties of these waveguides, including the transmission bands and dispersion characters, can be tuned simply by varying the geometrical parameters of the reflector. Various hollow-core PBG fibers based on the photonic bandgap effect have been proposed for terahertz guidance with low-losses. These fibers can be sorted into two categories, holey fibers and Bragg fibers, depending on their reflector structure.

In the case of holey fibers, the reflector in the cladding is usually formed of a 2D photonic crystal with periodically positioned holes. Only in the bandgap of the reflector can modes be confined and propagate through the core. These fibers are proposed primarily for guidance in the optical domain [45-46]. However, these fibers suffer from the relative high confinement losses due to the infinite layers of holes in the cladding. When expanded into the terahertz domain [47-51], the modal leakage does not harm the guidance of light. Vincetti *et al.* [47] showed that a holey reflector with only three layers of air-holes was good enough to confine the majority of power in the core, and produced a confinement loss of 0.0002 cm^{-1} which is negligible compared to material absorption (0.01cm^{-1}) in the same frequency range. Owing to the PBG effect, various periodic lattices such as, triangular [47-49], rectangular [50], and honeycomb [51-53], to name but a few., can be used as the reflector of holey fibers. The key parameter of these periodic lattices is the air filling fraction, or the air-hole diameter to hole-to-hole pitch ratio (d/Λ), in the cladding, which

determines both the spectral position and width of the bandgaps. Holey PBG fibers with high air-filling fractions are usually designed for wider bandgaps.

Bragg fiber is another type of hollow PBG fibers used for terahertz guidance. It exploits resonant reflection from a periodic multilayer reflector with circular symmetry surrounding the hollow core region. To produce photonic bandgaps, hollow core Bragg fibers usually feature alternative layers to achieve a periodic variation of the refractive index in the radial direction. The simplest Bragg reflector can be formed by repeating alternate concentric layers of two different polymers. A hollow core Bragg fiber with this kind of reflector was first theoretically demonstrated by Skorobogatiy *et al.* [54] in 2007. The transmission of losses less than $0.2cm^{-1}$ over a wide frequency range (1-3THz) was accomplished using an all-polymer multilayer structure (PVDF/PC) as the reflector. However, one should note that the wide, low-losses transmission range was attributed to the relatively large refractive index contrast between PVDF and PC, particularly in the frequency range of 0.6-2.0THz where the refractive index of PVDF is even smaller than that of the air. The proposed waveguide is not easily fabricated in the lab due to the differing thermal and mechanical properties of PVDF and PC. It is hard to find dielectric materials with both large refractive index contrast and similar thermal and mechanical properties, which are required by the fiber drawing technology [55-56]. To solve this problem, another type of all-solid Bragg reflector was proposed by using the same material with different dopants [57-58]. In [58], the authors proposed a hollow core Bragg fiber using the PE and TiO_2-doped PE based multilayer structure. Through the control of dopant concentration, the refractive index contrast in the Bragg reflector can easily be tuned. Low transmission losses below $0.1cm^{-1}$ are attainable in such fibers.

As with all-solid Bragg fibers, several techniques using porous Bragg fibers have been reported, which involve the introduction of rings of porous material. The simplest porous Bragg fiber was fabricated by introducing air-holes to the cladding [59]. The proposed porous Bragg reflector consisted of five circular rings of air-holes. The presence of these air-holes reduced the effective refractive index of porous layers, and Bragg reflections occur at the interface between layers with and without air-holes. Using this fiber, a low transmission loss of $\sim 1.1cm^{-1}$ was attained over a range of 0.8-1.4THz. To enlarge the PBG width, hollow core Bragg fibers with solid/randomly porous multilayers [60] and cob-web structures [61-62] were investigated in the terahertz range. For these fibers, a high refractive index contrast was realized due to ultra-high porosities in the cladding, thus allowing low-loss transmission over a broad spectral range. For

example, in the case of a hollow core Bragg fiber with a cob-web reflector, the transmission losses of the fundamental mode were theoretically predicted to be as low as $< 1.9\times10^{-5}$cm^{-1} over 0.3-4.3THz [61]. However, Bragg fibers with ultra-high porosities in their cladding are not easily fabricated, as their structures are extremely fragile.

2.1.2.2 Anti-resonant reflecting fibers

In addition to photonic bandgap guidance, anti-resonant reflecting guidance can also be used to confine terahertz radiation within a core having low refractive index. For fibers based on anti-resonant (ARROW) guidance, both the core and the cladding can support guided modes, and the core-guided modes are guided in the core region owing to the anti-resonant Fabry-Perot (F-P) effect [63]. The simplest ARROW fiber is a dielectric pipe with a thin wall [64], where the thin dielectric wall acts as a Fabry-Perot resonator. Transmission with high modal confinement in the core region and ultra-low transmission losses occurs at the anti-resonant frequencies of the F-P reflector. ARROW guidance in the terahertz domain was first demonstrated by Lai *el al.* [65], where PMMA pipes with differing wall thicknesses were characterized. The experimental results confirmed that transmission bands, corresponding to the frequencies between two adjacent resonant frequencies, can be tuned by varying the refractive index and thickness of the dielectric wall.

The Kagome hollow core waveguide is another waveguide based on ARROW guidance. The reflector structure of this waveguide gives the appearance of a kagome structure, which is a traditional Japanese woven bamboo pattern. Although both the core and cladding support guided modes, core-guided modes are prevented from coupling to the cladding due to the anti-resonant reflecting of the Kagome lattice in the cladding [66-67]. Compared to their counterparts using PBG reflectors, Kagome hollow core waveguides can have a much wider transmission band. However, transmission losses within bandgaps are much higher than that of hollow core PBG fibers.

The first Kagome hollow core waveguide for THz guidance was experimentally demonstrated by Lu *et al.* [68]. The waveguide reflector was fabricated by packing Teflon tubes in the hexagonal closest packed arrangement around a gaseous cavity. The outer diameters of the fabricated waveguides were in the cm-scale. A low attenuation loss of less than 0.002cm^{-1}, which is a negligible loss when compared to the material absorption of Teflon, was attainable for the proposed waveguide at 0.77THz. Moreover, the bandgap guidance was shown to be adjustable by

linearly scaling the whole waveguide size, including the inner diameter of the hollow core and the outer diameter of the whole waveguide. Hollow core Kagome waveguides with reduced sizes were also proposed by Anthony *et al.* [69]. A preform with an outer diameter of 80mm was first fabricated by stacking PMMA tubes in a triangular lattice, and then stretched into Kagome waveguides with the desired outer diameters of 5 mm and 6.8 mm, respectively. In this experiment, attenuation losses 20 times lower than that of the material absorption were achieved over a wide range of frequencies, 0.75-1.0 THz and 0.6-1.0THz, respectively.

Furthermore, numerical investigations [70-71] showed that both the attenuation losses and bandgaps could be tailored through the adjustment of geometric parameters of the waveguide. Specifically, the attenuation losses can easily be reduced by increasing the size of the hollow core, while reducing the thickness of the struts in the cladding can not only broaden the bandgap width but also flatten the dispersion relation of guided modes with bandgaps.

Both the photonic bandgap guidance and anti-resonant reflecting guidance can be used to reduce the transmission losses effectively. However, the potential applications of these hollow core fibers are limited by their own inherent drawbacks. To begin with, as we can see in Table 2, most of these fibers have large dimensions, rendering them inflexible. However, transmission losses are inversely proportional to the core size as $\alpha \sim d_{core}^{-3}$ where d_{core} is the core diameter [78]. Thus, a relative large core is necessary for low-loss transmission. A large core size would also lead to multimode guidance, and consequently, the intermodal interactions, such as modal anti-crossing and intermodal dispersion, would be pronounced.

Table 2 The comparison between different types of hollow core fibers for terahertz guidance.

Waveguide type	Reflector type	Schema	Material	Core size	Loss	Ref.
Holey PBG fibers	Hexagonal lattice with circular holes	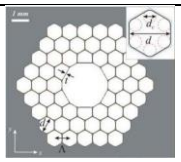	HDPE/air	292μm	~0.022 at 1.53THz for d/Λ=0.93;	[48]
	Rectangular lattice with inflated holes	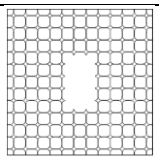	Teflon/air	840μm	<0.04cm^{-1} at 1.65-1.95 THz	[50]

	Honeycomb lattice	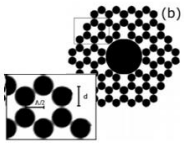	Topas/air	~1mm	~0.058cm^{-1} at 0.98THz	[52]
Bragg fibers	All-solid Bragg reflector	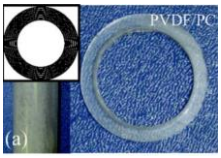	PVDF/PC	~1mm	<0.02cm^{-1} at 1-3 THz	[54]
	All-solid Bragg reflector with doped polymer	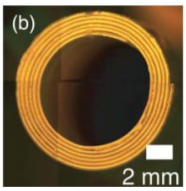	PE/PE with TiO_2 dopants	6.63mm	<0.042cm^{-1} at 0.69THz	[57]
	Bragg reflector with porous layers	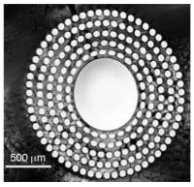	PMMA	2mm	<1.1cm^{-1} at 1.1-1.6 THz	[59]
	Bragg reflector with randomly porous layers	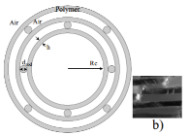	PE/air	6.73mm	<0.028cm^{-1} at 0.82THz	[60]
	Bragg reflector with Cob-web structure	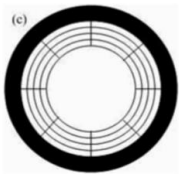	HDPE/air	16mm	5.84×10^{-5}cm^{-1} at 0.55THz	[61]
ARROW fibers	Tubes with thin dielectric walls	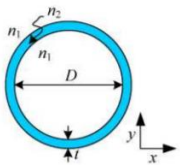	Teflon	9mm	0.0008cm^{-1} at 375GHz	[65]
	Kagome fibers with thick struts	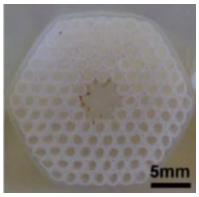	Teflon/are	5mm	0.002cm^{-1} at the 770GHz	[68]

	Kagome fibers with thin struts	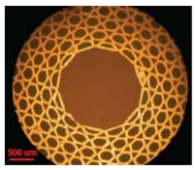	PMMA/air	2.2mm	0.6 cm^{-1} at 0.65-1.0 THz	[69]
	Tube lattice fiber	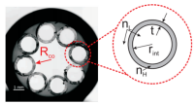	PMMA/air	1.62mm	<0.01cm^{-1} at 0.78-0.90THz	[72]

2.1.3 Hybrid waveguides/fibers

The earlier forms of THz waveguides were metallic in nature with a circular or rectangular hollow core [72-74]. However, these waveguides suffered from very high transmission losses due to high Ohmic losses in metals, which is caused by the fact that electric radiation does not vanish entirely on the metal/air interface, but penetrates into the metal by several nanometers (also known as the *skin effect*). Thus, the typical transmission loss of a metallic hollow core waveguide is in the scale of 1 cm^{-1} [72], not to mention their high dispersion close to cut-off frequencies.

Current research [75-81] shows that the transmission losses of metallic hollow core waveguides can be reduced by adding a thin dielectric layer on the inner surface of these metal waveguides. Apart from the reduced losses, these dielectric-coated waveguides support two modes with low-loss characteristics, the hybrid HE_{11} mode or the transverse TE_{01} mode [76,78,82]. Moreover, the dominant mode can be selected through the geometric properties of the waveguide, include the core size and the coated layer thickness [76]. For instance, when the coated dielectric layer is thick (~10 μm), the HE_{11} exhibits a lower loss, while the TE_{01} mode is suppressed. Conversely, in the waveguide with a dielectric layer of several micron or even thinner, the TE_{01} mode is less lossy, while the HE_{11} mode is restrained.

In addition to these metallic hollow core waveguides with dielectric coating, various waveguides based on metal wires have been proposed for low-loss guidance in the terahertz domain. Such guidance was firstly proposed based on a stainless steel wire with a diameter of 0.9mm, with which both low loss (<0.03cm^{-1} over the frequency range of 0.25-0.75THz) and negligible group velocity dispersion were realized [83]. However, as the fundamental mode in single-wire- based waveguides is radially polarized, it is very difficult to be excited with the

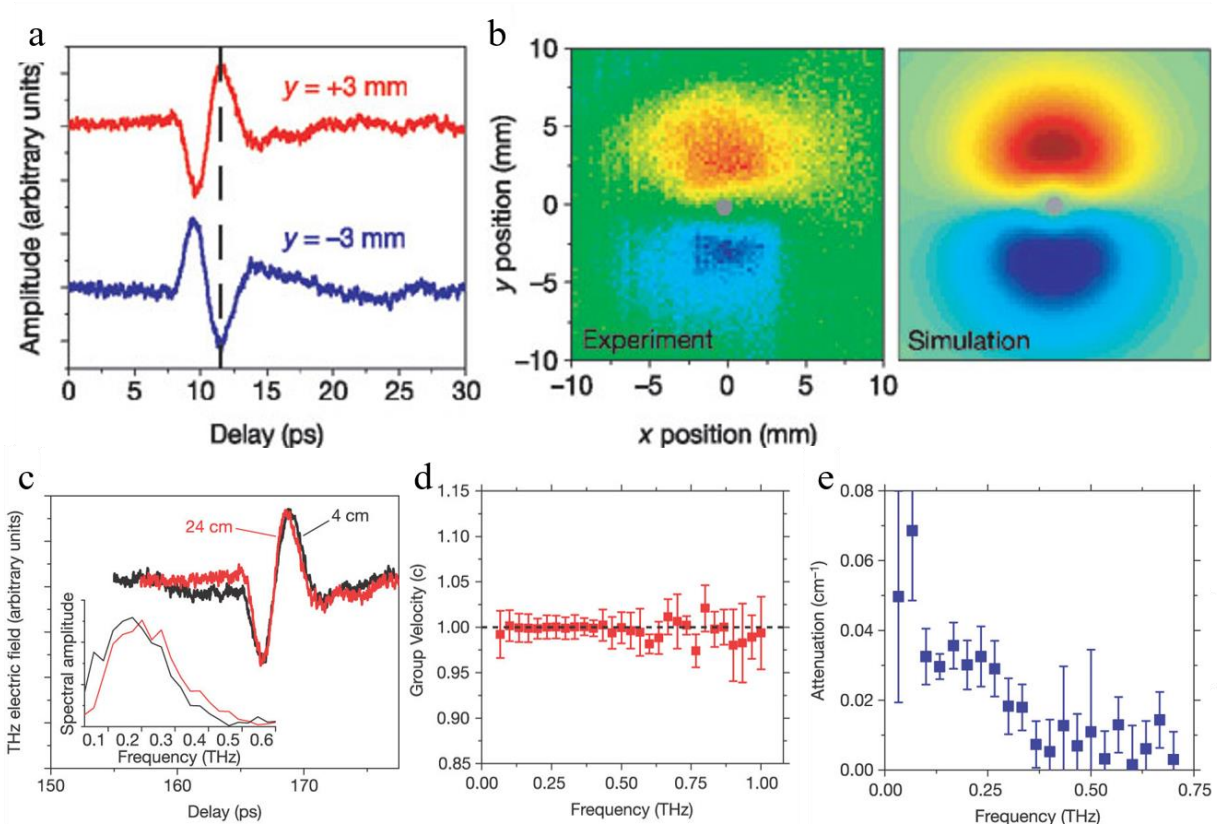

Figure 2.1 (a) Time-domain electric field waveforms detected with the receiver 3mm above and 3mm below the waveguide. (b) and (c) Experimentally mapped and numercial calculated spatial profile of the electric field obtained by moving the THz receiver in a plane perpendicular to the waveguide axis. (c) THz waveforms measured after 4 cm (black) and 24 cm (red) of propagation distance along the wire. (d) Group velocity of the propagating mode as a function of frequency. (e) The electric field amplitude attenuation coefficient of the propagating mode as a function of frequency. Reprinted from Ref [83].

linearly polarized THz light produced by photoconductive antennas. To make matters worse, terahertz guidance along single wire waveguides suffers from enormous bending losses due to poor modal confinement [84].

To overcome these difficulties, THz guidance along two parallel metal wires was investigated [85-92]. In these waveguides, the fundamental mode is linearly polarized along the line connecting the two wires, which allows the direct excitation of the guided mode with a majority of THz sources. Also, as terahertz radiation propagates through the air-gap between the two wires, the modal confinement of these two-wire-based waveguides are enhanced, and hence the bend

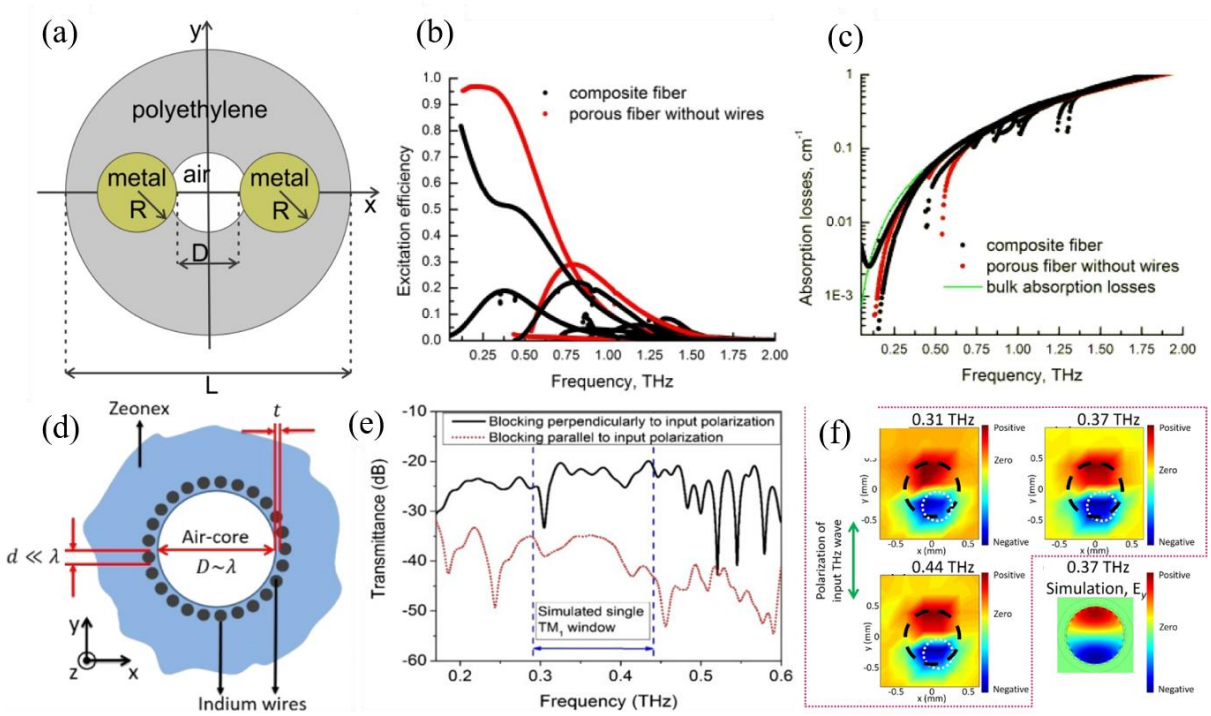

Figure 2.2 (a) Schematic of a composite fiber featuring two metal wires in a three-hole cladding. (b) Excitation efficiences and (c) absorption losses of modes guided in the two-wire-waveguide. Reprinted from Ref. [88]. (d) Schematic of waveguide with metal wire-based cladding. (d) Comparison of normalized transmissions measured by two configurations. Black solid curve and red dots are measured with the waveguide input-end face half-blocked perpendicularly and parallel to the polarization of the input THz wave, respectively. (e) Normalized near-field modal profiles of fabricated waveguide measured at frequencies of 0.31THz, 0.37THz and 0.44THz, and the simulated modal profile at 0.37THz. Reprinted from Ref. [95].

losses, as well as the modal leakage, are suppressed. Moreover, the characteristics of the guiding modes are dependent on the waveguide geometry, in particular, the size of the air-gap between two wires. When the displacement of these two wires is comparable to the wavelength of guided light [90], plasmonic modes are excited because of the presence of metal wires, and the dielectric cladding functions as a mechanical support. When the air-gap between the two wires is much bigger than the wavelength of guided light [93], the fundamental mode become a HE_{11}-like mode supported by ARROW guiding. In this case, the dielectric cladding of the two-wire-based waveguide works as an ARROW reflector, just as the thin-walled dielectric tubes shown in Section

1.1.2, while the metal wires are used to prevent the guided light from dispersing into the dielectric cladding with high absorption.

Apart from these two-wire-based THz waveguides, hollow core waveguides featuring wire metamaterial-cladding were also proposed to guide THz radiation [95-98]. Owing to its extreme anisotropy, uniaxial metamaterials reflects transverse magnetic (TM) waves and transmits transverse electric (TE) waves. As a result, hollow core waveguides, produced through the arrangement of wire metamaterials in the cladding, only support TM mode, which halves the number of guided modes available and enlarges the single mode range. Based on this principle, Li *et al.* [97] proposed a metamaterial-based hollow core waveguide by embedding indium wires in the cladding. The aforementioned waveguide supports single mode (TM_1) guidance over a frequency range of 0.29–0.44THz, and the transmission losses within the single mode range have been experimentally confirmed to be as low as ~0.06cm^{-1}.

2.2 Optical-fiber-assisted dispersion management

To date, various dielectric waveguides have been proposed for low-loss guidance in the terahertz range. However, dispersion continues to be a challenge. Some fibers with reduced losses, such as subwavelength fibers, even make the dispersion problem worse. Other fibers, such as the metal wire and Kagome fibers, support simultaneously low-loss and low-dispersion guidance. However, due to their own deficiencies, such as the poor coupling of SPP modes of metal wires and the brittle structure of Kagome fibers, the use of these fibers is still problematic. However, in the visible and infrared regimes, dispersion management has been investigated in-depth and various remedies employing the assistance of optical fibers have been reported. In fact, occupying a position adjoining visible and infrared light in the electromagnetic spectrum, the terahertz field often borrows the ideas and methods already implemented in the optical domain. In this section, I will review some notable examples of optical fibers for dispersion management in the visible and infrared regimes, which may be adequate for similar applications in the terahertz range. In the following paragraphs, I will classify these fibers into two categories based on their functions, including dispersion flattened fibers and dispersion compensating fibers.

2.2.1 Dispersion reduced fibers

For optical fibers, dispersion represents a broad class of phenomena related to group velocity variation of the guided electromagnetic wave, including frequency-dependent material dielectric constants, frequency-dependent group velocity, and group velocity difference between different modes. Based on these mechanisms, the different types of dispersion can be distinguished as material dispersion, waveguide/individual dispersion and intermodal dispersion. In the terahertz regime, the majority of dielectric materials suitable for waveguide manufacture, such as most polymers and silica, feature frequency-independent dielectric constants, resulting in negligible material dispersions. Thus, in this part, I will place a greater emphasis on waveguide dispersion and intermodal dispersion management.

Waveguide dispersion, also known as group velocity dispersion (GVD), is a phenomenon behind the frequency-dependent group velocity (v_g). This term can also be defined by the derivative of the inverse group velocity with respect to the angular frequency, namely

$$\mathrm{GVD} = \frac{\partial}{\partial \omega}\frac{1}{v_g} = \frac{\partial^2 \beta}{\partial \omega^2} \tag{2.1}$$

where β is the modal propagation constant. As the modal field distribution intensively impacts the value of β, we can expect flattening waveguide dispersion based on the geometric design of the waveguide. With this in mind, various optical fibers have been proposed for providing tiny (near-zero) and ultra-flattened dispersion in a broadband spectral range. Among these fibers, the solid-core photonic crystal fiber (PCF) is the most promising one.

Unlike the hollow core photonic crystal waveguides shown in Section 2.1.2, by introducing a solid defect to the center, the solid-core photonic crystal fibers guide optical light using index guiding based on the total internal reflection (TIR) [99-100]. In these fibers, optical light is confined in the solid core, and isolated from the outmost air-hole-layers and surrounding environments by the first layers of air-holes. The geometry of the air-holes in the cladding is not essential to the confinement of light being guided in the core region, but can be used to modify the characteristics of guided modes.

Using this strategy, various photonic crystal fibers (PCFs) have been proposed to manage waveguide dispersion. In these PCFs, the dispersion can be flattened or shifted by simply changing

the ratio of air-hole diameter to inter-hole distance (d/Λ) [101-103]. Also, by using air-hole arrays of varying diameters [104-106], or by introducing defects in the vicinity of the solid core [107-108], the dispersion can also be flattened.

In fact, the aforementioned method has already been executed in the terahertz range. Nielsen *et al.* [31] exploited the geometry of PCF in the THz frequency regime and reported a polymer (Topas® COC) PCF for terahertz guidance, which has a signal mode over a wide frequency range. Simulation results showed that the dispersion of the fundamental mode was flattened and close to zero in the frequency region of 0.6-1.4 THz. They demonstrated experimentally the dispersion can be easily managed by simply changing the area of the core region and the porosity of the cladding. However, as the THz radiation is guided in the solid core, the transmission loss of the proposed THz PCF was relatively high at 0.42 cm^{-1}. A high transmission loss of this value limits the application of the proposed PCF in terahertz communications.

Besides waveguide dispersion, intermodal dispersion, which is predominant in multimode fibers [109], should also be reduced and flattened. Intermodal dispersion is caused by different group velocities of guided modes. With different velocities, these modes have different travelling time in the guided fiber, leading to the temporal broadening of the optical signal, and hence, reduction of the data rate. In the optical domain, optical fibers with radial graded index profile along the radial direction offer a good solution to this challenge.

In graded optical fibers, the core refractive index decreases from its maximal value at the core center as a certain power ($n(r) \sim n(0) - \alpha r^2$) of the distance. As a result, intermodal group velocity dispersion can be dramatically reduced by artificially controlling the light trace in these fibers. The first graded index optical fibers were composed of silica fibers, and fabricated using the doping method [112] or the photowritten method [114]. Since the 1990s, polymer-based graded index optical fibers have been extensively studied for reducing intermodal dispersions and for their applications in communications [112-115]. Akimoto *et al.* [115] reported the fabrication and experimental investigation of the doped PSt-based GI-POFs. The graded refractive index distribution was achieved by controlling the radial dopant concentration. The authors confirmed that this fiber has a high bandwidth (4.4 GHz at 655 nm with fiber length of 50m) and low attenuation (166-193 dB/km at 670-680 nm) and can be used for home networks. Non-uniformly distributed geometrical features, such as non-uniform air-hole arrays, can also be used realize

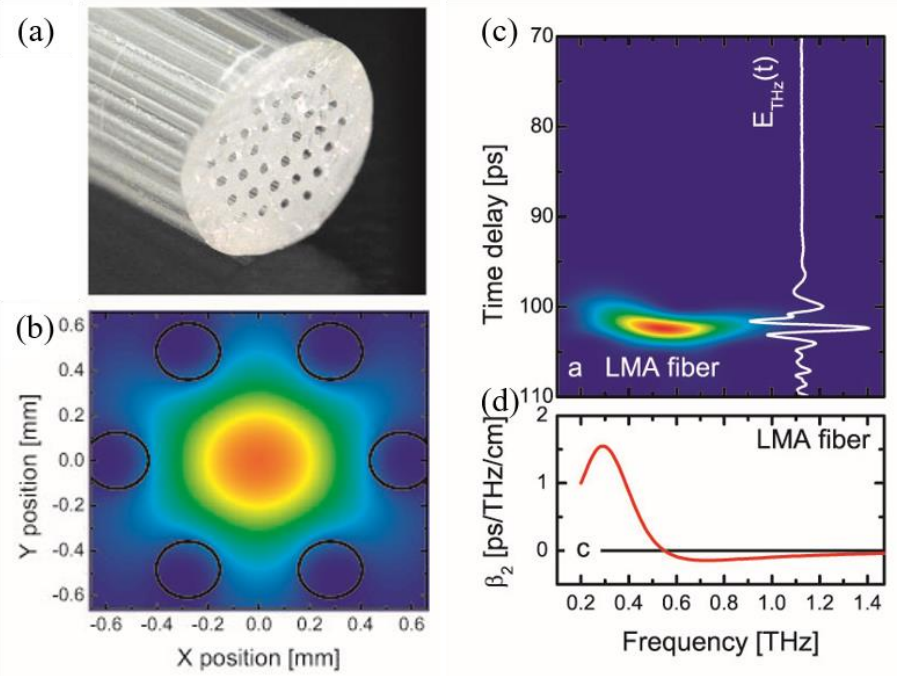

Figure 2.3 (a) Photograph and (b) calculated fundamental guided mode structure at 1 THz of the photonic crystal fiber. Spectrogram and measured temporal profile of the THz pulse after propagation through the fiber are presented in (c) and (d). Reprinted from Ref [31].

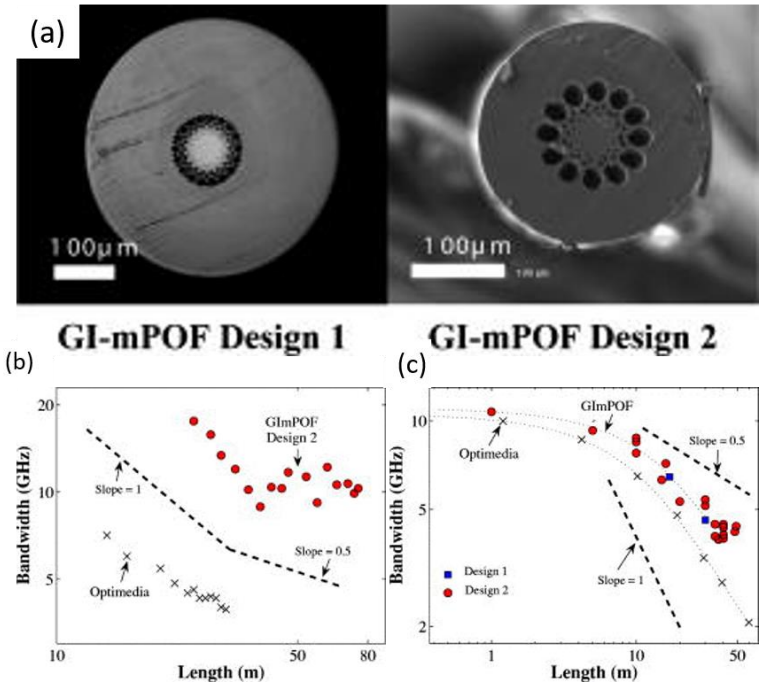

Figure 2.4 (a) Micrographs of GImPOF design 1 (left) and design 2 (right). (b) and (c) Length dependence of the bandwidth measured using sources with linewidth of 3.5nm and 0.01nm, respectively. Reprinted from Ref [106].

variable refractive index profiles in the fiber core. In [116], R. Lwin *et al.* reported another type of graded index fiber with a graded index profile obtained by porous cladding with judiciously positioned air holes of variable diameters. They called this fiber GI-mPOF. They demonstrated experimentally that the bandwidths of the proposed GI-mPOF were much wider than those of the commercial GI-POF.

However, these designs cannot be directly implemented for terahertz guidance. The application of these designs in the terahertz domain is hindered by high material absorptions, which would worsen by introducing dopants to the polymers [57]. Meanwhile, the fiber size would also be problematic. If we use these designs by simply scaling the fiber geometries with respect to the wavelength of guided light, the corresponding fibers used for terahertz guidance would be clumsy and rigid.

2.2.2 Dispersion compensation fibers

Although both waveguide dispersion and intermodal dispersion can be minimized and flattened through various methods, the remaining dispersion would remain unbearable for long distance transmission. Thus, dispersion cancelling, or dispersion compensation, is required for applications in moderate- or long-distance communications.

In optical domain, the first dispersion compensated fiber system was realized by using step index fibers [117]. For a step index fiber, both positive and negative dispersion are achievable by simply varying the fiber geometry (core size and numerical aperture). Based on this principle, Lin *et al.* [117] used two distinct single mode fibers with judiciously chosen core sizes and lengths. Typically, the first fiber is a transmission fiber of long length and of relatively low positive dispersion, while the second one is a dispersion compensating fiber of short length and of high negative dispersion. Using this strategy, the dispersed pulse can be compressed to its original form. Similarly, a majority of dispersion compensation fibers in optical domain feature large dispersion with a sign opposite to that of the transmission fibers, such as dual core fibers based on the modal anti-crossing [118-120], higher order modes fibers operated near their cut-off frequencies [121-123], and even SOI-based slab waveguide [124-125]. However, the implemention of these designs in the terahertz domain is limited by their complex structures, as well as high absorption losses. In

what follows, I review other fiber/waveguide-based dispersion compensation systems with potential for applications in terahertz domain, including photonic crystal fibers, hollow core Bragg fibers and fiber Bragg gratings.

2.2.2.1 Photonic crystal fibers

Photonic crystal fibers (PCFs) have shown great capacity of managing dispersion in the optical domain. As well as flattening dispersion, photonic crystal fibers can also be used for dispersion compensation. These dispersion compensating PCFs can be divided into two categories based on their cladding geometry.

The first type of dispersion compensating PCF is proposed based on the dual-core fiber. For these PCFs, air-hole-arrays with particularly arranged air-holes and defects were used to obtain a configuration equivalent to dual-core fibers. Using this technique, two guides are formed at the central solid core and the cladding containing defects. In the proximity of certain wavelengths λ_0, core-guided modes hybridize with the defect modes and eventually "transform" into the defect-guided modes, and vice versa. In two sides of λ_0, both positive and negative dispersion with large value can be obtained. The value of the dispersion D and the phase matching wavelength λ_0, can be tuned by changing the air-hole diameters (d) and hole-to-hole spacing (Λ). Using this strategy, Gerome *et al.* [126] firstly proposed a dual-core-PCF by introducing a layer of air-holes with smaller diameter into the cladding with perfectly periodic air-hole arrays, which functioned as defects, and were used to for guiding in cladding. A considerably large negative dispersion of -2200ps/(nm km) was attained at 1550nm. Apart from the above-mentioned PCFs, various dispersion compensating PCFs have been proposed based on diverse cladding and defect designs [127-131]. Among these PCFs, the largest negative dispersion, which can be as large as -25,000ps/(nm km), was achieved numerically by Zhao *et al.* [127]. In practical terms, the main problem with these dispersion compensating PCFs is a relatively low coupling efficiency which is a consequence of the mismatch between the modal fields of regular circular core fibers for transmission and the dual core PCFs needed for the dispersion compensation.

Another type of dispersion compensation fiber has been proposed based on PCFs. As demonstrated in the previous section, the dispersion of solid-core PCFs can be easily tuned by varying the geometric parameters of the air-hole arrays found in the cladding, which includes air-hole diameters (d) and hole-to-hole spacing (Λ), thus allowing large negative dispersions [101].

Based on this principle, various solid-core PCFs covering a broad band in the infrared range and featuring specially designed air-hole arrays have been proposed for dispersion compensation [132-136]. Moreover, with these solid-core PCFs, endless single mode guidance over a broad spectral range can be easily realized by changing the ratio of air-hole diameter to hole-to-hole spacing (d/Λ). Hence, the guided modes in these PCFs are HE_{11}-like, which ease the coupling with the transmission fibers.

2.2.2.2 Bragg fibers

Similar with photonic crystal fibers, hollow core Bragg fibers leave a lot of room for the modification of dispersion as the optical characteristics of these fibers critically depends on their geometrical parameters, including their core size, their reflective index contrast and the layer thickness of the multilayer reflector. The first example of dispersion compensation using Bragg fibers was realized by Marcou *et al.* [137], who showed that one could cancel material dispersion by waveguide dispersion in a low index contrast Bragg fiber. Later, Ouyang *et al.* [138] exploited the use of the HE_{11} mode for dispersion compensation. They showed that using a hollow core Bragg fiber with high index contrast, one can easily obtain a negative dispersion of about -20,000 ps/(nm·km). However, the applications of this fiber is limited by its small core size which is required in order to achieve a large negative dispersion. Alternatively, Dasgupta *et al.* [139] offered another approach to achieve negative dispersion using the TE_{01} mode. They showed that using multiple quarter-wave stacks, a negative dispersion about -1245 ps/(nm·km) at 1550nm can also be achieved in a Bragg fiber with the core radius of 3.5μm and an effective figure of merit (FOM) of 200,000 ps/(nm·dB). For all these Bragg fibers mentioned above, smaller core radius is necessitated for large negative dispersion. In fact, the modal dispersion can be arbitrarily small as it is proportional to $1/r_{core}^2$ [140]. When decreasing the size of the air-core, large dispersion values can be easily achieved. However, the small core limits their applicability. To overcome this challenge, Engeness *et al.* [141] proposed an alternative method for achieving large negative dispersion in a hollow core Bragg fiber with a large core radius. By introducing a defect layer to the cladding, core-guided modes will anticross with defects modes, similar to what happens in the case of dual-core PCFs, and as a result, large negative dispersion can be achieved. The Bragg fiber proposed in [141] featured a large core with a radius of 14.8μm and could support a large negative dispersion of ~-55,000ps/(nm·km) at $\lambda = 1650\text{nm}$.

2.2.2.3 Fiber Bragg gratings

Fiber Bragg gratings (FBG) are one of the most widely used optical devices for dispersion compensation in the optical domain. Different long-haul optical communication systems have been developed by employing fiber Bragg gratings as dispersion compensators, and show that FBGs of only a few centimeters can completely cancel the dispersion introduced by transmission links of several-hundred-kilometers [142-144]. For these FBGs, strong dispersion can be produced in both reflection and transmission.

In reflection geometry, chirped fiber Bragg gratings are used for dispersion compensation as their resonant frequency is linear with the axial position, because of both non-uniform grating period and the reflective index modification and thus exhibit different delay at different frequencies [145-148]. Both large bandwidth and large dispersion can be provided by chirped gratings. Ouellette [145] was the first to theoretically demonstrate the potential of using a linearly chirped fiber Bragg grating for dispersion compensation. The dispersion could be high and quasi-constant over the reflectivity bandwidth and it can be modified by adjusting the chirp coefficient. Moreover, the sign of dispersion can be both positive and negative depending on the direction of light propagation.

Another way of using FBGs for dispersion compensation is through transmission–based geometry where the grating simply follows the transmission fiber [149-150]. In this design, uniform fiber Bragg gratings can exhibit high dispersion at frequencies close to the edge of the transmission band gap and, thus, can be used for dispersion compensation. Litchinister et al. [149] numerically investigated the transmission links that use uniform FBGs. By detuning the center frequency of the FBG, a pulse compression ratio of over 2.4 was obtained. Compared to the reflective dispersion compensation, this transmission based fiber imparts much lower insertion losses as the directional coupler is not needed.

2.3 Contribution and impacts of my works

In my doctoral study, I investigated three different types of waveguides in the attempt to manipulate THz beams more efficiently. In particular, I first proposed a novel hollow core photonic bandgap waveguide which is essentially a generalization of the earlier 2D waveguides featuring hyperuniform claddings into 3D waveguides and fibers. Comparing to its counterparts with

periodic reflectors, the proposed waveguide showed potential for producing bandgaps with large widths. Moreover, owing to its aperiodic reflectors, such a waveguide can produce complete bandgaps for all polarizations, and hence can be used as an optical modulator with higher efficiencies for terahertz radiation. This is the first attempt to produce a 3D hollow core waveguide featuring hyperuniform reflectors. The performance of such waveguide can be further improved via using different hyperuniform point patterns to produce the reflector geometry. Besides, advanced 3D printing technique with higher printing resolution and accuracy can also be of great benefits to improve the waveguide performance. I believe this work will open a new venue for both light guidance and beam modulation for terahertz frequencies.

Further along the text of the thesis, I will present two works on dispersion managements for THz frequencies. The first one is a porous graded index optical fiber (GI-mPOF) for dispersion reduction in the THz frequency range. The fiber is made from polyethylene plastic and features a non-uniform array of variable size subwavelength holes positioned at subwavelength separations with respect to each other, thus resulting in a graded refractive index effective medium. The proposed fiber structure has successfully reduced both the individual and intermodal dispersions, and hence retained the pulse broadening and widened the spectral transmission range. Subsequently, I will demonstrate a waveguide Bragg grating which can be used for the dispersion compensation in THz frequency range. With longitudinally positioned periodic structures, the proposed waveguide Bragg grating supports a signal mode operation range in the vicinity of 0.14GHz. The HE_{11}-like fundamental mode offers large, negative dispersion in this frequency range.

To the best of my knowledge, this is the first investigation of dispersion management based on waveguides in the THz frequency range. In the past decades, various fibers and waveguides have been proposed for low-loss guidance in the THz regime, and thus loss reduction in THz fibers can be considered as a solved problem. However, dispersion reduction and compensation in THz fibers were rarely studied. The study in this thesis offers good solutions to problems arising by the dispersion in the terahertz range.

With properly chosen lengths, the proposed GI-mPOF and waveguide Bragg grating can be used to build up a fiber-based transmission link with several-meter-length. Such a fiber-link can offer a guiding with both low-loss and low-dispersion for terahertz frequencies, which can be of

great benefits for terahertz communication in areas rapidly changing geometrical environment (busy conference center, etc.), or where a blocking object like a wall has to be penetrated.

Moreover, the proposed waveguide Bragg grating can also be used to cancel the dispersion for a wireless terahertz communication system. Although the dispersion of the dry gas is negligible, problems caused by dispersion are still pronounced after a long distance propagation, and would be further deteriorated if the humidity in the atmosphere is high, as the dispersion of moist gas is much higher than that of the dry one [29]. As a consequence, if we insert a waveguide Bragg grating with large negative dispersion at the beginning or end of the free space propagation based transmission link, the quality of received THz signal would be improved, and hence higher data rates are available.

CHAPTER 3 METHODOLOGY

3.1 Waveguide Fabrication

The dielectric waveguides mentioned in my thesis were fabricated using two different manufacturing methods, including thermal fiber drawing and 3D printing. Thermal fiber drawing has been widely used for optical fibers made mostly of thermoplastic polymers. When supplemented with the stacking method [178], the drilling method [179], and the extrusion moulding method [180] for preform fabrication, thermal fiber drawing technology is very convenient for fabricating fibers with structural features in the micro-, or even nano-scale. Using this technology, I fabricated porous optical fibers with both graded and uniform air-hole-arrays using a custom-made fiber drawing tower for polymer fibers. In particular, microstructured preforms, featuring an isotopically magnified version of the designed fiber geometry, are first prepared with commercial low density polyethylene (LDPE) rods drilled using a computer numerically controlled (CNC) machine. Then, fiber preforms are heated and melted in a furnace, and stretched into fibers with the designed size using a mechanical tractor. During the drawing process, air pressure is employed to prevent air-holes from collapsing. The fiber diameter is controlled by both the feeding speed of the preform holder (v_{feed}) and the stretching speed of the tractor ($v_{stretch}$), as $d \sim v_{feed}/v_{stretch}$. With a precise control of all parameters mentioned above, we finally obtained fibers with well-maintained structures and uniform diameters over several meters.

The main limitation of the fiber drawing process is that it only allows the fabrication of quasi-3D fibers. The term “quasi-3D fibers” refers to fibers featuring microstructures in the transverse plane and remaining invariable in the longitudinal plane. On the other hand, 3D structured waveguides, whose geometries vary in all three dimensions, cannot be fabricated by using the abovementioned thermal drawing method. The main challenge for the development of 3D structured optical waveguides is the limited availability of the 3D micro/nano fabrication techniques that could operate with dielectric/metallic materials. In the terahertz spectral range, where the wavelength of light is larger than 300μm, a recently developed technique using stereolithography, at a high resolution of < 30μm, can be used for the fabrication of 3D structured waveguides [151-154].

Stereolithograph, also known as stereolithography apparatus (SLA), is a form of 3D printing technology used for creating models, prototypes, and patterns in a layer by layer fashion using photopolymerization, a processing by curing photosensitive polymers with ultraviolet UV light [155]. With the assistance of 3D modeling software, the printed 3D objects are first preprogramed. The UV laser light is patterned by a computer controlled projector and then focused on the surface of a vat of photosensitive resin. With this technique, the exposed resin is solidified, and a single layer of the desired 3D object is fabricated. By repeating this process, the designed 3D object is fabricated layer by layer. A typical setup for stereolithgraphy is shown schematically in Figure 3.1 [156].

In this thesis, I will present two THz waveguides fabricated through the use of stereolithography. The first one is a hollow core THz waveguide featuring hyperuniform disordered reflectors. The hyperuniform reflectors in the waveguide cladding are comprised of dielectric cylinders with radiuses of 113μm connected by dielectric walls having a thickness of 35μm. Although the printer we used (*ProJet 3500HD Plus* from *3D system*®) offers a lateral resolution of ~100μm, we can only print structures with bridges thicker than 200μm due to the complexity of the printed structure and the mechanical properties of the resin we used. The other 3D waveguide shown in my thesis is a hollow core waveguide Bragg grating featuring periodically placed

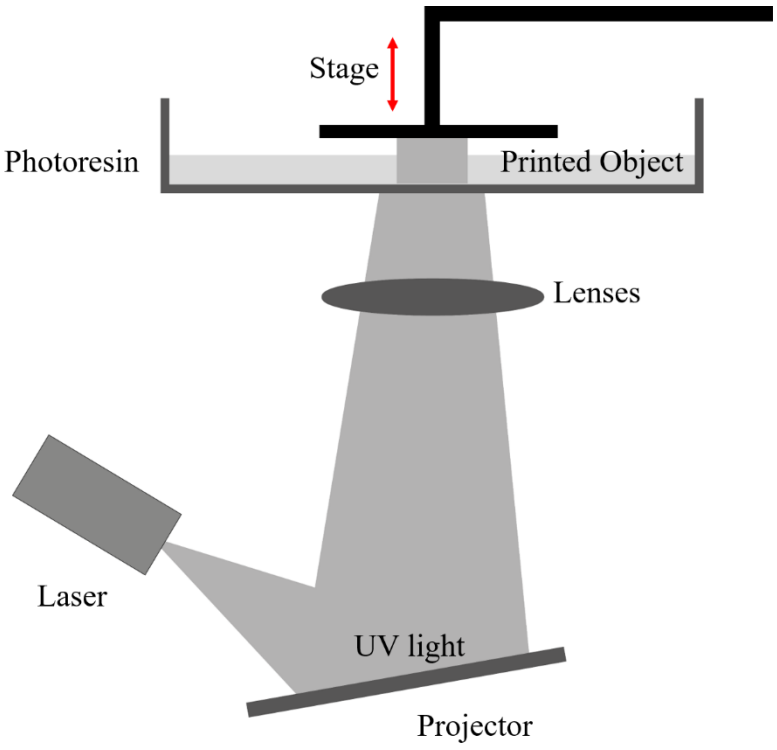

Figure 3.1 Schematic of a typical stereolithography printing system

triangular axisymmetric slopes on its inner surface. This waveguide was fabricated using another commercial stereolithography 3D printer (*Asiga® Freeform PRO2*) with a photosensitive resin(*PlasCLEAR*) offering resolutions of up to 50μm along the x- and y-axes, and up to 1μm along the z-axis. After printing, the waveguide prototype was fully metallized through coating with a silver layer using a wet chemistry coating method.

3.2 Numerical Simulation

To numerically analyze the optical characteristics of the fabricated THz waveguides, I utilized a commercial finite element (FEM) software, COMSOL Multiphysics. The fiber geometries were extracted from the high resolution photographs of their cross-section and imported into the COMSOL solver for further numerical analysis. By solving the time-independent Helmholtz equation with the complex effective refractive index as a parameter, we can adjust dispersion relations and the modal electromagnetic field distribution of guided modes to construct the complete modal structure of the fabricated waveguides.

When modes propagate through the waveguide, they gain frequency dependent phase factors and lose power due to transmission losses. I consider that all of these modes propagate individually. Hence, the distribution of the transverse electric field components at the output facet of the waveguide with a length of L_w can be constructed by coherently superposing the N guided modes as

$$\vec{E}_{out} = \sum_{m=1}^{N} C_m \cdot \vec{E}_m \cdot \exp\left(i\frac{\omega}{c} n_{eff,m} L_w\right) \cdot \exp\left(-\frac{a_m L_w}{2}\right) \tag{3.1}$$

where $\vec{E}_m$ refers to the field distribution of the m-th guided mode, while $n_{eff,m}$ and a_m are the real part of its modal effective refractive index and power loss coefficient, respectively.

The variable C_m refers to the normalized amplitude coupling coefficient, which is computed from the overlap integral of the respective flux distribution of m-th mode with that of the input Gaussian beam as a source. Specifically, the definition of C_m is based on the continuity of the transverse field components across the input interface (i.e. cross-section of the fibers) between the incident beam and the excited fiber mode [157]

$$C_m = \frac{1}{4}\int dxdy\left(\boldsymbol{E_m^*}(x,y)\times\boldsymbol{H_{input}}(x,y) + \boldsymbol{E_{input}}(x,y)\times\boldsymbol{H_m^*}(x,y)\right) \times \frac{1}{\sqrt{\frac{1}{2}\mathrm{Re}\left[\int dxdy\left(\boldsymbol{E_m^*}(x,y)\times\boldsymbol{H_m}(x,y)\right)\right]}\times\sqrt{\frac{1}{2}\mathrm{Re}\left[\int dxdy\left(\boldsymbol{E_{input}^*}(x,y)\times\boldsymbol{H_{input}}(x,y)\right)\right]}} \quad (3.2)$$

In 2D simulation, I used a Gaussian beam whose fields were normalized to carry power P [158]:

$$\boldsymbol{E_{input}}(x,y) = \vec{x}\cdot\sqrt{\frac{2P}{\pi\sigma^2}}\cdot\exp\left[-\frac{x^2+y^2}{2\sigma^2}\right]$$
$$\boldsymbol{H_{input}}(x,y) = \vec{y}\cdot\frac{1}{\sqrt{\mu_0/\varepsilon_0}}\cdot\sqrt{\frac{2P}{\pi\sigma^2}}\cdot\exp\left[-\frac{x^2+y^2}{2\sigma^2}\right] \quad (3.3)$$

where the Gaussian beam waist parameter σ is related to the full-width hall-maxima by field as $FWHM = 2\sigma\sqrt{2ln2}$, $\vec{x}$ and $\vec{y}$ are the unit vectors in x- and y-directions, $\sqrt{\mu_0/\varepsilon_0}$ is the intrinsic impedance of vacuum.

Meanwhile, I also modelled the input beam by a 3D Gaussian beam for 3D simulations, which can be given as [159],

$$\boldsymbol{E_{in}} = \overrightarrow{n_r}\frac{\omega_0}{\omega(z)}\cdot\exp[-\frac{r^2}{\omega^2(z)}]\cdot\exp[-i\frac{k\cdot(r^2)}{2R(z)}]\cdot\exp\{-i[kz-\phi(z)]\} \quad (3.4)$$

where ω_0 is the beam waist radius and assumed to be $\sim 2\lambda$, $\omega(x)$ is the spot size, $R(x)$ is the beam curvature radius, and $\phi(x)$ is the Guoy phase shift.

3.3 Optical Characterization

The optical properties of waveguides shown in this thesis were characterized by measuring their complex transmission spectra with terahertz spectroscopies, including a modified terahertz time-domain spectroscopy (THz-TDS) and continuous-wave terahertz (CW-THz) spectroscopy.

The modified THz TDS consists of a frequency doubled femtosecond fiber laser (MenloSystems C-fiber laser with the output wavelength of 780nm) used as a pump source and two identical GaAs dipole antennae used as a THz emitter and a detector. The GaAs dipole antennae we used can yield a spectrum range of 0.1 to 3.0 THz. However, because of the lower

dynamic range and increased material losses in the fiber at higher frequencies, I only considered the spectrum range of 0.2 to 1.5 THz in the following sections.

As schematically demonstrated in Figure 3.2 (a), the femtosecond laser we use produces a train of output pulses with a repetition rate of $\sim 100\mathrm{MHz}$ and pulse lengths of $120\mathrm{fs}$. For the sake of coherent detection, the output pulse train is split into two with a 50/50 beam splitter. One half of the pulse train is projected to the THz emitter and utilized for generating the THz signal, while the other half is employed for gating the THz detector. With the assistance of the optical pulse train, when the THz pulse hits the detecting antenna gap, its electric trace $E(t)$ of can be directly recorded by measuring the generated photocurrent.

In the experiment, the THz electric trace $E(t)$ in the time domain is sampled point by point, and its Fourier transform gives us a complex frequency spectrum which contains both amplitude and phase information. Subsequently, the absorption of the test sample can be retrieved from the amplitude information, while its dispersion relation, or corresponding refractive index, can be evaluated based on the phase information.

For the THz-TDS system, the point-by-point sampling is realized by utilizing a linearly mechanic delay line. In such measurements, the position of *z* of the delay line can be converted to the time-domain coordinate *t* as

$$t = \frac{2z}{c} \tag{3.1}$$

where *c* is the speed of light, and the factor of 2 refers to the fact that the optical light travels twice in the delay line. By the Fourier transform, the specifications of the complex transmission spectra, namely the maximum frequency f_{max} and the frequency resolution δf, are linked to the step size dz and total displacement Δz, respectively, which can be given as

$$\begin{aligned} f_{max} &= \frac{1}{2 \cdot \delta t} = \frac{c}{4 \cdot \delta z} \\ \delta f &= \frac{1}{\Delta t} = \frac{c}{2 \cdot \Delta z} \end{aligned} \tag{3.2}$$

Hence, the maximum achievable spectral resolution in the frequency domain is limited by the maximum displacement of the optical delay line. Specifically, for our system, the total length of

the optical delay line is about $z_{max} = 125\text{mm}$, resulting in a maximal spectral resolution of $\delta f_m = 1.2\text{GHz}$.

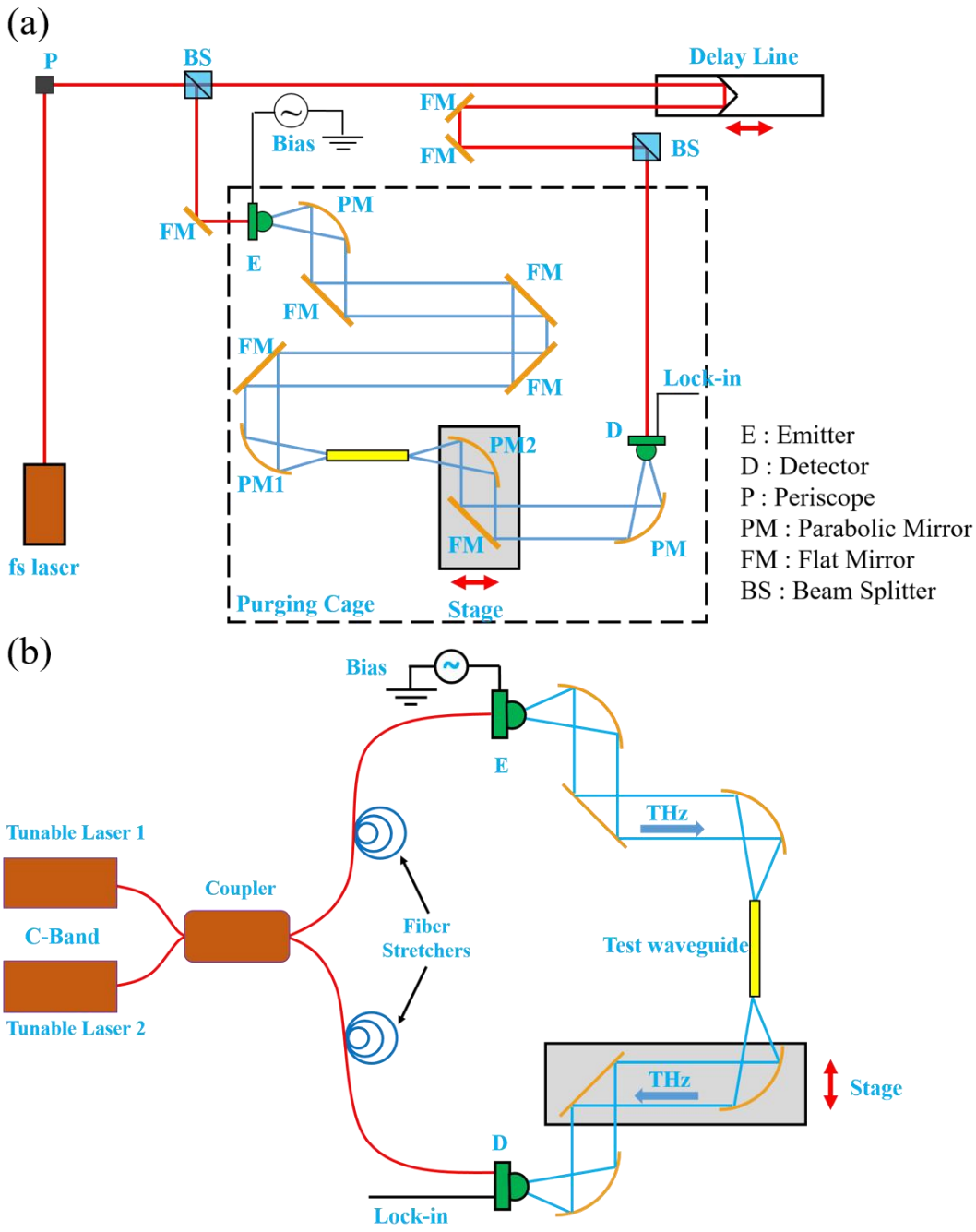

Figure 3.2 Schemas of (a) THz-TDS setup and (b) CW-THz setup for measuring the transmission of THz waveguides. For both systems, mirror assemblies, which are mounted on the movable stage, can translate the output focal plane to accommodate waveguides with different lengths. Optical beams/fibers are shown in red, while the THz beams are in blue.

To measure waveguide transmission at a higher resolution, I use a continuous wave Terahertz (CW-THz) spectroscopy system (*Toptica Photonics*®). This setup consists of two distributed feedback (DFB) lasers with slightly different center wavelengths and uniform power (~30mW for each) when operating in the telecom region. A 50:50 coupler combines and splits the two wavelengths equally into the emitter and detector arms respectively. Two single mode polarization maintaining fibers wounded around piezo actuators that stretch in opposite directions are connected to both of the arms for the phase measurement. The symmetric arrangement of the fiber stretchers provides additional path delay as well as phase noise cancelation that can be caused by the variation in the environment [160]. The path lengths between the emitter and detector arms are balanced (in the empty configuration) to have a flat phase, which is almost frequency independent. The THz waves are generated by the emitter photomixer which emits the frequency difference between the two lasers which are further modulated using bias voltage for lock-in tection. By tuning the lasing wavelengths, such a system can generate a tunable THz radiation that rests between 50 GHz-1.2 THz, with a bandwidth as narrow as 40MHz.

To analyze the optical properties of THz waveguides shown in my thesis, I employed several methods in the experiment. The first technique was to directly compare transmission spectra obtained by different measurements. Typically, one should measure two pulses. One is the sample pulse which propagates through the entire optical system including all mirrors, lenses, and the tested waveguide, while the second pulse is measured when the waveguide is removed and the rest of the optical system remains intact. The complex transmission, involving both the amplitude transmission $[t(\omega)]$ and phase $[\varphi(\omega)]$ information, can be extracted based on these two measurements by

$$T(\omega) = t(\omega) \cdot exp[i\varphi(\omega)] = \frac{E_f(\omega)}{E_r(\omega)} \tag{3.3}$$

where E_f and E_r are the measured the complex electric fields measured with and without the tested waveguide. This technique offers a general overview of the optical characteristics of the waveguide, but does not allow for in-depth analysis. For example, different sources of loss, such as coupling and absorption losses, cannot be discriminated. In my thesis, I will show the characterization of the waveguide Bragg grating using this technique, where the measured transmission of the waveguide Bragg grating is compared with that of the commercial copper tubes

and metallic hollow core waveguides. With this method, transmission with several stop bands and large negative dispersions is confirmed.

Another technique is the cut-back method. In this type of measurement, transmission of the waveguide segments with different lengths are measured. The input facet of the waveguide is fixed by custom-made holders with respect to the focal point of the fixed parabolic mirror (PM1 in Figure 3.2 (a) and (b)), which, thus, ensures that the coupling coefficient of the input beam to the fiber modes remains unchanged during the measurement. The waveguide output end is fixed to the focal point of another parabolic mirror (PM2 in Figure 3.2 (a) and (b)), which is mounted on a movable stage. During the measurement, the length of the test waveguide is altered by repeatedly cutting its output end or removing waveguide sections one by one.

The cut-back method enables us to eliminate the waveguide coupling efficiency from losses calculation and obtain the transmission losses of the test waveguide. By comparing the transmission of waveguides with different lengths, we can extract both the losses and modal dispersion by

$$T_m(\omega) = \frac{E_m(\omega)}{E_{ref}(\omega)} = C_{in} \cdot C_{out} \cdot \exp\left(-\frac{\alpha L}{2}\right) \cdot \exp\left(i\frac{\omega}{c}\left(n_{eff} - 1\right)L\right) \tag{3.4}$$

where $E_{ref}(\omega)$ and $E_m(\omega)$ are the complex electric fields at frequency ω measured without and with the tested waveguide of length L, C_{in} and C_{out} are the coupling coefficients at the input and output facets of the tested waveguide. α and n_{eff} are the absorption loss and modal effective refractive index of the guided mode in the tested waveguide.

As mentioned above, the coupling coefficients at both the input and output facets remain unchanged in the measurements. Hence, we can get rid of the coefficients of C_{in} and C_{out} by applying the transmission of waveguides with different lengths to Equation (3.4) by

$$\frac{T_2(\omega)}{T_1(\omega)} = \exp(-\alpha \cdot (L_2 - L_1)/2) \cdot \exp\left(i\beta \cdot (L_2 - L_1)\right) \tag{3.4}$$

where $\beta = \frac{\omega}{c} n_{eff}$ is the propagation constant. Finally, we can get the transmission loss α and modal effective refractive index n_{eff} by using Equation (3.4) for multiple measurements.

CHAPTER 4 ARTICLE 1 : 3D PRINTED HOLLOW-CORE TERAHERTZ OPTICAL WAVEGUIDES WITH HYPERUNIFORM DISORDERED DIELECTRIC REFLECTORS

This chapter is based on the paper "3D Printed Hollow-Core Terahertz Optical Waveguides with Hyperuniform Disordered Dielectric Reflectors," published in *Advanced Optical Material* in 2016 [161]. I am the primary author of this paper, while this paper is co-written by Hichem Guerboukha and Maksim Skorobogatiy from Ecole Polytechnique de Montreal, Martin Girard from Northwest University, and Andrew D. Squires and Roger A. Lewis from University of Wollongong. My role in this paper includes the numerical modeling and experimental characterization. I am responsible for the theoretical analysis and experimental characterizations of the proposed waveguide.

In this chapter, we proposed a hollow core THz waveguide featuring hyperuniform disordered reflectors. Comparing with the photonic bandgap reflectors with periodic structures, hyperuniform disordered reflectors have shown potentials for low-losses guidance with enlarged photonic bandgaps for 2D planar waveguides. In this chapter, for the first time, we successfully utilized the concept of hyperuniform disordered reflector to the development of 3D waveguides and fibers, and confirmed both numerically and experimentally that such waveguides feature spectrally broad bandgaps that are potentially superior to those attainable with purely periodic structures.

4.1 Introduction

Photonics crystal (PC) materials have drawn great interest over the years because of their unique properties that allow advanced light management [162]. In particular, dielectric reflectors based on PCs can be employed to create hollow-core fibers by arranging such reflectors around a gas filled cavity. In such fibers, the light is confined in the hollow-core for frequencies within the reflector photonic bandgaps (PBGs). Based on this principle, various hollow-core PBG fibers have been proposed for simultaneously low-loss and low-dispersion guidance over sizable spectral ranges [163]. These fibers can be divided into two categories, Bragg fibers and holey fibers, according to their reflector structure.

Generally, hollow core Bragg fibers consist of a circularly symmetric Bragg reflector which is formed by alternate high and low refractive index layers. The Bragg reflector can be all-solid or porous. The all-solid Bragg reflector is formed by repeating alternate concentric layers of two different polymers [54] or the same polymer with different dopants [57-58]. The bandgap position and its spectral width are determined by the thickness and the refractive indices of the alternate layers. The periodic refractive index variation in Bragg reflectors can also be realised by introducing rings of porous material. Using this approach, hollow core Bragg fibers with solid/randomly porous multilayers [60], air-hole rings [59] and cob-web structures [41,62] were investigated in the terahertz range. Another type of hollow core PBG fiber is the holey fiber. Such fiber features reflectors formed by various types of periodic lattices, such as, rectangular [50], triangular [50], honeycomb [51], etc. The holey PBG fibers are typically designed to have high air-filling fractions in order to achieve bandgap.

Recently, both numerical [164-166] and experimental [167-170] studies in 2D have shown that hyperuniform disordered structures present a new class of disordered photonics materials that can possess large complete photonic bandgaps for all polarizations. In these studies, the key parameter that characterizes hyperuniform structures is the hyperuniformity χ, which was first introduced as an order metric of a point pattern based on its local density fluctuations [169]. The hyperuniformity is zero for a random pattern taken from a Poisson distribution, becomes disordered when $\chi > 0$ and eventually settles in a crystal pattern around $\chi \sim 0.8$. A particular type of hyperuniform disordered structure that was considered in [169] comprises dielectric cylinders connected by thin dielectric bridges. Based on this structure, various planar hyperuniform waveguides have been developed with both high [166] and low refractive index contrasts [167] that exhibited spectrally broad bandgaps, as well as photonic bandgap guidance for all polarizations. Moreover, it was demonstrated in [168] that for the same refractive index contrast, hyperuniform reflectors can have larger bandgaps than their counterparts featuring periodic PCs. Thus, it could be expected that hollow core PBG fibers featuring hyperuniform reflectors could have spectrally broader bandgap than hollow core PBG fibers that use strictly periodic reflectors.

In this paper, we propose a novel hollow core terahertz PBG waveguide that uses hyperuniform disordered reflectors. This is essentially a generalization of the earlier 2D waveguides featuring hyperuniform claddings [164-170] into 3D waveguides and fibers. Our main motivation is to explore the possibility of designing hollow core waveguides that feature spectrally

broad bandgaps that are potentially superior to those attainable with purely periodic structures. Particularly, we demonstrate theoretically that using resin/air material combination that offers relatively low refractive index contrast of 1.67/1, one can design a hollow core waveguide featuring an 90GHz (~21%) bandgap centered in the vicinity of 0.41THz. In such waveguide, highly porous PBG reflector is comprised of ~113μm radius cylinders connected with ~35μm thick bridges. We then fabricate such waveguides using 3D stereolithography. The diameter of the resultant waveguides (reflector size) is ~20mm, while the diameter of the hollow core is ~5mm. Due to limitations in the 3D printer that we have used, the resolution was limited to 100μm which allowed us to print structures with bridges thicker than 200μm. As we demonstrate, both theoretically and experimentally, thicker bridges lead to an overall reduction of the bandgap spectral size. Nevertheless, the fabricated waveguides featured relative wide bandgaps (up to ~15%), and low transmission losses (<0.10cm^{-1}) within their PBGs.

4.2 Fiber Design

In order to generate a disordered reflector structure, we use a set of dielectric cylinders connected with thin dielectric bridges. The cylinder centers follow a distribution of 2D hyperuniform point pattern. For any point pattern, its point distribution can be characterized by its number variance, which is given by the standard deviation of the number of points (N_R) in a sampling window Ω of radius R in d dimension, $\sigma^2(R) = \langle N_R^2 \rangle - \langle N_R \rangle^2$ [171]. A point pattern is called "hyperuniform" if the corresponding number variance within Ω grows slower than the volume of Ω namely R^d. In reciprocal space, the point distribution can be characterized by its structure factor $S(k)$. In [164], it has been shown that if a hyperuniform point pattern is tailored such that its structure factor $S(k)$ is zero for all $|k| < k_c$, such a point pattern is called "stealthy" and can produce photonic bandgaps. Moreover, the critical value k_c can be related to the hyperuniformity χ, which is defined as [170]:

$$\chi = \frac{M(k_c)}{d \cdot N} \tag{4.1}$$

where $M(k_c)$ is the number of constrained degree of freedom and $d \cdot N$ is the total number of degrees of freedom with d is the number of dimensions and N is the total number of points.

In our design, we used a value of $\chi = 0.5$ since it has been shown in [164] that it generates a hyperuniform point pattern that can be optimized to produce a complete PBG for both TE and TM polarizations in a 2D photonic crystal waveguide. To drive the structure factor $S(k)$ to zero

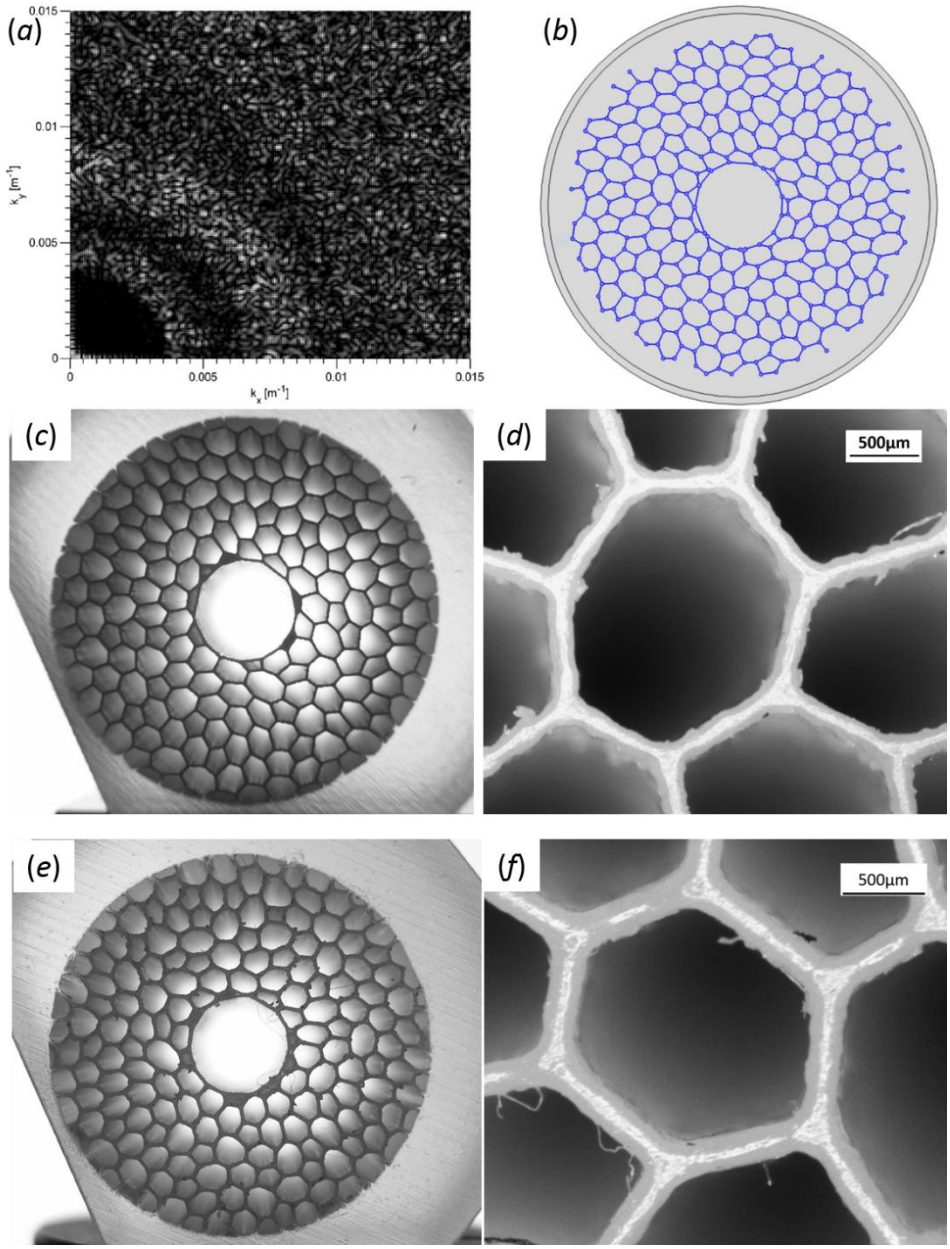

Figure 4.1 (a) Hyperuniform point pattern in k-space. This point pattern is used to define center positions of the dielectric cylinders in the hyperuniform PBG reflector. (b) Waveguide and a computational cell used in our numerical simulations. The reflector material is shown in blue, while the air is gray; the computational domain is terminated by a circular perfect electric conductor (PEC). The cylinder radii are 113µm and the bridge thickness is 35µm. (c) The fabricated

waveguide with a bridge thickness of 200μm in the reflector. (d) Zoom of the reflector region shown in (c). (e) The fabricated waveguide with a bridge thickness of 250μm. (f) Zoom of the reflector region shown in (e).

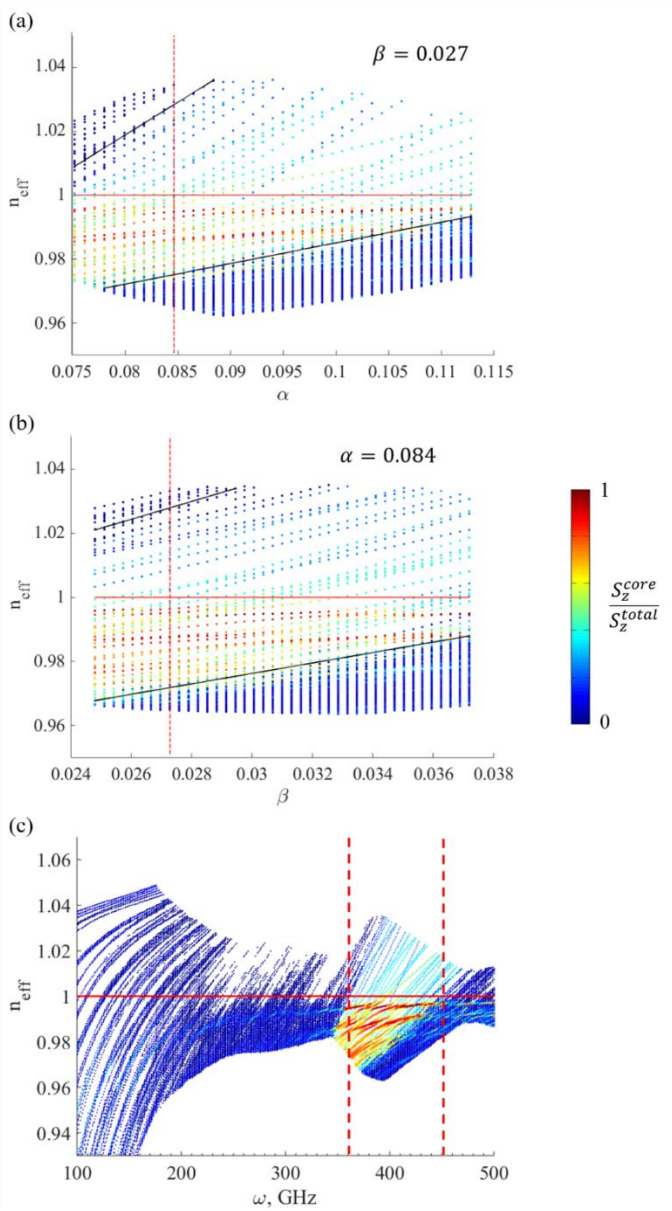

Figure 4.2 Optimazition of the waveguide structure. (a) Sweeping α with fixed $\beta = 0.027$ results in an optimal value of $\alpha = 0.084$, while (b) sweeping β with fixed $\alpha = 0.084$ results in an optimal value of $\beta = 0.027$. The two black solid lines define the boundaries of the continuum of the cladding-bound states. The red line refers to the air light line with $n = 1$. The red dashed line shows the optimal parameter value for which the air light line is positioned strictly in the middle between

the two boundaries with the continuum of cladding states. (c) The band diagram of the numerically optimized waveguide structure. The red dashed lines refer to the boundaries of the bandgap centered at 0.41THz, having the width of ~90GHz. The red solid line shows the air light line.

for all $|k| < k_c$, we changed the particle coordinates using the TOMLAB's MINOP algorithm, which is a Fortran-based reduced gradient nonlinear optimization solver. In Figure. 4.1(a), we illustrate the Fourier transform in the k-space of the generated hyperuniform point pattern. The brightness of each point is proportional to the absolute value of its structure factor $S(k)$.

Then, following the method described in [164], we developed the cross section of the proposed waveguide based on the generated hyperuniform point pattern. A triangular mesh is defined with the hyperuniform point pattern as its vertices using the Delaunay triangulation method. Then, cylinders with radii of r_c are placed at the centroid of each triangular cell. Finally, cylinders in neighboring triangular cells are connected using dielectric bridges of thickness t_b. The central part of thus generated structure was replaced with a hollow core of 5mm diameter. The final step in our design was to maximize the full PBG width of the proposed waveguide by optimizing its structural parameters, namely the cylinder radius r_c and the bridge thickness t_b. Similar optimization has been done in [164], where these structural parameters were optimized for a planar hyperuniform waveguide with the optimized parameters expressed as

$$\begin{aligned} r_c &= \alpha \frac{L}{\sqrt{N}} \\ t_b &= \beta \frac{L}{\sqrt{N}} \end{aligned} \tag{4.2}$$

where L is the size length of the supercell and N is the number of points in this supercell. For our waveguide, $L = 21\text{mm}$ and $N = 256$. In our simulation, we set the central frequency of the PBG at 0.4THz and the cladding material refractive index at 1.67. Then, by performing consecutive sweeps of both α and β parameters, we can iteratively optimize the waveguide structure and maximize the resultant PBG at a fixed frequency. Particularly, at each optimization step, we fix one of the parameters (say α) at the optimal value found in the previous step. Then, we perform a one dimensional sweep of the other parameter (β) and find its new optimal value. We then repeat the procedure by switching the parameters (fix β, sweep α). Optimal value of a parameter is defined as one that results in an equidistant separation of the air light line from both the lower and the upper edges of the continuum of cladding states. This optimization condition is meant to

minimize scattering of the core guided modes (with effective refractive indices close to that of air) into the continuum of cladding modes. After several such iterations the values of the two parameters converge to their optimal values of $\alpha = 0.084$ and $\beta = 0.027$ with the corresponding optimal cylinder radius and bridge thickness being 113μm and 35μm, respectively. In Figure. 2(a) and (b), we demonstrate two consecutive sweeps of α and β after convergence is achieved. The proposed waveguide with optimized parameters is shown in Figure. 4.1(b), and the corresponding band diagram is demonstrated in Figure. 2(c). The resultant bandgap width is ~90GHz.

4.3 Optical Characterization

4.3.1 Band diagram of the proposed waveguides

Light guidance in the proposed waveguides was analyzed using commercial finite element software COMSOL. For the experimentally fabricated waveguides, the reflector geometries were extracted from the high resolution photographs of the waveguides cross-sections [see Figure. 4.1 (c) and (e)]. For the frequency dependent refractive index and absorption loss of the reflector material, we used polynomial fits (Eq. [4.S2] and [4.S3]) on experimental data presented in Section S1 of the Supporting information. Computational cell was terminated by a circular perfect electric conducting boundary. Modal dispersion relations of all guided modes for the two fabricated waveguides with different bridge thicknesses are presented in Figure 4.4 (c) and (d). In these band diagrams, we present the modal effective refractive indices (n_{eff}) of the guided modes as a function of frequency in the range of 0.1THz-0.5THz. Due to large system size and small features, modal simulation above 0.5THz is problematic due to time and memory limitations. The color code for the band diagrams [Figure. 4.3(b) and Figure. 4.4] indicates the fraction of the power guided by the individual mode within the hollow core. Thus, the blue color refers to modes with power localized mostly outside the waveguide core, while the red color refers to strong presence of the modal fields in the hollow core. In order to show core guided modes clearly, we use bigger dots to represent the modes with more than 60% of the total power in the core. The red solid line in these diagrams is the light line of air with $n = 1$, while the red dashed lines define the edges of the photonic bandgaps.

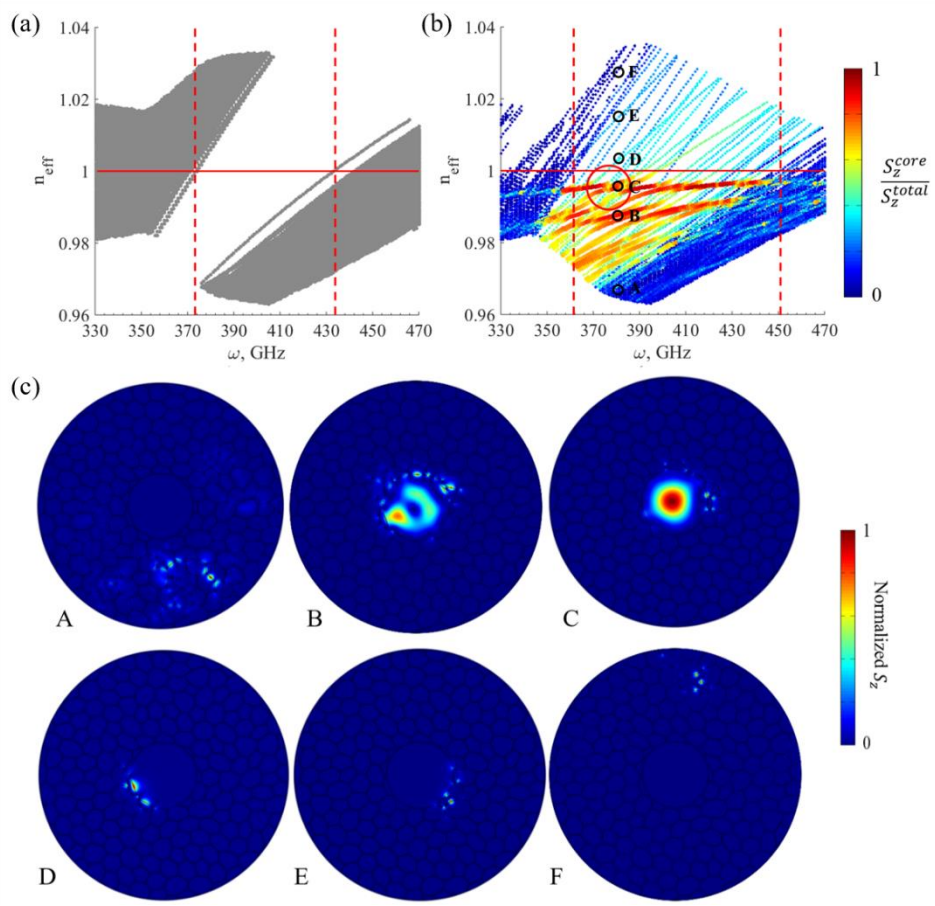

Figure 4.3 (a) Band diagram of the numerically optimized reflector structure (a) without and (b) with the hollow core. Color of each dot indicates the fraction of power guided in the hollow core. The red circle highlights an example of the modal anti-crossing between the fundamental core guided mode and one of the surface modes. The black circles refer to different types of modes guided by the waveguide at 0.38THz. (c) Normalized longitudinal flux of different modes labelled by black circles in (b). A and F: states of the reflector continuum located outside of the bandgap. B and C: second order core guided mode and fundamental core guided more located inside the bandgap. D and E: surface modes guided in the bandgap and localised in the immediate vicinity of the waveguide core/reflector interface.

As discussed in Section 4.2, the numerically optimized reflector structure ($r_c = 113\mu m$, $t_b = 35\mu m$) presents a relatively wide photonic bandgap in the vicinity of 0.4THz. Here, we investigate in greater detail the band diagram of the numerically optimized structure with and without the hollow core [Figure 4.3(a) and (b) respectively]. In the case of the coreless waveguide, COMSOL mode solver finds artificial modes propagating inside the bulk of the reflector structure, as well as

spurious modes confined in the vicinity of the boundary. To exclude these spurious modes due to numeric boundary, in Figure 4.3(a) we only present the modes that propagate in the bulk of the reflector and that have more than 30% of the total power guided in an area delimited by a radius equal to 2/3 of the waveguide outer boundary. As shown in Figure 4.3(a), the resultant bandgap is centered at 0.41THz and its width is about ~75GHz (see the definition of the bandgap in Section 4.4). When introducing a hollow core of 5mm diameter, the bandgap features a plethora of modes that can be further identified as core guided modes and surface states. Thus, the guided modes are presented in Figure 4.3(b) with dispersion relations that have red-orange color. Such modes feature fields that are strongly confined (more than 80% by power) in the waveguide hollow core. Even for frequencies outside the bandgap, dispersion relations of the guided modes (or rather resonant modes in this case) can still be clearly identified due to the light blue color of their dispersion relations (20% - 40% modal power still remaining in the fiber core) that stand out on the background of the dark blue dispersion relations corresponding to the modes of a reflector. Another type of modes present in the bandgap are the surface states that are confined in the direct vicinity of the fiber core/reflector interface. Dispersion relations of such modes have light blue colors (20%-50% of modal power in the core), and such modes have significant presence both in the fiber core and in the reflector. Spectrum of the surface states is highly sensitive to the structure of the core boundary. Surface states can, in principle, be largely suppressed via a careful design of the fiber core/reflector interface, which is, however, not a focus of this paper. In Figure 4.3(c), we present longitudinal flux (S_z) distributions of several typical modes positioned inside and outside of the PBG at 0.38THz. Particularly, the core guided modes inside the reflector bandgap, namely the first higher order mode B and the fundamental mode C, are strongly confined in the core region. The modes of the reflector found outside the reflector bandgap (modes A and F in Figure 4.3(b)) have strong presence in the cladding region. Finally, surface states within the reflector bandgap (modes D and E) are localized in the vicinity of the hollow core/reflector interface. Additionally, dispersion relations of the surface states can show avoided crossing phenomenon with the dispersion relations of the core guided modes. In the vicinity of the avoided crossing frequency (see red circle in Figure 4.3(b), for example), surface states can be strongly coupled (hybridized) with the core guided modes, thus affecting guided mode dispersion relations and losses. This phenomenon is further detailed in Section 4.4.

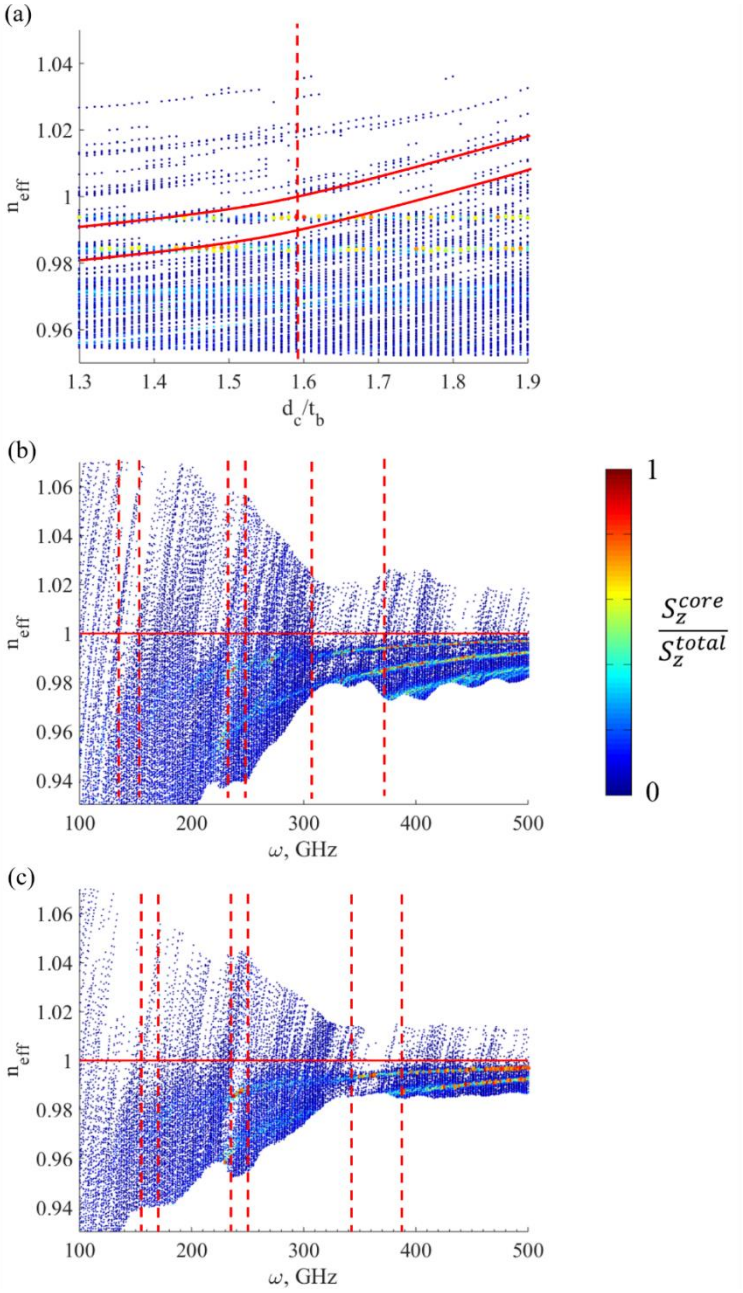

Figure 4.4 (a) Partial optimization of the waveguide structure with a bridge thickness of 200μm. Red solid lines refer to the boundaries of the reflector states, while the red dashed line indicates the optimal value of the cylinder diameter which maximizes the bandgap width. (b) The band diagram of the partially optimized waveguide structure with a bridge thickness of 200μm and cylinder diameter of 318μm. (c) The band diagram of the fabricated waveguide with bridge thicknesses of 200μm.

We also note that upon closer inspection, most dispersion relations corresponding to the core guided modes are made, in fact, of two nearly degenerate dispersion relations. This near degeneracy comes from the fact that the hollow core boundary is circular, while the core diameter (5mm) is much larger than the operation wavelength (~0.75mm at 0.4THz). Here, we would like to remind the reader that in the circularly symmetric hollow-core fibers [140], most of the guided modes are doubly degenerated. In the case of the hyperuniform reflector, the modal degeneracy is lifted due to non-circularly symmetric structure of the reflector. Intermodal birefringence, however, remains very small due to low presence of the core guided modes in the reflector region. For example, in the vicinity of the core-guided mode C in Figure 4.2(c) ($n_{eff} = 0.9948$), we found a similar mode with orthogonal polarization with $n_{eff} = 0.9930$. Similarly, in the vicinity of the core guided mode B ($n_{eff} = 0.9861$), there is another mode with $n_{eff} = 0.9855$. By comparing the modal effective refractive indices, we estimate the birefringence of the core guided modes in our waveguide to be on the order of $\Delta n_{eff} \sim 1 - 2\times10^{-3}$.

Finally, for the sake of comparison, we now discuss modal structures for the two fabricated waveguides with bridge thicknesses of 200 and 250μm. The corresponding band diagrams were calculated using the reflector geometries extracted from the high resolution photographs of the waveguides cross-sections [see Figure. 4.1 (c) and (e)], as well as using complex values of the reflector material refractive index [see Supporting Information Section 1]. As those waveguides feature suboptimal bridge and cylinder sizes, resultant bandgaps are smaller and positioned at lower frequencies [Figure 4.4(c)] than those of a fully optimized structure (see Figure 4.3(b)). For completeness, we also perform partial numerical optimization of the fabricated waveguides [Figure 4.4(a)] and compare their modal properties with those of the unoptimized fabricated waveguides. For example, during the partial optimization, the bridge thickness of a waveguide is fixed to 200μm, which corresponds to the case of a fabricated waveguide presented in Figure 4.1(c), while the cylinder diameter is changed until the optimal value is found. The optimal value is defined as one that results in the equidistant separation of the effective refractive index of the fundamental mode from both the lower and upper edges of the continuum of cladding states. Figure 4.4(a) depicts the partial optimization of the fabricated waveguide with the bridge thickness of 200μm, where the cylinder diameter is optimized to maximize the width of the bandgap centered at 365GHz. The results show that when the cylinder diameter is 318μm ($d_c/t_b = 1.59$), the dispersion relation of the fundamental guided mode is optimized according to the abovementioned

criteria see [Figure 4.4(b)]. In Figure 4.4(b) and (c), we present the band diagrams of the partially optimized and experimental structures with 200μm bridge thickness. The figures show strong similarity between the two band diagrams, as the relevant bandgaps feature similar central frequencies and bandgap widths. Thus, we conclude that the experimental structure of the fabricated waveguide is close to the partially optimized one.

4.3.2 Waveguide Transmission Measurements

Next, we characterize THz transmission of the fabricated waveguides using a cut-back measurement, which is detailed in the Supporting information [Section S2]. Transmission spectra of the fabricated waveguides with lengths of 2.5cm, 5.0cm, 7.5cm and 10.0cm are shown in Figure 4.5(c) and (d). In order to calculate the bandgap width $\Delta\omega$, we applied the second moment method detailed in [173] with the full bandgap width defined as

$$\Delta\omega^2 = 4\frac{\int(\omega-\omega_c)^2T(\omega)^2d\omega}{\int T(\omega)^2d\omega}$$

where ω_c is the bandgap central frequency and $T(\omega)$ is the field transmission. For the waveguide with a bridge thickness of 200μm, there are four PBGs centered at frequencies of 0.17THz, 0.22THz and 0.29THz and 0.38THz characterized by enhanced transmission. The spectral width of these PBGs are 18GHz, 22GHz, 44GHz and 49GHz. Meanwhile, in the case of the waveguide with a bridge thickness of ~250μm, four bandgaps are centered at 0.14THz, 0.17THz, 0.23THz and 0.29THz, respectively. The estimated spectral widths of these bandgaps are 7GHz, 25GHz, 15GHz, and 45GHz. For comparison, in Figure 4.5(a) and (b), we show the computed band diagrams for the fabricated waveguides with 200μm and 250μm bridge thicknesses. For the fabricated waveguide with a bridge thickness of 200μm [see Figure 4.5(a)], three main bandgaps are centered at 0.14THz, 0.24THz, and 0.37THz, with bandwidths of 13GHz, 12GHz, and 40GHz, respectively, while for a waveguide with 250μm bridge thicknesses, PBGs are discernable at 0.13THz, 0.24THz, and 0.33THz with corresponding band widths of 20GHz, 14GHz, and 25GHz. Overall, a relatively good agreement between the measured and theoretically predicted bandgap positions and sizes are achieved. Inconsistencies in the bandgap locations and sizes can be attributed to the conceptual differences between various approaches that are used to characterize the photonic bandgaps. Thus, when using band diagrams (Figures 4.5(a) and (b)), bandgap positions can, in principle, be inferred from the position of the “finger-like” spectral regions (see Discussion section) that do not support

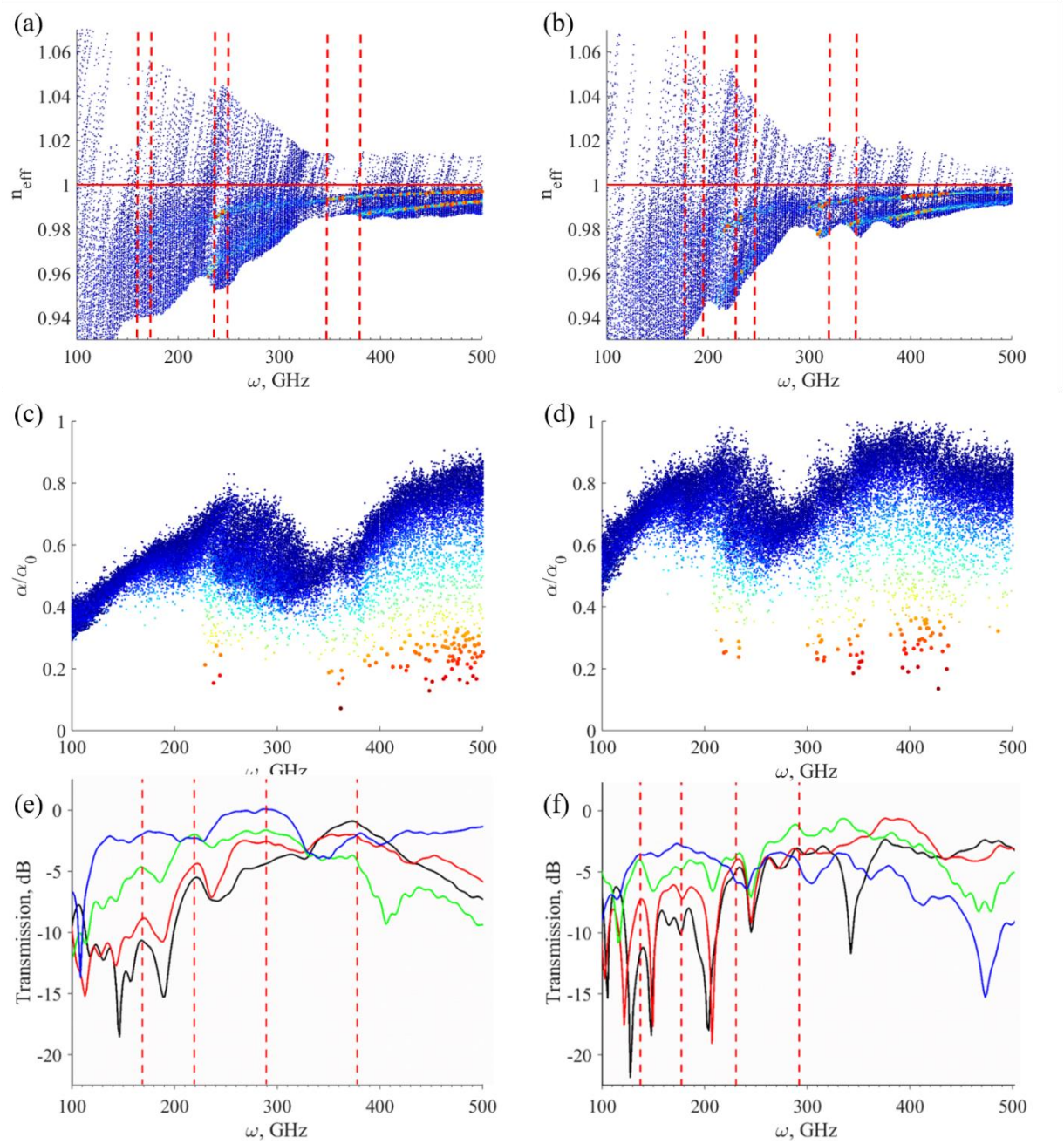

Figure 4.5 The simulated band diagrams of the fabricated waveguides with bridge thickness of (a) 200μm and (b) 250μm. (c) and (d) are the corresponding relative losses of all the modes of the two fabricated waveguides. The color code of the dots in (a) - (d) is the same as in Fig. 4.4. Experimentally measured transmission spectra of the waveguide with (e) 200μm and (f) 250μm.

any reflector states, which is a classical definition of the bandgap in the case of waveguides. In practice, especially in the case of the multimode waveguides that support multiple core guided modes and surface states, unambiguous identification of such "finger-like" regions are problematic as clearly seen in Figures 4.5(a) and (b). Moreover, from the same figures it is clear that dispersion relations of the core guided modes persist even outside of the bandgaps, thus resulting in relatively efficient transmission (albeit with higher losses) even outside of the bandgap regions. Therefore, one would expect some differences between classical definition of a bandgap from the structure of the modal band diagram as compared to the region of high transmission in the waveguide transmission spectrum. We note that there exists yet another approach to defining positions of the photonic bandgaps from the structure of the modal band diagram. In particular, one can plot the relative losses $\alpha(\omega)/\alpha_0(\omega)$ of all the modes (see Figures 4.5(c) and (d)) and define bandgaps as spectral regions where modal losses of the core-guided modes are suppressed. Here, $\alpha_0(\omega)$ is the bulk material loss of the reflector material (see [S2] in the Supporting Information section). When compared to the actual transmission spectra shown in Figures 4.5(e) and (f) we note that a modal loss-based method offers a better match between the experimental transmission data and predictions based on numerical simulations.

Finally, we note that, as the light is guided in the hollow core, transmission losses of the fabricated waveguides can be expected to be significantly lower than those of the reflector material. From Figures 4.5(e) and (f), we can deduce the waveguide transmission loss in various bandgap regions by comparing transmission through waveguides of different lengths. In what follows, we use waveguides of 10cm and 7.5cm in our estimations. For instance, at 0.23THz, the absorption loss of the first waveguide ($t_b = 200\mu m$) is estimated to be $\sim 0.1\text{cm}^{-1}$, while that of the second waveguide ($t_b = 250\mu m$) is $\sim 0.06\text{cm}^{-1}$. As expected, the propagation losses of the two fabricated waveguides are much smaller than the corresponding bulk absorption losses of the reflector material at the corresponding frequency, which is $\sim 0.55\text{cm}^{-1}$, at 0.23THz according to Eq. [S2].

4.4 Discussion

First, we would like to clarify the definition of a bandgap in the context of our hyperuniform waveguides. We note that the definitions of a bandgap related to the quasi-3D photonic crystal fibers differ from that of 2D photonic crystal waveguides. In particular, for a 2D photonic crystal waveguide, one usually projects the full 3D band diagram along one direction (such as k_x in Fig.

4.6(a)). Then, the region of frequencies that features no modes in the projected band diagram is defined as the complete bandgap of a 2D photonic crystal waveguide [157]. Such a bandgap is shown as an empty gray region in Fig. 4.6(a). However, in the case of the quasi-3D hollow-core photonic crystal fibers, complete bandgaps are rare, and one typically uses another definition of the bandgap, which is rather related to the position of the empty pockets of the modal phase space also known as "finger-like" regions (see Figure 4.6(b)). In this case, the edges of the bandgap are defined by the points of intersection of the air light line ($n_a = 1$) with the boundaries of the empty "finger-like" pockets in the band diagram as shown in Fig. 4.6(b), where the red dashed lines delimit the edges of the bandgap [162]. Within such defined bandgaps, the core guided modes are well separated from the continuum of the cladding modes, and they propagate without scattering in the perfectly uniform waveguides. Generally, bandgap definition in the case of quasi-3D fibers results in much wider bandgaps compared to the size of complete bandgaps used in the case of 2D photonic crystal waveguides.

Next, we would like to compare transmission properties of our hollow-core waveguides that feature a hyperuniform cladding with other types of the hollow-core THz waveguides. In the Table 3, we present bandgap widths and transmission losses of several all-dielectric hollow-core photonic bandgap and antiresonant waveguides. The bandgap width is defined as the ratio of the full bandgap width to the bandgap central frequency (ω/ω_0). Our theoretically optimized

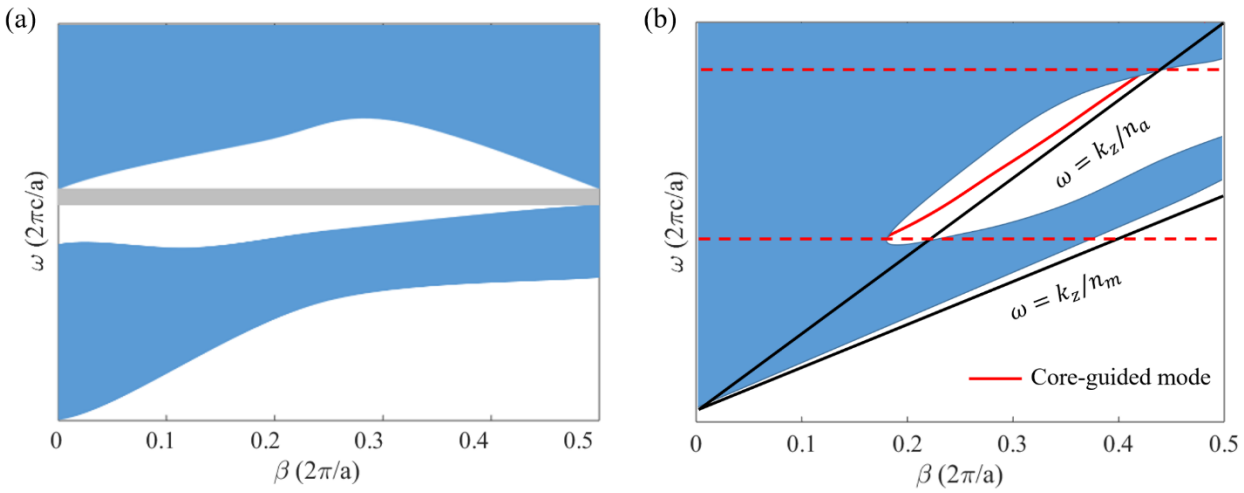

Figure 4.6 Schematic of the band diagram for (a) 2D planar photonic crystal waveguides and (b) quasi-3D photonic crystal fibers.

waveguides feature a bandgap width of 21% at 0.41THz, while the experimentally measured suboptimal waveguides feature a bandgap of 15.3% at 0.29THz, which are comparable to the largest bandgaps reported for the photonic bandgap holey or Bragg fibers. At the same time, it is not as wide as the spectral width of regions of high transmission featured by the antiresonant waveguides. This is to be expected as in the case of antiresonant waveguides the concept of "bandgap" is not strictly defined, and their transmission spectra do not manifest an abrupt transition from guided to non-guided regimes when crossing the bandgap boundaries. We also believe that hyperuniform fibers can be further optimized to result in larger bandgaps via exploration of other point patterns. Thus, further work is still necessary to find out the maximal bandgap size possible with hyperuniform disordered reflectors.

As it can be seen in Table 3, the measured losses of our hyperuniform fiber are higher than those of other types of photonic bandgap fibers. This phenomenon has multiple causes. Firstly, due to requirements of the fabrication process, we use a highly absorbent polymer (VisyJet® Crystal) as the reflector material that features material absorption that is much higher than that of other commercial polymers normally used for THz fibers, such as polytetrafluoroethylene, polypropylene, polyethylene, polycarbonate, etc. High absorption of the reflector material results in high losses of both the core-guided and the cladding modes. Secondly, our fiber features many surface states that are bound to the core/reflector interface and, thus, exhibit significant presence in the lossy cladding material [see modes D and E in Figure. 4.3(c)]. Over a certain frequency range, these surface modes hybridize with the core-guided modes and eventually "transform" into the core-guided modes, and vice versa [174]. This phenomenon is known as anti-crossing (or avoided crossing) and is presented schematically in Figure. 4.7(a). Owing to the anti-crossing phenomenon, both the dispersion relations and the losses of the core-guided modes can be significantly altered in this frequency range. In Figure. 4.7(b) and (c), we present modal properties in the spectral region of anti-crossing between the core guided mode and one of the surface states. Near 375GHz, the fundamental mode (black circles) shows strong hybridisation with a surface state (blue circles), thus leading to a significant increase in the losses of a core guided mode. As seen in Figure. 4.3(b), due to a large number of the surface states, one, therefore, expects the overall loss increase in the propagation losses of the core guided modes due to their interaction with surface states.

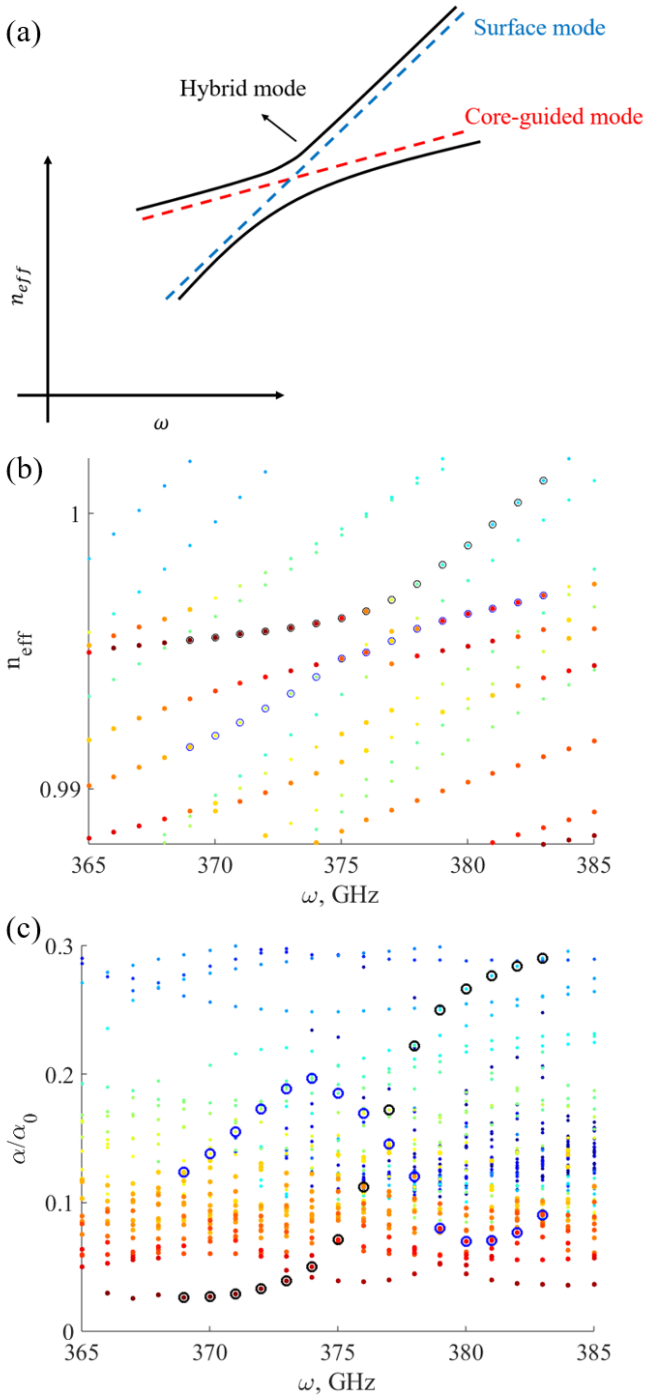

Figure 4.7 (a) Schematic of the modal anti-crossing of the core-guided mode (red dashed line) and the surface mode (blue dashed line). The black solid lines refer to the dispersion relations of the hybridized modes. (b) Dispersion relations and (c) losses of the modes in the area highlighted by the red circle in Figure. 4.3(b). Two hybridized modes are labelled by black circles and blue circles, respectively. The color code of (b) and (c) are the same as that shown in Figure. 4.3.

Table 3 Comparison of the bandgap widths and losses of the hollow core fibers featuring different reflector types.

Fiber type	Reflector structure	Reflector material	Core diameter	Bandgap	Loss (cm^{-1})	Ref
Hyperuniform fiber	Numerical optimized	Resin/air	~5mm	21% at 0.43THz	-	-
	Fabricated	Resin/air	~5mm	15.3% at 0.29THz	~0.1 at 0.23THz	-
Bragg fiber	All solid	PVDF/PC	~1mm	-	<0.02 at (1-3)THz	[163]
	Doped polymer	PE/PE with 80% wt. TiO_2	6.63mm	~13% at 0.68THz	<0.042 at 0.69THz	[54]
	Randomly porous layer	PE/air	6.73mm	~12% at 0.82THz	<0.028 @ 0.82THz	[60]
	Porous rings	PMMA/air	2mm	-	<1.1 (1.0-1.6THz)	[59]
	Cob-web structure	HDPE/air	16mm	-	5.84×10^{-8} at 0.55THz	[62]
Holey fiber	Rectangular Lattice	PTFE/air	1.12×1.87mm	~20% at 1.66THz for $d/\Lambda=0.96$	-	[50]
	Hexagonal Lattice with regular holes	HDPE/air	292μm	~7.5% at 1.47THz for $d/\Lambda = 0.93$; ~14% at 1.66THz for $d/\Lambda = 0.93$	~0.022 at 1.53THz for $d/\Lambda = 0.93$; ~0.014 at 1.75THz for $d/\Lambda = 0.96$;	[47]
	Hexagonal Lattice with inflated holes	Teflon/air	840μm	~17% at 1.80THz	<0.04cm^{-1} at (1.65-1.95)THz	[50]

	Honeycomb	Topas/air	~1mm	~4% at 0.98THz	~0.058 at 0.98THz	[51]
ARROW fiber	Hollow core tube	PTFE	~8.24mm	~41% at 1.25 THz for 0.3mm thin tube	-	[173]
	Kagome	PMMA/air	1.6mm 2.2mm	~28% at 0.87THz ~45% at 0.77THz	<0.1 at (0.75-1)THz <0.06 at (0.65-1THz)	[69]
	Tube (Single ring)	PMMA/are	1.62mm	~23% at 0.85THz	~0.04 at 0.83THz	[70]
	Tube (Several rings)	PE/air	5.5mm	~8% at 0.49THz	-	[72]

Finally, we would like to comment on the 3D stereolithography technique that has been used in this paper. Overall, this is a mature technology that has been widely used in the fabrication of microelectronic and optical devices [175-177]. Currently, ~200μm lateral resolution is standard, while some commercial system also offers sub-50μm lateral resolution. The biggest limitations of this technology are a limited material choice (photosensitive resins used in fabrication), as well as a limited build volume (~10-20cm linear dimension). Compared with the traditional fiber drawing fabrication method even when supplemented with stacking method [178], drilling method [179], and extrusion moulding method [180] for preform fabrication, the 3D stereolithography technology still enables fabrication of waveguides with significantly more complex transverse profile. At the same time, fiber drawing does not suffer from “resolution” issues that are present in 3D printing, thus enabling fabrication of long (tens of meters), very smooth, submicron-thin THz structures.

4.5 Conclusion

Hollow core waveguides featuring a hyperuniform disordered reflector in the cladding are proposed for applications in the terahertz frequency range. The reflector consists of the disorderly

positioned dielectric cylinders that are connected with thin dielectric bridges. Center positions of the cylinders follow a hyperuniform disordered point pattern with the hyperuniformity parameter χ equal to 0.5. The proposed reflector structure was further optimized to maximize the photonic bandgap in the vicinity of 0.4THz, and the optimal bridge thickness and the cylinder diameter were found to be 35μm and 113μm, respectively. The resulting photonic bandgap features a full width of 90GHz (~21%).

Based on the numerically optimized waveguide structure, two hollow core waveguides with different bridge thicknesses were fabricated using a commercial 3D stereolithography printer. Due to resolution limitations of the printer, the resultant waveguides featured much wider bridge thickness (200μm and 250μm), while having the same overall structure of the reflector. We then theoretically investigated modal properties of the fabricated waveguides using a finite element method. Because of the suboptimal bridge thicknesses used in these waveguide, they exhibit smaller photonic bandgaps (~15%) when compared to those of the optimal structure. Finally, we performed optical characterization of the two fabricated waveguides using a modified THz-TDS system. For the fabricated waveguide with the bridge thickness of 200μm, spectral regions of enhanced transmission (bandgaps) are located at 0.17THz, 0.22THz and 0.29THz and 0.38THz, and the corresponding spectral widths are 18GHz, 22GHz, 44GHz and 49GHz, respectively, resulting in a maximum bandgap of ~15.1% at 0.29THz. When the bridge thickness is increased to 250μm, central frequencies of these bandgaps are shifted to 0.14THz, 0.17THz, 0.23THz and 0.29THz, respectively, and the corresponding spectral widths are reduced to 7GHz, 25GHz, 15GHz, and 45GHz. The maximum bandgap of this waveguide is measured to be ~15.3% at 0.29THz. The location and the widths of the experimentally measured bandgaps are in agreement with the theoretical predictions. Moreover, due to hollow core guidance, transmission losses (within the bandgap) of the fabricated waveguides are significantly smaller than the bulk absorption loss of the reflector material.

4.6 Experimental section

Fiber fabrication: The developed waveguides shown in this paper were fabricated using a commercial stereolithography 3D printer (ProJet® 3500HD Plus) with the photoresin (VisyJet® Crystal). In order to print robust structures, with this printer, the minimum feature size in the lateral directions is required to be at least twice the resolution ~200μm. Hence we could not print the

waveguide with the optimized structure. Instead of the optimized structure, we, therefore, printed two types of waveguides with bridge thicknesses of 200μm and 250μm, respectively, while keeping the same distribution of cylinders. For each waveguide, we printed four sections with lengths of 25mm each. As we used the same drawing file for the printing, these two waveguides have almost the same reflector size with ~22mm outer diameter and ~5mm diameter hollow core. The cross-sections of the fabricated waveguides are illustrated in Figures 1(c) and (e).

Support Information

S1. Optical characterization of the reflector material (VisyJet® Crystal)

In order to model the waveguide optical properties, first, we characterized the refractive index and absorption losses of the reflector material (VisyJet® Crystal) used in the waveguide fabrication. Characterization of the refractive index and absorption losses were performed using Zomega THz time-domain spectrometer (THz-TDS) using thin resin slices of different thicknesses, which were prepared using the same 3D printer. In the experiment, the complex transmission of these resin slices with different thicknesses are measured.

The real part of the resin refractive index and the absorption coefficient were extracted from the measured complex transmission data. In the analysis, multiple reflections within the sample were neglected. In this case, the measured complex transmission is given by:

$$\begin{aligned} T(\omega, L) &= \frac{E_t}{E_r} = |T(\omega, L)| \cdot \exp[i\varphi(\omega, L)] \\ |T(\omega, L)| &= C_{in} \cdot C_{out} \cdot \exp\left[-\frac{\alpha(\omega)L}{2}\right] \\ \varphi(\omega, L) &= -\frac{\omega}{c}(n_r(\omega) - 1)L \end{aligned} \tag{S1}$$

where E_t and E_r are complex transmission spectra measured with and without the tested sample with a length of L. C_{in} and C_{out} are the input and output coupling coefficient with respect to the tested sample, which are assumed to be the same during all samples. n_r and α are the real part of the reflective index and the absorption coefficient of the tested sample, respectively. In Figure. S1 (a) and (b), we present transmission spectra and corresponding phases of the tested samples with different thicknesses. Our analysis is limited to the frequency range of 0.2-1.0THz, where all the

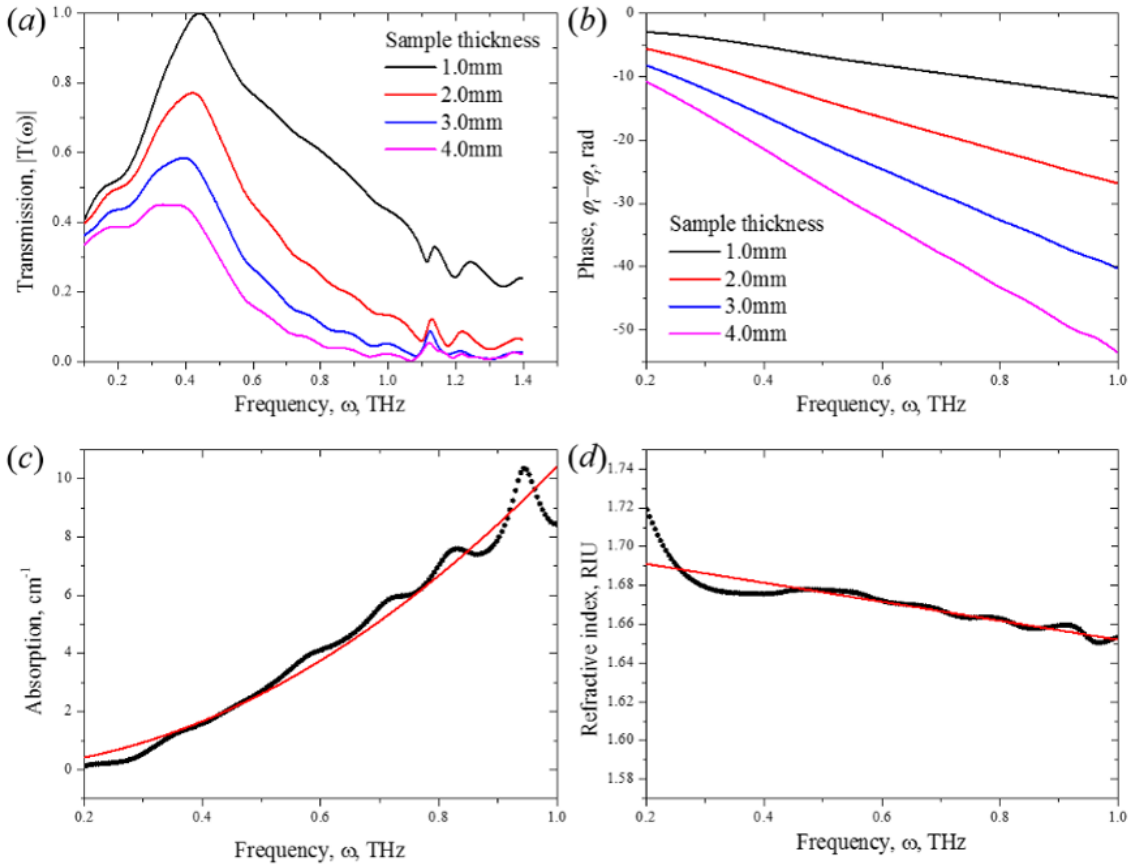

Figure 4.8. Optical characterization of the reflector material using cutback method and four 1mm-thick slices of the *VisyJet*® Crystal resin. (a) Normalized transmission spectra, (b) corresponding unwrapped phases, (c) the absorption coefficient and (d) the real part of the reflective index.

spectra are well above the noise level. For these frequencies, the absorption coefficient extracted from the measured data [Figure. 8(c)] can be fitted with a second order polynomial with respect to frequency:

$$\alpha(\omega)[cm^{-1}] = 10.43 \cdot (\omega[\mathrm{THz}])^2 \qquad \text{(S2)}$$

In Figure. 8(d), we demonstrate the frequency-dependent refractive index of the reflector material, which is retrieved using the unwrapped phase relative to the reference [see Figure. S2(b)]. In the frequency range of 0.2-1.0THz, the refractive index of the reflector material decreases almost linearly towards higher frequencies and can be fitted as:

$$n(\omega) = 1.701 - 0.049 \cdot \omega[\mathrm{THz}] \qquad \text{(S3)}$$

S2. Waveguide transmission measurements

In order to obtain the optical performance of the fabricated waveguides, we characterized their THz transmission using a modified terahertz time-domain spectroscopy (THz-TDS) setup shown in Ref. [23]. The setup consists of a frequency doubled femtosecond fiber laser (MenloSystem® C-fiber laser) used as the pump source and two identical GaAs dipole antenna (MenloSystem®) used as THz emitter and detector operating in the 0.1-3.0THz range. Figure. S2 illustrates the experimental setup where the waveguide under test is fixed in U-shaped 3D printed composite holder sections placed between two parabolic mirrors. Here, the printed holder sections can be divided into two types, namely external- and internal-holder sections [see Figure. S2(b)]. Two external holder sections were used to position the input and output facets of the waveguide with respect to the parabolic mirrors. The first external holder section was fixed in the focal point of the stationary parabolic mirror (PM1), thus, ensuring that the input facet of the waveguide was also at the focal point of PM1. At the input facet, an aluminum foil with a central hole of 5mm diameter was glued on the fixed external holder section, and it was used as an aperture to prevent the incoming beam from coupling into the waveguide cladding. The second external holder was mounted together with the parabolic mirror 2 (PM2) on a movable stage. At the same time, the second external holder section was fixed in the focal point of PM2. The internal holder sections hosting the waveguide were sandwiched between the two external holder sections, thus ensuring that the waveguide input and output ends were always in the focal points of the two parabolic mirrors. During the measurements, the three internal holder section that each hosted 2.5cm-long waveguide sections were removed one by one, and hence, waveguides of 10cm, 7.5cm, 5cm and 2.5 cm were measured. The measured electric field time domain THz traces and corresponding transmission spectra of these waveguides are shown in Figure. S3. The references shown here were acquired by removing all the internal holder sections (together with the waveguide sections), and minimizing the distance between the two external holder sections.

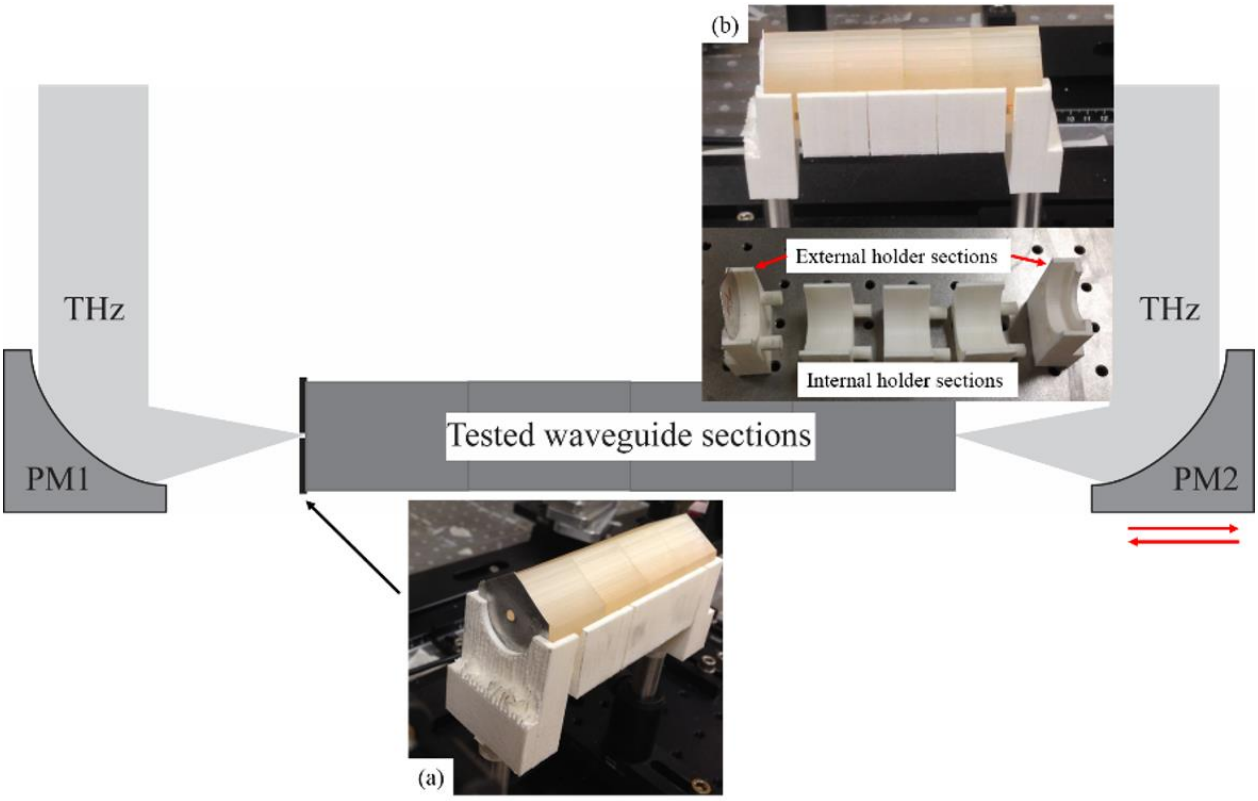

Figure 4.9. Schematic of the experimental setup with all of four waveguide sections mounted inside of a composite holder. Insert (a): the input facet of a waveguide features an aperture with the size equal to that of the waveguide hollow core. Insert (b): the 3D printed composite holder with sections before (bottom) and after (top) being insert into the experimental setup. PM1 – fixed parabolic mirror with a focus at the waveguide input edge. PM2 – movable parabolic mirror which is displaced every time the waveguide section is removed in order to keep the focal point at the waveguide output edge.

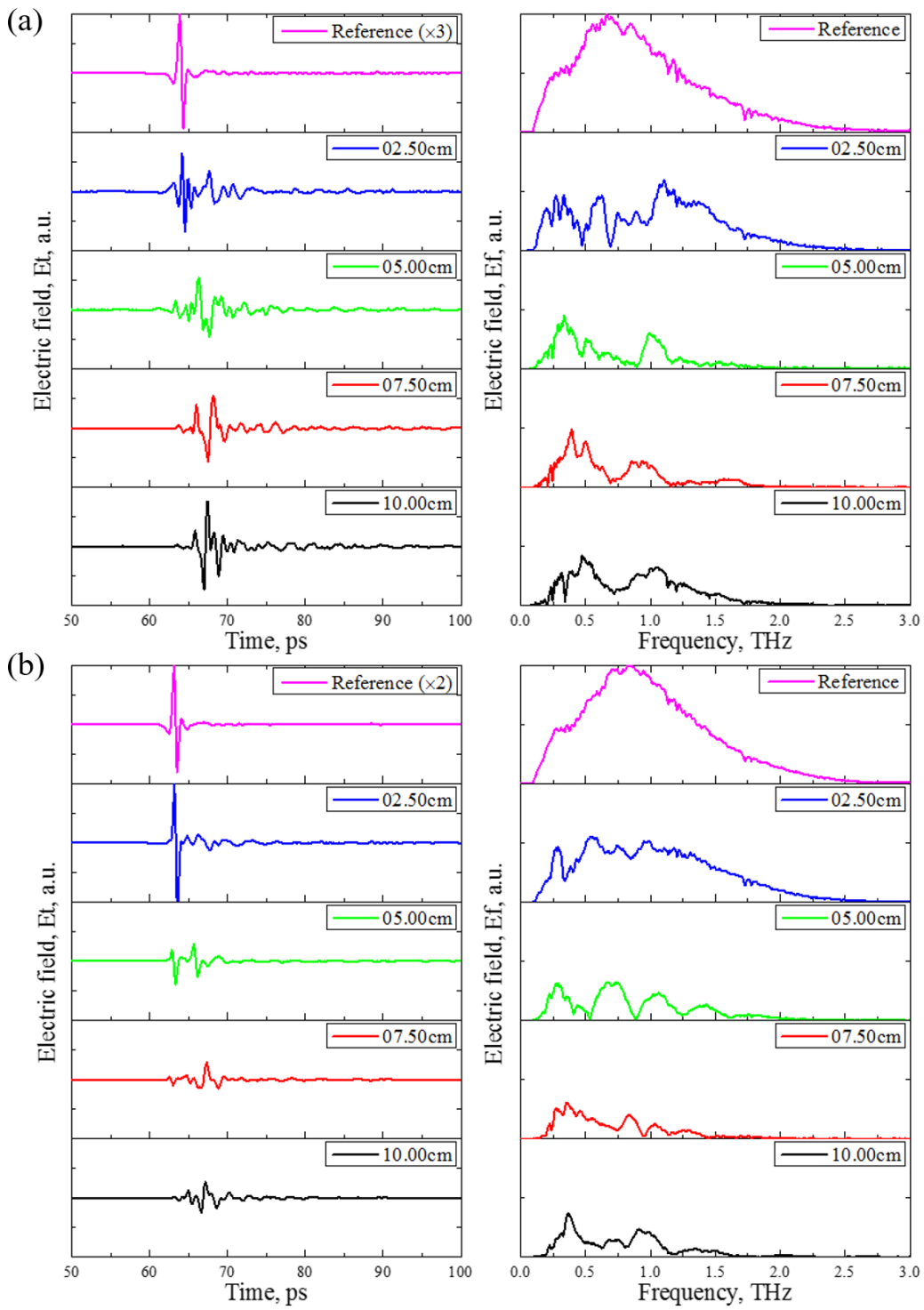

Figure 4.10. Experimentally measured electric field THz traces of the two waveguide with bridge thickness of (a) 200μm and (b) 250μm. Colors of the lines refer to waveguides of different length.

CHAPTER 5 ARTICLE 2 : GRADED INDEX POROUS OPTICAL FIBERS – DISPERSION MANAGEMENT IN TERAHERTZ RANGE

This chapter is based on my paper "Graded Index Porous Optical Fibers – Dispersion Management in Terahertz Range" published in *Optics Express* in 2015 [181]. I am the primary author of this paper, while this paper is co-written by Andrey Markov and Maksim Skorobogatiy from Ecole Polytechnique de Montreal, and Lili Wang from Xi'an Institute of Optics and Precision Mechanics, Chinese Academic of Science, China. My role in this paper includes the fuber structure design, numerical modeling and experimental characterization. I am responsible for all results shown in this paper.

In this chapter, I propose a novel porous fiber in a view of potential applications in low-loss and low-dispersion terahertz guidance. The fiber structure is initially designed to realise the graded refracitve index profile by using an air-hole array featuring variable air-hole diameters and inter-hole separations. Comparing with the regular porous fiber incorporating an air-hole array with uniform porousity, the proposed fiber features simultaneously low modal and intermodal dispersions, as well as low loss in the terahertz spectral range. Moreover, the proposed graded index porous fibers exhibit smaller pulse distortion, larger bandwidth, and higher excitation efficiency.

5.1 Introduction

The terahertz frequency range has strong potential for various technological and scientific applications, such as sensing, imaging, communications, and spectroscopy. However, most terahertz (THz) sources are immobile, thus designing efficient THz waveguides for flexible delivery of the broadband THz radiation is an important step towards practical applications of terahertz techniques. Moreover, THz waveguides can be very useful on the system integration level when used for connectorization of the diverse THz point devices, such as sources, filters, sensor cells, detectors, etc. Availability of the THz fibers is also crucial for various niche applications such as endoscopy and crevice inspection.

The main complexity in designing terahertz fibers is the fact that almost all materials are highly absorbent (over ~1 m propagation) in the THz spectral range. A traditional way of guiding light would be to use solid-core fibers, such as step index core/clad fibers, or solidcore microstructured fibers. In these fibers, however, the fraction of light guided in the solid core is

significant, and, therefore, fiber transmission loss is typically close to the absorption loss of the core material. For completeness we mention that in the 0.1-1 THz spectral range, amorphous materials suitable for fiber drawing (such as glasses and polymers) have losses that are typically higher than $0.1 - 0.3\ \mathrm{cm}^{-1}$.

In order to break away from the loss limit imposed by the fiber material absorption, subwavelength [38-40], porous [41–43], and hollow core THz fibers of various types [47–53] were introduced. The lowest absorption loss occurs in dry gases, therefore transmission losses of the THz fibers can be reduced significantly below the loss of the fiber core material by maximizing the fraction of the THz power guided in the low-loss gas. Using this strategy, very low transmission losses in the range of $0.3\ \mathrm{cm}^{-1}$ were demonstrated using the abovementioned fibers.

In particular, hollow core fibers are of great interest as they also tend to offer broadband guidance. Among such fibers one has to distinguish between dielectric photonic crystal fibers [181-182], metallized capillary fibers [80-81], and hybrid metal/dielectric fibers [88-90]. However, dielectric photonics crystal fibers and metallized capillaries require the use of relatively large core diameters in order to keep the propagation loss low. Therefore, such fibers operate mostly in the multimode or in the few-mode regime. In contrast, hybrid metal/dielectric fibers, which are essentially two wire waveguides surrounded by a porous dielectric cladding, operate in a single mode regime. On the same note, design of such fibers is challenging due to ease of parasitic excitation of the cladding modes, and it still remains to be seen if such fibers can show losses comparable to that of other hollow-core fibers.

Therefore, if the goal is to guide THz light over distances of $\sim 1\ \mathrm{m}$ in a single mode regime with losses on the order of $0.01\ \mathrm{cm}^{-1}$, then the only choices that are currently available are either using a subwavelength or porous fiber. When comparing porous and subwavelength fibers [38-43] it was found that porous fibers are generally superior to the rod-in-the-air subwavelength fibers as porous fibers offer larger bandwidth and lower bending loss.

Another complication when guiding broadband THz pulses is the effect of group velocity dispersion on the pulse shape. In fact, waveguide modes typically exhibit significant variation of their optical properties as a function of frequency (refractive index, group velocities, etc.), thus leading to pulse broadening, and hence, signal amplitude reduction. Consequently, waveguide dispersion management is an important issue when guiding broadband pulses. Dispersion

optimized single mode THz fibers have been first studied in [31,32,42]. Particularly, in [31,32] the authors used solid core microstructured fibers with optimized geometrical parameters to minimize group velocity dispersion of the fiber fundamental mode in the 0.2-1.2 THz frequency range. Dispersion of the fundamental mode was optimized to be less than 1 ps/(THz·cm) in the whole THz frequency range. However, due to guidance in the solid core, losses of such fibers were comparable to that of the bulk absorption loss of the fiber material $\sim 0.1 - 0.5\ \mathrm{cm}^{-1}$ (increasing towards higher frequencies). In [42], the authors studied dispersion and losses of the porous fibers and they have concluded that losses in such fibers could be significantly reduced below that of the core material loss by introducing porosity into the fiber core. At the same time, the authors of [31,32,42] have observed that both in solid core and porous fibers, group velocity dispersion can be very large at low frequencies due to rapid change in the modal confinement, while dispersion can decrease by more than an order of magnitude at higher frequencies (strong confinement limit). At higher frequencies, however, the fiber can become multimode and one has to worry about the effect of the intermodal dispersion.

Therefore, we conclude that when designing broadband dielectric fibers for THz guidance one must consider several trade-offs between dispersion, loss and single mode versus multimode operation. In order to demonstrate the nature of these trade-offs we consider guidance in the rod-in-the-air fiber of radius a having core and cladding refractive indices ε_c and ε_a, respectively. In our analysis we divide the whole frequency range into 3 spectral regions as shown in Figure 5.1. In the first region $\omega < \omega_0 \sim c/\left(a \cdot \sqrt{\varepsilon_c - \varepsilon_a}\right)$, the fiber is single mode and it guides in the weak localization regime. At these low frequencies one often calls the fiber a “subwavelength” fiber. In this regime, modal losses are much lower than the bulk absorption losses of the core material as a significant fraction of the modal fields is found outside of the fiber core and in the low-loss air cladding. In this regime, modal group velocity dispersion is also low as the mode is mostly guided in air. At the same time, macro-bending losses in this subwavelength guidance regime are very high as modal effective refractive index is very close to that of air, which typically renders subwavelength fibers unusable at frequencies significantly lower than ω_0.

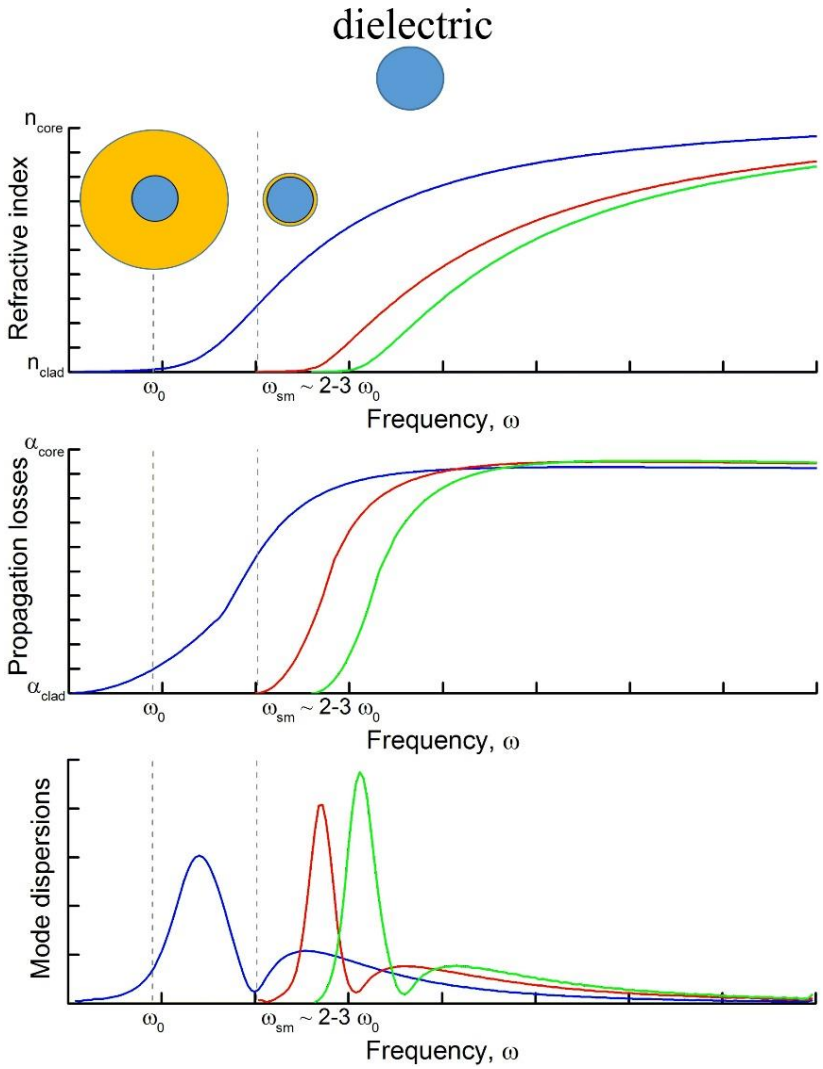

Figure 5.1 Modal propagation properties of the dielectric THz fibers. Blue lines correspond to the fundamental mode of the fiber, red and green lines – to higher order modes.

Next, we consider the second region $\omega_0 < \omega < \omega_{sm}$, where ω_{sm} is a cutoff frequency of the second order mode. In this frequency range the fiber is still single mode. Note that ω_{sm} and ω_0 are simply proportional to each other $\omega_{sm} \sim 2 - 4 \cdot \omega_0$ with a proportionality coefficient dependent on the symmetry of the second order mode that can be excited by a given THz source. In the vicinity of ω_0 the mode localization changes dramatically from a weak to strong localisation in the fiber core. This transition leads to a fast increase in the value of the modal refractive index, followed by a significant increase in the modal loss and modal group velocity dispersion. When increasing the operation frequency towards ω_{sm}, one observes a monotonic increase in the modal loss, which approaches that of the core material. Furthermore, modal group velocity dispersion decreases

significantly as the modal effective refractive index becomes virtually constant and close to that of the core refractive index. Additionally, at these higher frequencies macro-bending loss decreases dramatically due to improved modal confinement in the fiber core. So far, most of the experimental demonstrations of THz guiding were performed in this spectral range. It was clearly identified that high dispersion at lower frequencies and high propagation loss at higher frequencies present major challenges in the design of a solid-core THz fiber.

In principle, high modal loss at higher frequencies can be mitigated by using porous fibers with deeply subwavelength core size. In this case, absorption loss of the porous core can be made significantly lower than that of the constituent solid material. Additionally, modal group velocity dispersion decreases with lower refractive index contrast between the fiber core and cladding materials. Thus, using porous fibers can help in reducing both loss and group velocity dispersion of the fundamental mode.

Even when using porous materials in the fiber core, the fundamental limitation on the usable bandwidth is given by $0 < \omega < \omega_0$ where, as mentioned earlier, $\omega_{sm} \sim 2 - 4\omega_0$ in the rod-in-the-air fibers. This frequency range is quite limited as it spans less than an octave. The question then is how to extend the usable bandwidth of THz fibers. There are two approaches that one can pursue. One is designing microstructured fibers with an extended range of single mode operation. The other one is accepting multimode guidance, while at the same time optimizing fiber performance over an ensemble of the guided modes.

Multimode fibers (MMFs) offer several general advantages over single mode fibers such as high coupling efficiency and broadband operation. Moreover, in the multimode regime, most of the lower order modes show strong confinement in the fiber core, and, therefore, MMFs typically feature low modal group velocity dispersion, and low bending loss. As mentioned earlier, even at high frequencies modal absorption can be made significantly lower than absorption loss of the fiber core material by introducing subwavelength porosity into the fiber core. Moreover, a new phenomenon called intermodal dispersion has to be taken into account when considering THz pulse propagation in the multimode fibers. Simply speaking, an incoming pulse at the fiber input is split between several fiber modes. If the group velocities of the guided modes are somewhat different from each other, then various copies of the original pulse will arrive at the fiber output at different times, thus causing pulse shape degradation. In addition, when looking at a particular fiber mode,

the shape of the pulse carried by such a mode will be additionally affected by this mode group velocity dispersion. Therefore, reduction of both the modal and the intermodal dispersions presents an important problem when designing multimode THz fibers.

To date, multimode fibers have been exhaustively researched in the context of their application in short-length high bit-rate communication systems operating in the visible spectral range [184-186]. In such systems, fiber communication bandwidth is limited by the intersymbol interference caused by the intermodal dispersion, which arises because of the diverse group velocities of the individual fiber modes [26]. To address the issue of intermodal dispersion, graded index polymer optical fibers (GI-POF) have been extensively studied since the 1990s [115, 187, 188]. In such fibers, the core refractive index decreases from its maximal value at the core center as a certain power (~2) of the distance. As a result, intermodal group velocity dispersion can be dramatically reduced. In practice, in order to realize variable refractive index profiles in the fiber core one either uses a non-uniform distribution of dopants or a non-uniform distribution of geometrical features (such as holes). Thus, Y. Akimoto et al. [115] reported the fabrication and experimental investigation of the doped PSt-based GI-POFs. The graded refractive index distribution was achieved by controlling the radial dopant concentration. The authors confirmed that this fiber has a high bandwidth (4.4 GHz at 655 nm with fiber length of 50 m) and low attention (166-193 dB/km at 670-680 nm) and can be used for home networks. In [116], R. Lwin et al. reported another type of graded index fiber with graded index profile obtained by porous cladding with specially designed air hole positions and diameters, namely graded index microstructured polymer optical fibers (GI-mPOF). They demonstrated experimentally that the bandwidths of the proposed GI-mPOFs were much wider than those of the commercial GI-POF.

When designing multimode fibers for delivery of THz pulses we adopt the manufacturing strategy of graded index refractive index profiles using non uniform distribution of holes in the fiber core. However, when simply trying to scale the GI-mPOF design presented in [116] to THz wavelengths, the outer diameter of the resultant THz fiber becomes close to 5-10 cm, which is not practical. In fact, GI-mPOF presented in [116] does not contain subwavelength features (air holes), therefore the core material does not operate in the effective medium regime. Instead, the features are comparable or larger than the wavelength of light, and their size and position are optimized in order to provide a certain resonant response of the microstructured cladding. As a consequence, the diameter of such graded index fibers is in hundreds of wavelengths for which they are designed,

and obviously scaling of these fibers to THz will be impractical. Moreover, the GI-mPOFs developed for communications in the visible/near-IR have to operate in a very narrow spectral range as the signal bandwidth (~10 GHz) to the carrier frequency ($\sim 10^{14}$Hz) ratio is $\sim 10^{-4}$, whereas for THz GI-mPOFs this ratio is close to 1.

In this paper, we propose a novel graded index porous optical fiber which is specifically designed for applications in the terahertz spectral range (THz GI-POF). The fiber is made from polyethylene plastic and features a non-uniform array of the variable size subwavelength holes positioned at subwavelength separations with respect to each other, thus resulting in a graded refractive index effective medium. The outer diameter of the fiber is ~1.4 mm, which is at most 7 times larger than the wavelength of operation in the whole 0.2-1.5 THz operation range. The fiber is single mode below 0.35 THz, while at higher frequencies it operates in a few-mode regime. Due to high porosity, fiber absorption loss is only a fraction of the bulk absorption loss of polyethylene, and in the whole operation range it varies from 0.025cm^{-1} at 0.3 THz to 0.15cm^{-1} at 1.5 THz. Modal group velocity dispersion of the individual modes is reduced below 1 ps/(THz·cm) in the whole operational range due to the use of porous materials and due to the relatively large core size. At the same time, intermodal dispersion is reduced below 2 ps/(THz·cm) due to the choice of the graded index profile. Finally, we confirm experimentally and numerically that THz-GI-POFs have considerably superior optical properties when compared to regular THz porous optical fibers that feature similar geometrical dimensions, however only use a uniform array of holes. We believe that graded index porous optical fibers offer a clear pathway towards designing low-loss, broadband, low dispersion fibers for THz frequency range.

5.2 Fiber Design and Fabrication

In order to obtain a graded index profile similar to that of the conventional GI-POFs (see, for example Ref [115].) we use a hexagonal lattice of 5 rings of air-holes with gradually varied airhole diameters and inter-hole separations [as shown in Figure 5.2(a)]. In our design, the azimuthal average refractive index was approximated by the following power law:

$$n(r) = n_0(1 - a(r/R)^g)^{1/2} \tag{5.1}$$

where a is a constant which determines the index profile of the designed fiber, R is the radius of this fiber. In the case of porous fibers, local value of the core refractive index is determined by the

local value of the air filling fraction $f(r)$.Therefore, in order to design porous fiber geometry we have to first find the radially dependent air filling fraction $f(r)$ that results in the desired graded index profile given by Eq. (5.1). As detailed in [8], dielectric properties of the porous core can be described using an anisotropic dielectric permittivity tensor. Moreover, at higher frequencies, when transverse modal electric fields become much larger than the modal longitudinal electric fields, impact of anisotropy becomes small. In this regime, one can consider dielectric constant of the porous core material to be that of a transverse component of the dielectric tensor:

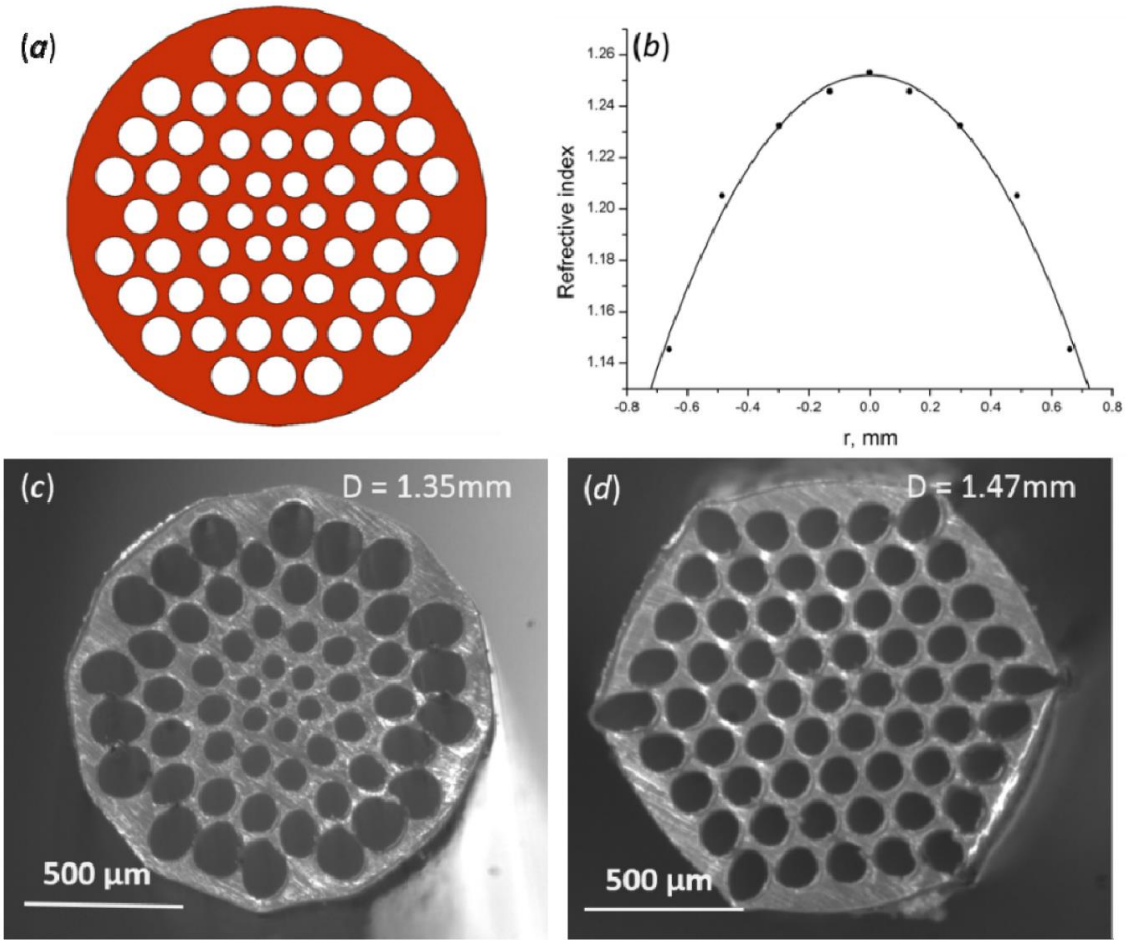

Figure 5.2 (a) The schematic representation and (b) the theoretical index profile of the designed GI-mPOF. The dots correspond to the localized refractive index at each layer, while the solid line is the theoretical index profile calculated using Eq. (5.2). The cross-sections of (c) GI-mPOF (outer diameter OD = 1.35mm) and (d) mPOF (OD = 1.47mm).

$$\varepsilon(r) = n(r)^2 = \sqrt{\left(\frac{1}{2} - f\right)^2 \cdot \Delta\varepsilon^2 + \varepsilon_a \varepsilon_p} + \left(\frac{1}{2} - f\right) \cdot \Delta\varepsilon \tag{5.2}$$

where ε_a and ε_p are the dielectric constants of the air and the used polymer, respectively, and $\Delta\varepsilon = \varepsilon_p - \varepsilon_p$. Now, using Eqs. (1) and (2), we can find the distribution of the air filling fraction $f(r)$ that results in the graded index profile given by Eq. (5.1). In our simulations we have used $g = 2$ and $a = 0.2$. Finally, using the expression for $f(r)$ at the air-hole center, we can extract the relation between the local value of the hole diameter d and the inter-hole separation Λ, which can be given as

$$f(r) = \frac{\pi}{2\sqrt{3}} \frac{d^2}{\Lambda^2} \tag{5.3}$$

The theoretical index distribution used in our simulation is depicted in Figure 5.2(b).

All fibers presented in this paper were fabricated using commercial rods of low density polyethylene (LDPE) known as one of the lowest absorptive polymers in the THz region [30]. The fiber preforms were fabricated using the drilling method. The air-hole arrays with designed structural parameters were drilled on the transversal surface of LDPE rods with an outer diameter of 1.5 inches and a length of 12 cm. Then the fabricated preforms were drawn down to fibers with an outer diameter (OD) of 1.3-1.5 mm in a fiber drawing tower. In order to make a reference measurement, a porous optical fiber with uniform diameters and interhole separations comparable to those of the GI-mPOF was also fabricated using the same material and fabrication technique. The cross sections of the two fibers are shown in Figure 5.2(c) and 2(d), respectively. The air filling fraction of fabricated GI-mPOF and mPOF are 43.3% and 43.0%.

5.3 Numerical Model and Simulation Results

To investigate the optical properties of the proposed GI-mPOF numerically, we used the commercial software COMSOL to solve for the complex effective index and field distribution of the guided modes. Figure 5.3 shows the calculated modal refractive index (n_{mod}) and group velocities (v_g) of the guided modes for the two fibers. In these figures, the dots' colors represent the logarithmic flux coupling coefficient (C_m^2). In the group velocity versus frequency graph we notice that the variation of the values of group velocities is smaller for the case of the GI-mPOF.

Correspondingly, the normalized amplitude coupling coefficient C_m is computed from the overlap integral of the respective flux distribution of the m-th mode with that of the 2D Gaussian beam used as a source. Specifically, the definition of C_m is based on the continuity of the transverse field components across the input interface (i.e. cross-section of the fibers) between the incident beam and the excited fiber modes:

$$C_m = \frac{1}{4}\int dxdy\left(\boldsymbol{E_m^*}(x,y)\times\boldsymbol{H_{input}}(x,y) + \boldsymbol{E_{input}}(x,y)\times\boldsymbol{H_m^*}(x,y)\right) \times \frac{1}{\sqrt{\frac{1}{2}\mathrm{Re}\left[\int dxdy\left(\boldsymbol{E_m^*}(x,y)\times\boldsymbol{H_m}(x,y)\right)\right]}\times\sqrt{\frac{1}{2}\mathrm{Re}\left[\int dxdy\left(\boldsymbol{E_{input}^*}(x,y)\times\boldsymbol{H_{input}}(x,y)\right)\right]}} \quad (5.4)$$

To model the field structure of the source, we assume an x-polarized 2D Gaussian beam whose fields are normalized to carry power *P*, then limited by an aperture of radius *R* as follows:

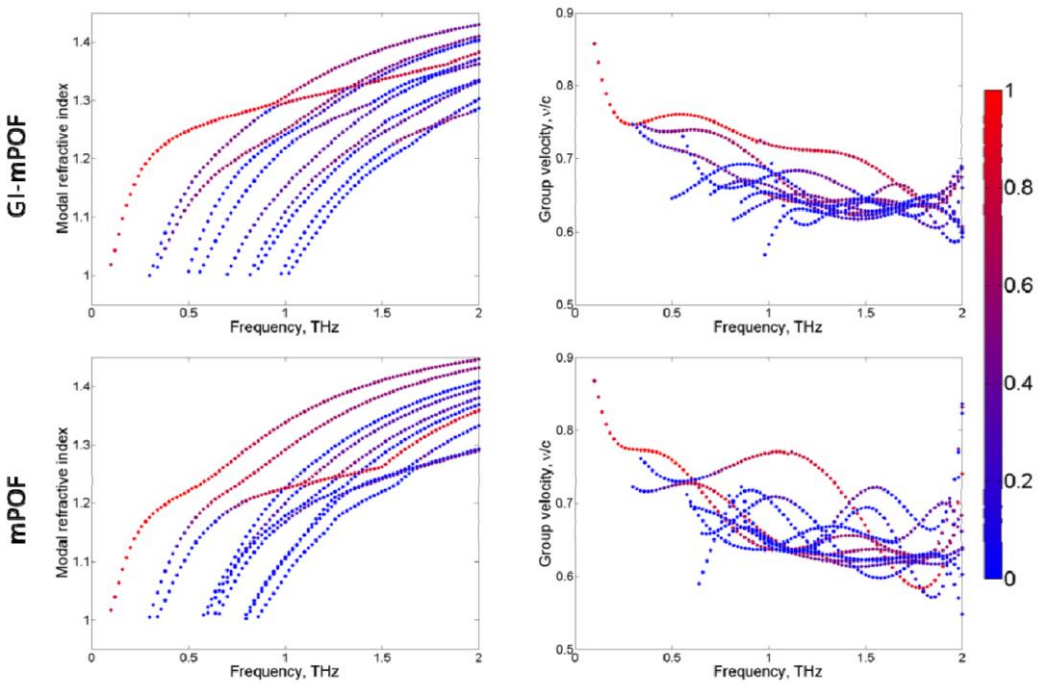

Figure 5.3 The modal refractive indices and the group velocities of the proposed GI-mPOF and the traditional mPOF. The dots' colors represent the logarithmic flux coupling coefficient of each mode at the given frequency.

$$\begin{aligned} \boldsymbol{E_{input}}(x,y) &= \vec{x}\cdot\sqrt{\frac{2P}{\pi\sigma^2}}\cdot\exp\left[-\frac{x^2+y^2}{2\sigma^2}\right] \\ \boldsymbol{H_{input}}(x,y) &= \vec{y}\cdot\frac{1}{\sqrt{\mu_0/\varepsilon_0}}\cdot\sqrt{\frac{2P}{\pi\sigma^2}}\cdot\exp\left[-\frac{x^2+y^2}{2\sigma^2}\right] \end{aligned} \quad ,for\ x^2+y^2\le R^2$$
$$\boldsymbol{E_{input}}(x,y)=0, \boldsymbol{H_{input}}(x,y)=0, for\ x^2+y^2>R^2 \tag{5.5}$$

where the Gaussian beam waist parameter σ is related to the full-width hall-maxima by field as $FWHM = 2\sigma\sqrt{2ln2}$, $\vec{x}$ and $\vec{y}$ are the unit vectors in x- and y-directions, $\sqrt{\mu_0/\varepsilon_0}$ is the intrinsic impedance of vacuum, and R is equal to the radius of the fiber ($\sim$0.65 mm). The frequency dependence of the beam waist was measured experimentally and then fitted by a linear function of the input wavelength $\sigma = 0.96\lambda + 1.4$ mm.

As shown in Figure 5.4, the fundamental mode of the GI-mPOF (shown as the blue curve) is predominantly excited in the entire frequency range, whereas coupling into higher order modes is correspondingly lower as opposed to the fiber with uniform holes. In the case of traditional mPOF, higher order modes have higher coupling coefficients compared to the fundamental mode (black curve) above 0.7 THz.

Based on the modal refractive indices and group velocity, we calculated the individual mode (or waveguide) dispersion ($\sqrt{\langle D^2\rangle}$) and the intermodal dispersion ($\sqrt{\langle \Delta v_g^{-2}\rangle}$). The waveguide dispersion was computed based on the first order derivative of the modal propagation constant. The intermodal dispersion was defined as the standard deviation of the modal delay and can be given as:

$$\langle \Delta v_g^{-2}\rangle = \langle v_g^{-2}\rangle - \langle v_g^{-1}\rangle^2 \tag{5.6}$$

where $\langle M\rangle$ denotes the average of the variable M and is defined as $\langle M\rangle = \sum_j M_j C_j^2$. Assuming pulse intensity is given by $I(t,0)\sim\exp\left[-\left(\frac{2t}{\tau_0}\right)^2\right]$ at the fiber input $z=0$, pulse width after propagation over a fiber length z can be found as follows:

$$\langle \tau^2(z)\rangle = \frac{\tau_0^2}{8} + z^2\left(\left[\langle v_g^{-2}\rangle - \langle v_g^{-1}\rangle^2\right] + 2\frac{\langle D^2\rangle}{\tau_0}\right) \tag{5.7}$$

where one can see the contribution of intermodal and individual mode dispersions into pulse broadening. For the calculations we assume that the initial pulse is 1 ps long.

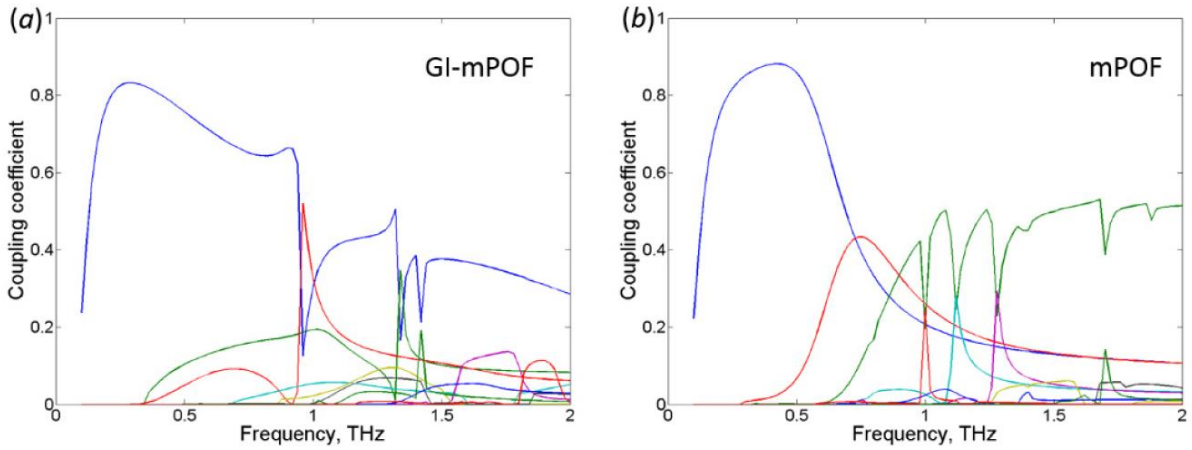

Figure 5.4 The coupling efficiency by power for (a) the proposed GI-mPOF and (b) the traditional mPOF

In Figure 5.5, we depict the results of the computation for the two dispersion types for both the proposed GI-mPOF and the traditional mPOF. As we can see from Figure 5.5, both the individual mode dispersion and the intermodal dispersion of the GI-mPOF has been reduced significantly compared to the traditional mPOF. Therefore, we expect that the proposed fiber structure will considerably decrease the pulse width broadening by both lowering the impacts of higher order modes and by reducing intermodal dispersion.

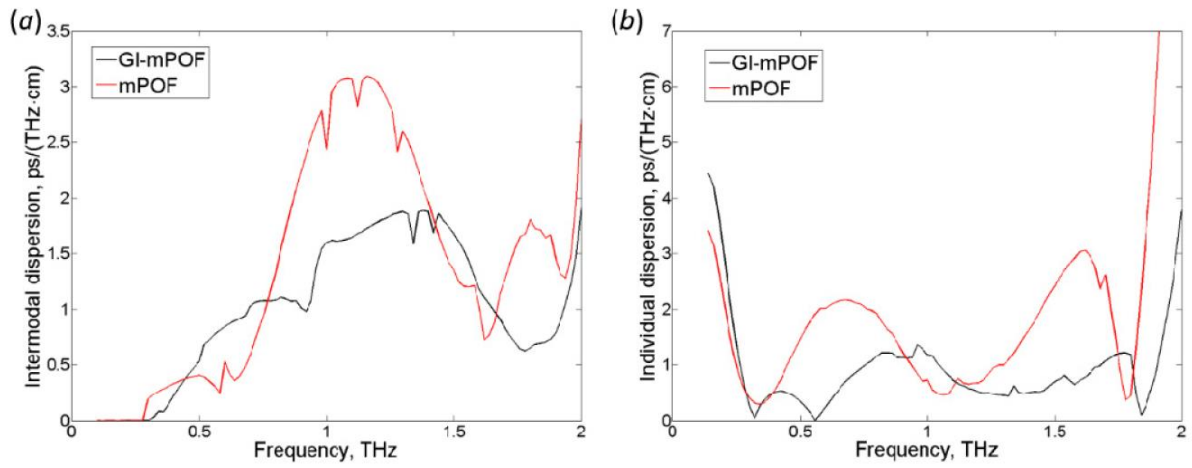

Figure 5.5 (a) The individual mode dispersion and (b) the intermodal dispersion of the two fibers. The red solid lines are the dispersion properties of the proposed GI-mPOF, while the black lines show that of the traditional mPOF.

5.4 THz-TDS measurements

All the measurements in our experiment were obtained by using a modified terahertz timedomain spectroscopy (THz-TDS) setup. The setup consists of a frequency doubled femtosecond fiber laser (MenloSystems C-fiber laser) used as pump source and two identical GaAs dipole antennae used as a THz emitter and a detector yielding a spectrum range of 0.1 to 3.0 THz. However, because of the lower dynamic range and increased material losses in the fiber at higher frequencies, we only considered the spectrum range of 0.2 to 1.5 THz in the following sections.

With a parabolic mirror mounted on the translation rails, our setup allows for the measurement of waveguides up to 45 cm long. Figure 6 illustrates the experimental setup where the fiber was fixed by apertures and placed between the two parabolic mirrors. To obtain the transmission properties of the fiber, we used the cutback method in the measurement. The input facet of the fiber was fixed by being glued to an aperture, while the output facet was cut in steps. Both the input and output ends of the fiber were placed at the focal points of the parabolic mirrors.

In Figure 5.7, we present three temporal traces of the THz electric field measured at different fiber lengths. As expected, based on the simulations, lower intermodal dispersion of the GI-mPOF leads to the reduction of pulse broadening. With a lower difference of the group velocities, most of the modes reach the output end of the fiber in one envelope. Other higher order

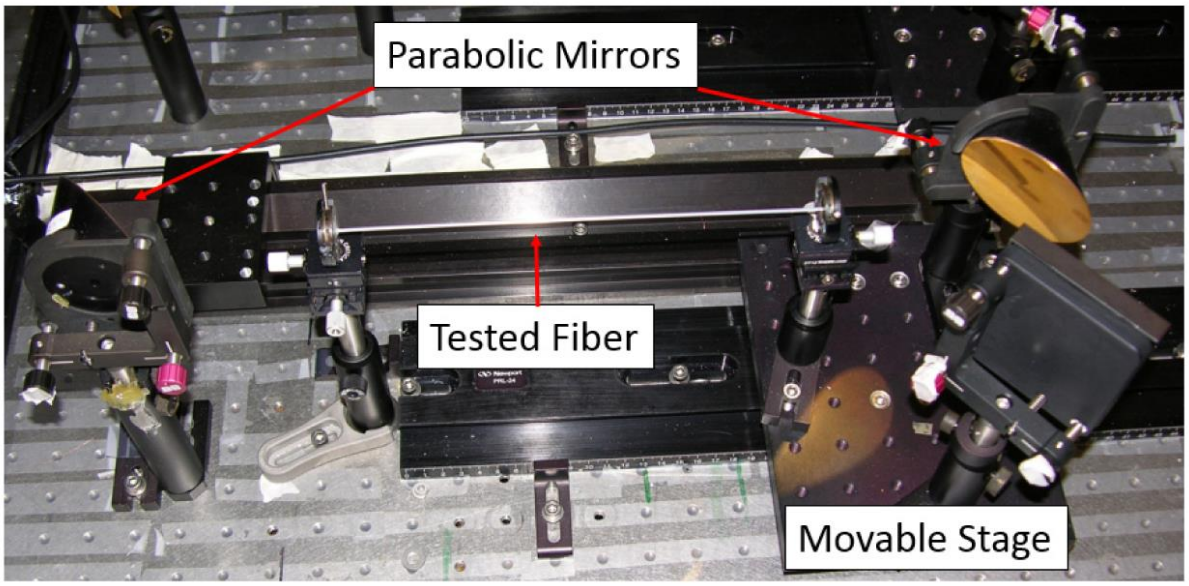

Figure 5.6 Experimental setup with the fiber mounted in the apertures.

modes with larger mode delay were also restrained because of the low coupling coefficients. Meanwhile, in the case of the traditional mPOF, the output pulse has been separated into several groups because of the higher difference of the modal group velocities.

Another interesting phenomenon can be observed from the temporal traces of the two fibers. The output electric field of the traditional mPOF is much smaller than that of the proposed GI mPOF. This feature is caused by the weaker mode confinement of the traditional mPOF. As shown by the simulated distribution of the fundamental mode at 0.5 THz [see Figure 5.7 (b)], the mode of the proposed GI-mPOF is mostly concentrated in the central region of the fiber. Meanwhile, in the case of the traditional mPOF, the fundamental mode leaves the core and propagates mainly on the

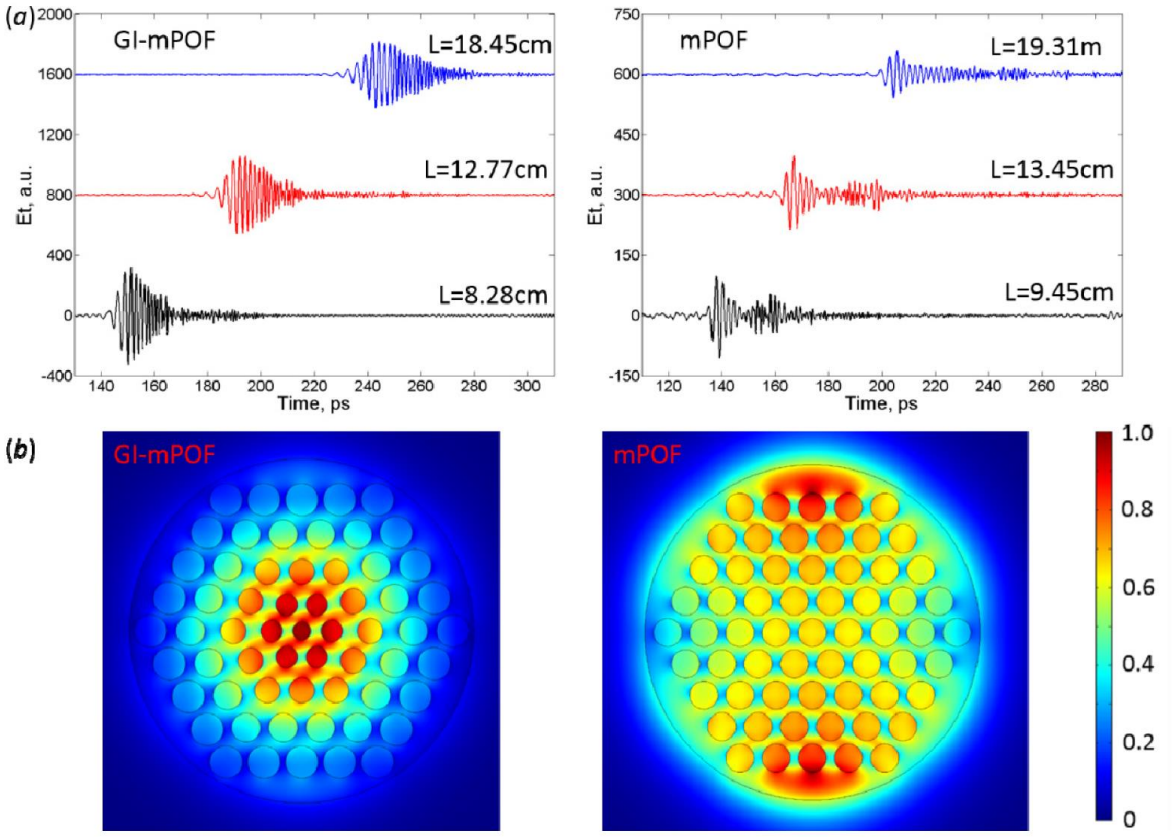

Figure 5.7 (a) The time-domain traces of the THz electric field measured at different fiber lengths of the proposed GI-mPOF (left) and the traditional mPOF (right). The black trace represents the THz field after propagating a short distance in the fiber; the red trace represents a longer distance, and the blue trace is for the whole fiber. The initial lengths of the fibers used in the experiment are about 20 cm. (b) Mode profiles simulated at 0.5 THz for these two fibers.

plastic/air interface. In our experiment, this evanescent field is blocked along with stray light by the metal aperture and partly absorbed by the glue.

Because of the dispersions of the tested fiber, the input pulse with a very narrow pulse width will expand into a broader one. To investigate the pulse broadening caused by multimode propagation, we reconstructed the output pulses based on the simulation results. The reconstructed pulse at the output facet of a waveguide of length L is modeled as the inverse Fourier transform of transverse electric output field which is the coherent superposition of N guided modes where N = 50 for both the designed GI-mPOF and traditional mPOF.

$$\boldsymbol{E}(t) = \int d\omega \sum_{m} C_m(\omega) \cdot \exp[i(\beta L - \omega t)] \iint dxdy \boldsymbol{E_m}(x, y, \omega) \tag{5.8}$$

where $\boldsymbol{E_m}$ stands for the normalized transverse field components of *m*-th guide mode. The variable β denotes the propagation constant. In Figure 5.8, we present the reconstructed pulses based on the simulation results. The experimental measured pulse of both these two fibers can be well explained by the numerical simulations. As we only considered the theoretical modal distribution here, both the coupling and launch conditions at the input ends would introduce some mismatch between the experimental and numerical results.

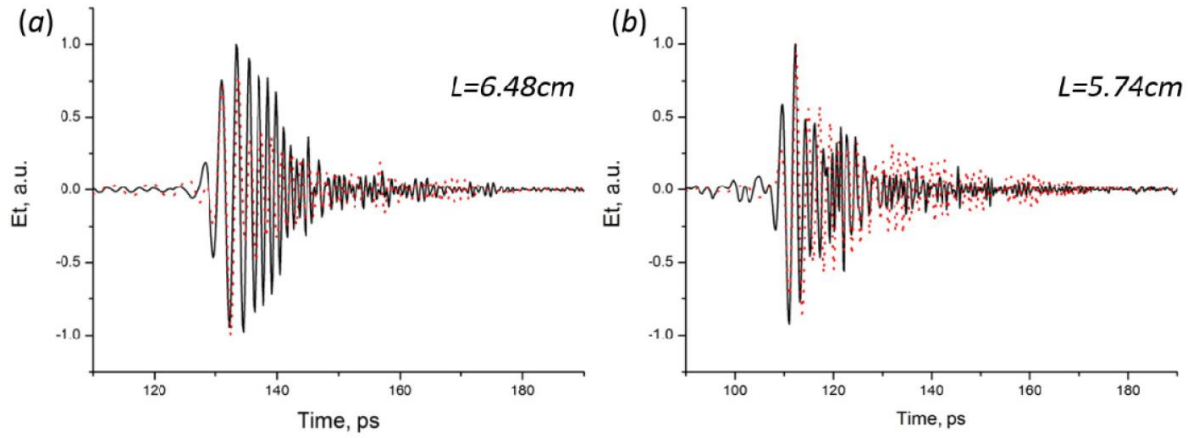

Figure 5.8 The comparison between measured pulse and reconstructed pulse for (a) the GI-mPOF with 6.48 cm length and (b) the mPOF with 5.74 cm length. The black solid line represents the experimentally measured electric trace, while the red dot line corresponds to the reconstructed pulse based on the simulation results.

Using the aforementioned numerical model, we also calculated the pulse width at different propagation lengths in these fibers. In Figure 5.9, we present both the experimental and theoretical values of the pulse width. The experimental values of the pulse width (dots in Figure 5.9) can be found by calculating the time averages:

$$\langle \tau^2 \rangle = \langle \boldsymbol{E_t} | t^2 | \boldsymbol{E_t} \rangle / \langle \boldsymbol{E_t} | \boldsymbol{E_t} \rangle - (\langle \boldsymbol{E_t} | t | \boldsymbol{E_t} \rangle / \langle \boldsymbol{E_t} | \boldsymbol{E_t} \rangle)^2 \tag{5.9}$$

where $\boldsymbol{E_t}$ refers to the measured time-domain electric field trace propagating along a fiber length L. To compute the theoretical values of pulse duration, we calculated the pulse duration based on Eq. (5.9) where we replace the measured time-domain electric field traces by the reconstructed temporal pulses; it is depicted in Figure 5.9 as solid lines. We note that for both of these two fibers, the pulse width has a L^2 dependence within some equilibrium length (L_e). Beyond this equilibrium length, the pulse width is nearly proportional to the fiber length. The value of L_e for the designed GI-mPOF is approximately 5 cm, while that of the mPOF is about 16 cm. The dashed lines in Figure 5.9 are fitted using the Eq. (5.7) by calculation the pulse duration within L_e. The difference beyond L_e arises from the fact that the Eq. (5.7) is valid only for narrow bandwidth Gaussian pulses, whereas we operate with THz pulses that have very large spectral ranges. We also note that in the case of the mPOF, the weaker pulse amplitude leads to greater values of the pulse duration uncertainties as compared to that of the designed GI-mPOF.

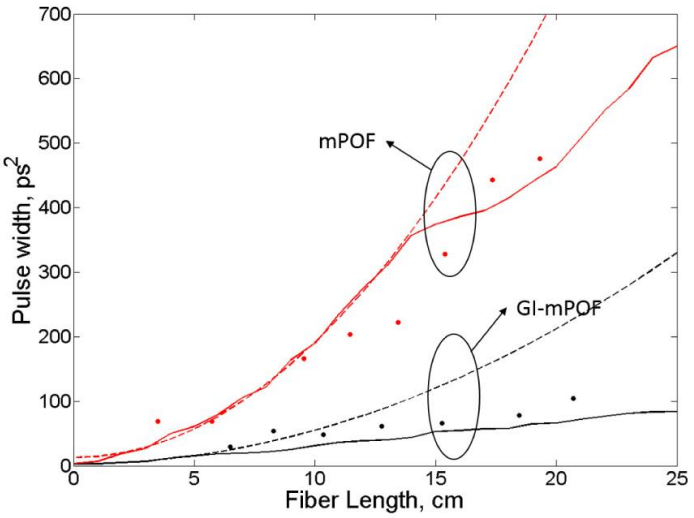

Figure 5.9 The pulse duration of the designed GI-mPOF (black) and the mPOF (red). Dots - experimental results. Dashed lines - results of the fitting based on Eq. (5.7). Solid lines – pulse duration calculated based on the reconstructed pulses.

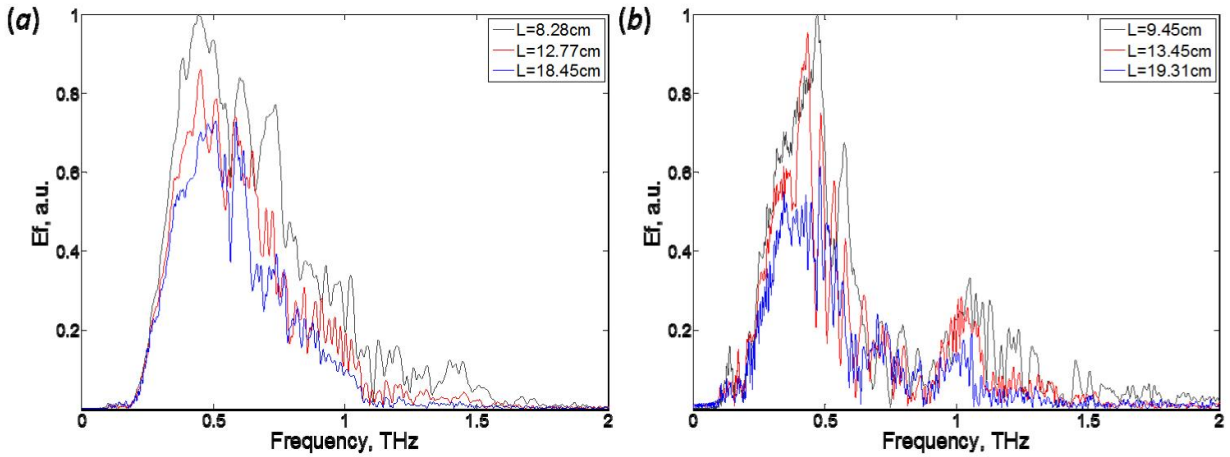

Figure 5.10 Electric field amplitude as measured by the THz-TDS setup for the case of (a) GI-mPOF and (b) mPOF.

In Figure 5.10, we present experimentally measured transmission spectra for different lengths of the GI-mPOF and mPOF corresponding to the time-domain traces shown in Figure 5.7(a) and (b), respectively. We note that a broader transmission band from 0.2 to 1.5 THz is observed for the proposed GI-mPOF, whereas transmission merely stops at 0.8 THz and has a small peak at around 1.0 THz in the case of the traditional mPOF. Another notable feature in the measured transmission spectrum of the mPOF [Figure 5.10(b)] is the amplitude fluctuation in the higher frequency region (higher than 0.40 THz). This fluctuation is caused by the interaction of higher order modes. As shown in Figure 5.4, in the case the mPOF, higher order modes occupy more modal power in the higher frequency region, thus the modal beating is more pronounced.

5.5 Conclusion

A graded index microstructured fiber designed for reducing intermodal dispersion has been proposed for applications in the THz range. The radially graded index distribution of the proposed fiber is achieved by an air-hole array featuring variable air-hole diameters and interhole separations. Large air holes at the outer layers of the proposed GI-mPOF lead to a better modal confinement at the center of the fiber and enhance the output electric field, as compared to the traditional mPOF with uniform air-hole diameters and lattice constants.

In this paper, we theoretically investigated the modal properties of the proposed GI-mPOF and the traditional mPOF using a finite element method. The fiber is single mode below 0.35 THz, while at higher frequencies it operates in a few-mode regime. The simulation results demonstrate

that the proposed GI-mPOF design suppresses the excitation of higher order modes and reduces the intermodal dispersion. At the same time, both the intermodal and individual dispersion of the designed GI-mPOF are smaller than that of the traditional mPOF leading to a smaller broadening in the designed graded index fiber. Modal group velocity dispersions of the individual modes is reduced below 1 ps/(THz·cm) in the whole operational range due to the use of porous materials and due to the relatively large core size. At the same time, intermodal dispersion is reduced below 2 ps/(THz·cm) due to the choice of the graded index profile.

We also experimentally and numerically confirmed that the designed GI-mPOFs have considerably superior optical properties when compared to the traditional mPOF. Due to high porosity, fiber absorption loss is only a fraction of the bulk absorption loss of polyethylene, and in the whole operation range it varies from $0.025\mathrm{cm}^{-1}$ at 0.3 THz to $0.15\mathrm{cm}^{-1}$ at 1.5 THz. The transmission of these two fibers was also measured utilizing a THz-TDS setup using the cut-back method. According to the experimental results, the proposed fiber structure improved the output pulse quality as all the modes reach the output facet of the fiber in one time-domain envelope. We also reconstructed the output pulses based on the simulation results and calculated the pulse duration. Both the experimental and numerical results show that the pulse broadening has been well restrained by the designed fiber structure, as the pulse duration of the designed GI-mPOF is much smaller than that of the traditional mPOF, with the difference between the fibers being the most pronounced for long fiber lengths. Simultaneously, the transmission band of GI-mPOF is significantly wider than that of porous fibers due to better suppression of the excitation of higher order modes.

CHAPTER 6 DISPERSION COMPENSATION FOR TERAHERTZ COMMUNICATION USING 3D PRINTED HOLLOW CORE WAVEGUIDE BRAGG GRATING

In this chapter, novel hollow core terahertz waveguide featuring periodic structure at its inner surface is proposed for dispersion compensation in the vicinity of 0.14THz. First, we begin with the principle of dispersion compensation in the terahertz frequency range. Then, we will discuss the theoretical performance and show an experimental implementation of the fabricated waveguide Bragg grating.

6.1 Principles of dispersion compensation

With the demand of wider bandwidths and higher bit rates, using terahertz frequencies for wireless communications is experiencing a surge of attention in recent years. Various THz wireless communication systems with carrier frequencies as high as 0.6THz and transmission data rates of up to 100Gbit/s have been developed and investigated [12,13,20,21]. However, applications of these THz communication systems are still limited due to inherent challenges posed by the free space propagation (FSP) modality, such as strong dependence on atmospheric conditions, rapid divergence of the THz beams especially at the lower carrier frequencies, as well as light-to-sight nature of the links. Particularly, due to self-diffraction and THz relatively long wavelength $\sim$1mm, realizing low divergence THz beams requires the use of large beam diameters and focusing optics that can be as big as several tens of centimeter in diameter for even short communication links of several tens of meters. Additionally, due to strong directionality of the THz beams, wireless communications access to partially blocked areas can be problematic, thus, requiring additional THz steering and routing solutions for reliable communications.

One the other hand, low-loss terahertz fibers and waveguides offer good solutions to some of the limitations caused by free space THz propagation, and can have their own wide applications. Particularly, light propagates through sealed THz fibers, thus, influence of the atmospheric conditions on the communication link quality is minimized. Additionally, THz fibers are flexible and of small diameters, hence, allowing access to otherwise physically obstructed areas. Finally, THz fibers size is typically comparable to the wavelength of light, thus enabling compact several mm in diameter communication links with small footprint that can be used as on-chip

interconnects. In the past decade, various THz fibers with low transmission losses (<0.01 cm-1) have been proposed and demonstrated. Generally, such waveguides maximize the fraction of the guided power in the low-loss gas. Among these designs, one generally distinguishes subwavelength THz fibers that guide using total internal reflection (TIR) mechanism [38-44] and hollow core fibers that guide using either photonic bandgap confinement [47-58] or anti-resonant reflection (ARROW) [59-72].

While loss reduction in THz fibers can be considered as a solved problem, dispersion management remains generally an unsolved problem. GVD, or group velocity dispersion, results in strong pulse spreading in TDS system. In communication systems, GVD also leads to pulse broadening, and hence reduction in the maximal bit rate supported by the communication link of fixed length. This happens because adjacent "bits" of temporal size Δt in the pulse train broaden after propagation over length L in the fibers with GVD D, as $D \sim \Delta L/\Delta t$. One considers that the pulse train gets scrambled when adjacent "bits" overlap which happens if $\Delta t \propto 1/\sqrt{D \cdot L}$ [26]. For example, considering a typical fiber dispersion $D \sim 10\ \mathrm{ps/(THz \cdot cm)}$, to obtain even a moderate bite rate of $10\mathrm{Gbit/s}$, the maximum transmission length in a dielectric fiber is limited to ~10 m. On the other hand, transmission rates of $100\ \mathrm{Gbit/s}$ would limit transmission links to only 10 cm with standard THz waveguides. Note that even in the wireless links, dispersion of air at THz frequencies is $D \sim 2.5\times10^{-4}\mathrm{ps/(THz \cdot cm)}$ [189-190], thus limiting the $100\ \mathrm{Gbit/s}$ wireless link to 400 m. In addition to pulse deformation due to group velocity dispersion, frequency dependent absorption loss due to water vapor will further contribute to pulse deformation. Therefore, while effects of dispersion can be modest in free space links, they are a major limiting factor in waveguide-based interconnects. One way of reducing the GVD of a THz waveguide link is via a judicial design of the waveguide geometry.

For example, in our previous work [179], we have demonstrated a graded porous THz fiber incorporating an air-hole array featuring variable air-hole diameters and inter-hole separations. Comparing with its counterparts featuring regular air-hole array, the proposed fiber successfully reduced both the individual modal and intermodal dispersions and improved the spectral transmission range.

Further reduction of the GVD below $0.1\mathrm{ps/(THz \cdot cm)}$ proved to be challenging and there are few examples in the literature of such THz waveguides. In order to address this issue, one can

pursue an alternative approach. Thus, instead of reducing GVD of a transmission link, one can rather use dispersion compensation at the link end, or dispersion precompensation at the beginning of the link. There are several requirements for effective dispersion compensation systems. One is effective coupling at the link end and into the dispersion compensator. Second is single mode operation, in order to avoid multimode interference effects and intermodal dispersion. Third is the requirement of the high negative dispersion of the dispersion compensating waveguide D_{DCW} in order to compensate with a short device length L_{DCW} for the positive dispersion D_L incurred in long L_L link such that $D_{DCW} \cdot L_{DCW} + D_L \cdot L_L = 0$, with $L_{DCW} \ll L_L$. Finally, dispersion compensation condition has to be satisfied over a with enough frequency range comparable to the communication signal bandwidths. In THz wavelength, some of these conditions can be satisfied with large diameter metallic tubes that can show excellent coupling with a focused THz beam and high value of the negative GVD near the modal cut-off frequencies.

In Figure 6.1(a), we schematically show dispersion relations of the fundamental mode and the first higher order mode for a circular metal tube, where ω_1 and ω_2 are the cutoff frequencies for the fundamental mode (black line) and the first higher order mode (red line). For frequencies between ω_1 and ω_2, metal tubes support a single mode guidance with negative dispersion [light blue region in Figure. 6.1(a)]. As optical characteristics of such waveguides are strongly dependent on the core size, one should consider trade-offs between the core size and the value of negative dispersion, as well as single mode versus multimode operation, when using such waveguides for dispersion compensation. For example, the dispersion relation of guided modes in a metal tube of radius *r* is given as [191]:

$$\beta_{mn} = \sqrt{\omega^2 - (\omega_c^{mn})^2} \tag{6.1}$$

where $\omega_c = X_{mn}c/r$ is the modal cutoff frequency, and X_{mn} is the n-th nonvanishing root of the m-th order second kind Bessel function $Y_m(\omega)$ (for TE modes) or the m-th order first kind Bessel function $J_m(\omega)$ (for TM modes). If λ is the operational wavelength, single mode regime is realized for the tube radii of $0.29\lambda < r < 0.38\lambda$. A typical beam waist size of the focused diffraction limited THz beam is $w \sim \lambda \frac{2M^2 f}{\pi D}$ [192], where f and D are the focal distance and diameter of the focusing lens, respectively, with field intensity dependent as $|E|^2 \propto \exp[-2r^2/w^2]$. In our system, we use $f = 2D = 10\text{cm}$. Assuming $M^2 \sim 1.5$, we get that $w \sim 2\lambda$. We note that in order to achieve efficient coupling, the tube size has to be lager than the Gaussian beam size, namely $r \geq$

w. However, when trying to operate near the first cutoff frequency, the tube radius should be $r \approx 0.29\lambda \ll w_0 \approx 2\lambda$, which leads to inefficient coupling to the tube fundamental mode near its cutoff frequency.

In order to increase coupling coefficient of the focused Gaussian beam and a hollow-core tube, one, therefore, needs to simply increase the tube diameter, or alternatively increase the operation frequency. However, this make the tube multimode The question, therefore, is how to how to make tubes of larger diameters effectively single mode. This can be achieved by introducing periodic patterns to the tuber core and opening a bandgap for higher order modes [gray region in Figure. 6.1(b)]. Now, operation in this frequency region is single mode, light guidance is still in the fundamental tube mode. Operation at higher frequencies allows better mode matching between the focused Gaussian beam and the core guided mode, and finally, strong negative dispersion is achieved, when operating close to the upper edge of the bandgap of the fundamental mode.

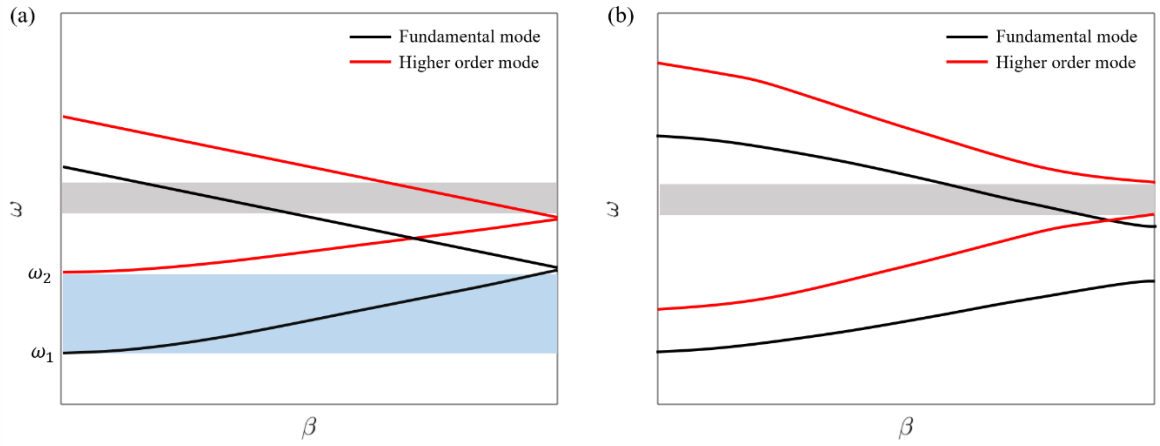

Figure 6.1 Dispersion relations of (a) metal tube and (b) hollow core waveguide Bragg grating. Black line: fundamental mode; red line: first higher order mode.

In this chapter, we explore a novel THz waveguide Bragg grating based on the corrugated hollow core metal tubes for dispersion compensation in terahertz communication links. The proposed waveguide was fabricated from photosensitive resin using 3D stereolithography, which currently used as a choice for fabrication of optical devices for terahertz frequencies [176-178]. Subsequently, the printed devices were metallized with silver microlayers using the wet chemistry. As we demonstrated, both theoretically and experimentally, the single mode guidance and negative dispersions for the fundamental mode are achievable in the vicinity of the operation frequency of

~140GHz. This is a choice for our upcoming THz communication setup, as it has highest power and detection sensitivity in the vicinity of this frequency. Furthermore, field distribution of the modal profiles for both waveguides were confirmed using THz imaging setup. The fabricated waveguide Bragg grating features a sizable transmission band (~7 GHz) for the fundamental mode and large negative dispersion (~-130 ps/(THz·cm)) in the vicinity of 140 GHz.

6.2 Waveguide fabrication

The waveguide Bragg grating is realized by introducing triangular steps inside of a hollow core tube of diameter $D = 9.0\text{mm}$. Bragg grating comprises of 40 periodically arranged triangular steps of the base size $p = 1.35\text{mm}$ and the height of $h = 1.9\text{mm}$. The 3D model of the proposed waveguide Bragg grating is shown in Figure. 6.2(a). The structure was optimized to enable effectively single mode propagation of a chosen guided mode in the vicinity of 0.14THz, as detailed in following sections. For the sake of comparisons, we also fabricated hollow core waveguides (without corrugation) with the same core diameter and total length as that of the waveguide Bragg gratings. The prototypes of the waveguides shown in this paper were fabricated using a stereolithography 3D printer (*Asiga® Freeform PRO2*) with the photosensitive resin (*PlasCLEAR*). The printer has a resolution of 50µm along the x- and y-axes, and 1µm along the z-axis. Subsequently, the printed prototypes were cleaned and immersed into isopropanol solution for ~12hrs, and then fully coated with a silver layer using a wet chemistry coating method as detailed in [193].

The metallization process consisted of the following four steps. Firstly, the printed prototypes were cleaned by rinsing them with a nonionic detergent (Wetting Agent from *AngelGilding®*). This step was used to reduce the surface tension and allow water to flow freely over the prototype surface. Then, the cleaned prototypes underwent the surface sensitization with a stannous chloride ($SnCl_2$) aqueous solution. In this step, the prototype surface was coated with a thin film of stannous ions (Sn^{2+}) in order to improve the uniformity of the Ag coating. After sensitization, the prototypes were immersed into the prepared Ag coating solution, which was a mixture of a home-made Tollens' reagent and a glucose aqueous solution. During the coating process, continuous magnetic stirring was applied for the uniform reaction between the prototype and the reagent. Finally, after being cleaned by rinsing into deionized water, the metallized

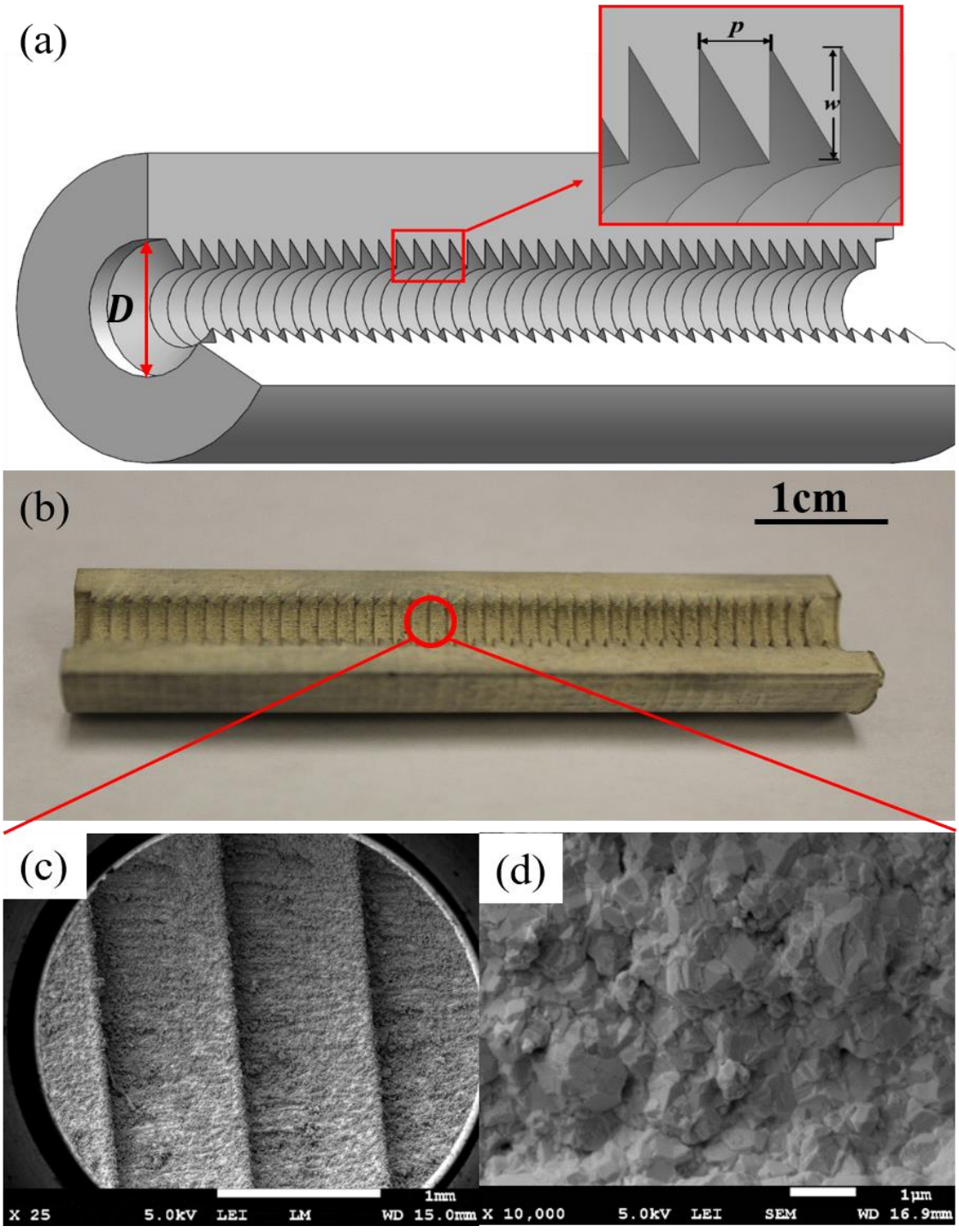

Figure 6.2 (a) The 3D geometry of the waveguide Bragg grating. Insert: zoom of the periodic structures. (b) Cut through of the fabricated waveguide Bragg grating. (c) and (d) SEM images for the area highlighted by the red circle in (b) with magnifications of ×25 and ×10000, respectively.

prototypes were desiccated by placing them in a fume hood at a room temperature for ~12hrs. The experimental procedures and solutions that we used are summarized in Table 4.

The fabricated waveguide Bragg grating is printed in Figure. 2(b) (only one half of the dissected waveguide is shown). The surface of the periodic corrugations was imaged using a scanning electron microscope (SEM). As shown in the SEM images [Figure 6.2(c) and (d)], the wet chemistry coating produces a uniform deposition of silver particles on the waveguide surface. The grain size of the silver particles varies from hundreds of nanometers to several micrometers. Resulting silver layer has thickness which is much larger than the skin depth for the THz waves ($\leq 100\text{nm}$) which prevents it from leaking into the dielectric cladding. Moreover, the roughness of the coated silver layer is $\sim 1\mu\text{m}$, which is three orders of magnitude smaller than the THz wavelength used in the experiments ($\sim 1\text{mm}$), thus resulting in very small scattering loss as we have confirmed by comparing transmission through Ag-coated waveguides and polished copper tubes.

We also characterized the electric quality of the coated silver layer. Firstly, the resistance of the coated silver layer was measured directly by placing the probes of a digital electric multimeter at the two ends of the waveguide inner surface. For both the waveguide Bragg grating and hollow core waveguide (tubes), the measured resistances were less than 6Ω, which indicates that the coated silver layers are continuous and the fabricated waveguides are fully metallized.

Table 4. The experimental producers and solutions used in the waveguide metallization

Item	**Composition of each solution**
Pre-cleaning	Nonionic detergent: 10mL Wetting Agent from *AngelGilding*® in 90mL deionized water
Sensitization	Sensitization solution: 3mL Tin for Silver Concentrate from *AngelGilding*® in 90mL deionized water
Coating	Tollens' reagent: 1.2g $AgNO_3$ and 2.4g NaOH in 90mL ammonium solution (NH_4OH; 28%-32%); Glucose aqueous solution: 0.8g glucose ($C_6H_{12}O_6$) in 300mL deionized water;
Post-treatment	Cleaning with deionized water; Desiccating in a fume hood at room temperature (21°C).

6.3 Numerical Modeling

Light guidance in the proposed waveguide Bragg gratings was first analyzed numerically using COMSOL finite element software. The computation cell was that of the unit cell of the periodic structure, which was terminated in transverse direction by a perfect electric conducting boundary to simulate the metal-air interface. In the longitudinal direction, Bloch-Floquet boundary condition was used. The computed band diagram is shown in Figure 6.3. The color code for the modes in the band diagram indicates the absolute value of the modal coupling coefficient by filed from the 3D Gaussian beam into a given mode. The coupling coefficient by field is defined using the continuity of the electric field components across the coupling interface between the incident Gaussian beam and the guided modes [157]:

$$C_m = \frac{\iint (\boldsymbol{E_m^*} \times \boldsymbol{H_{in}} + \boldsymbol{E_{in}} \times \boldsymbol{H_m^*}) drdz}{2\sqrt{\iint \mathrm{Re}(\boldsymbol{E_m^*} \times \boldsymbol{H_m}) drdz} \times \sqrt{\iint \mathrm{Re}(\boldsymbol{E_{in}^*} \times \boldsymbol{H_{in}}) drdz}} \tag{6.2}$$

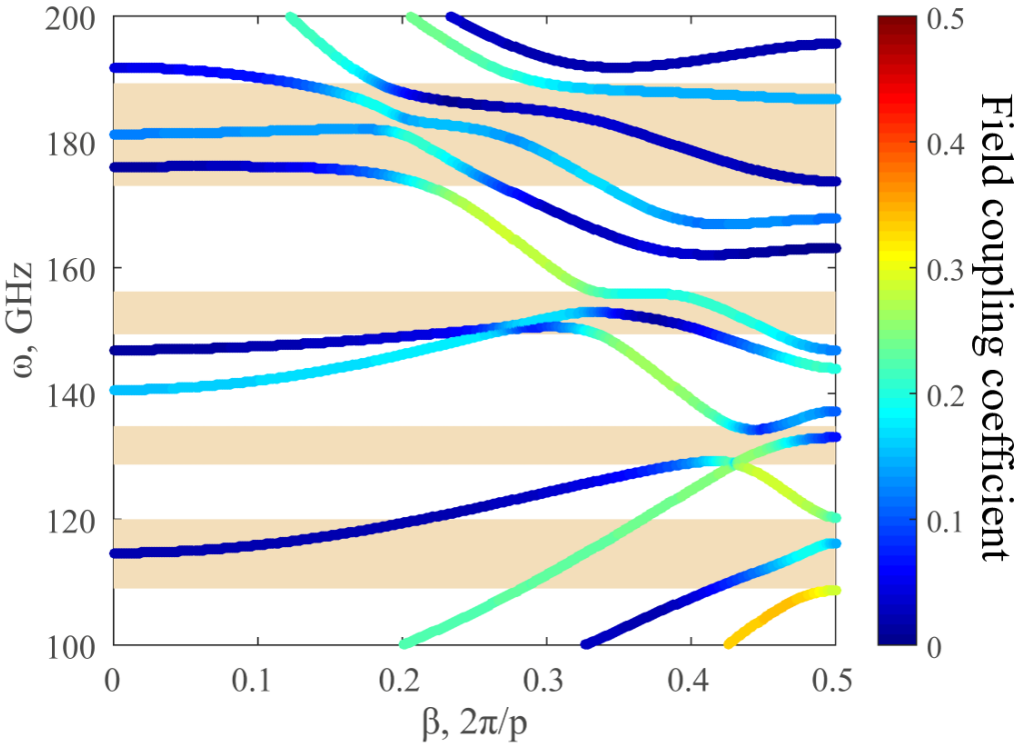

Figure 6.3 Band diagram of the waveguide Bragg grating. Color refers to the modal coupling coefficient (by field) to the focused Gaussian beam of $w_0 \sim 2\lambda$.

where integration is performed over the whole unit cell, and the corresponding power coupling coefficient is $|C_m|^2$. For input beam, we assume a linearly polarized 3D Gaussian beam with the polarization normal to the beam propagation direction. Electric field of such a beam is given by [194]:

$$\boldsymbol{E_{in}}(r,z,t) = \overrightarrow{n_r}\frac{w_0}{w(z)} \cdot \exp[-\frac{r^2}{w^2(z)}] \cdot \exp[-i\frac{k \cdot r^2}{2R(z)}] \cdot \exp\{-i[kz - \phi(z)]\} \cdot \exp[i\omega t] \quad (6.3)$$

where w_0 is the beam waist radius and assumed to be $\sim 2\lambda$, $w(z)$ is the spot size, $R(z)$ is the beam curvature radius, and $\phi(z)$ is the Guoy phase shift at distance z from the focal point. Magnetic field of the external Gaussian beam can be calculated from Eq. 3 using one of the Maxwell equations, $B_{in} = \frac{c}{\omega}\nabla \times E_{in}$. For simplicity, we only present modes with coupling coefficients bigger than 0.01. Thus, in Figure 6.3, modal dispersion relations of guided modes with angular momentum equal to 1 ($m = 1$) are presented, while the other modes would not be excited by a centrally coupled, linearly polarized terahertz source due to the symmetry mismatch.

As shown in Figure 6.3 in the 100-200 GHz range, there are several bandgaps of the fundamental HE_{11}-like mode and higher order modes opened by the Bragg grating. Particularly, we are interested in operation within bandgaps of the higher order modes, where waveguides can be considered effectively single mode with maximal coupling coefficient to HE_{11} mode. From Fig. 3, we observe that there are two such spectral regions, one is in the vicinity of 140 GHz [see Fig. 4(a)], while another one is in the vicinity of 160 GHz [see Figure 6.4(c)]. There, dispersion relation in yellow-green corresponds to an HE_{11}-like mode that can be efficiently excited using focused Gaussian beam. In Figure 6.4 (b) and (d), we show corresponding modal group velocity dispersions defined as:

$$D = \frac{\partial^2 \beta}{\partial \omega^2}\,[\mathrm{ps/(THz \cdot cm)}] \quad (6.4)$$

where β is the wave number and ω is the angular frequency. The magnitude of dispersion increases dramatically in the vicinity of the bandgap edges and frequencies of avoiding crossing with the 'plasmonic' modes. Both positive and negative dispersions are possible in our device.

In the spectral ranges of single mode guidance of the fundamental mode (HE_{11}) in the vicinity of 140GHz and 160GHz, mode dispersions are negative and varies strongly. Thus, in a

single mode frequency range of 137-141GHz, as shown by the gray region in Figure 6.4 (a), the dispersion varies between -330 and -130 [ps/(THz · cm)]. For frequencies within this region, all higher order modes are eliminated due to bandgap effects, and only the fundamental HE_{11}-like mode remains. In principle, outside of this region and within $\sim 133 - 144$ GHz, there is only one other mode that is present and coupling coefficient to this mode is an order of magnitude smaller than that to an HE_{11}-like mode. Thus, even outside of the single mode regime, one can still expect quasi-single mode guidance. At these frequencies, however, modal dispersion value can change dramatically and even change sign. Therefore, the problem of increasing the operational bandwidth, while keeping dispersion relation value constant still deserves further study. Similarly, in the vicinity of 160 GHz, the single mode guidance is strictly realized over 156-162GHz, and can

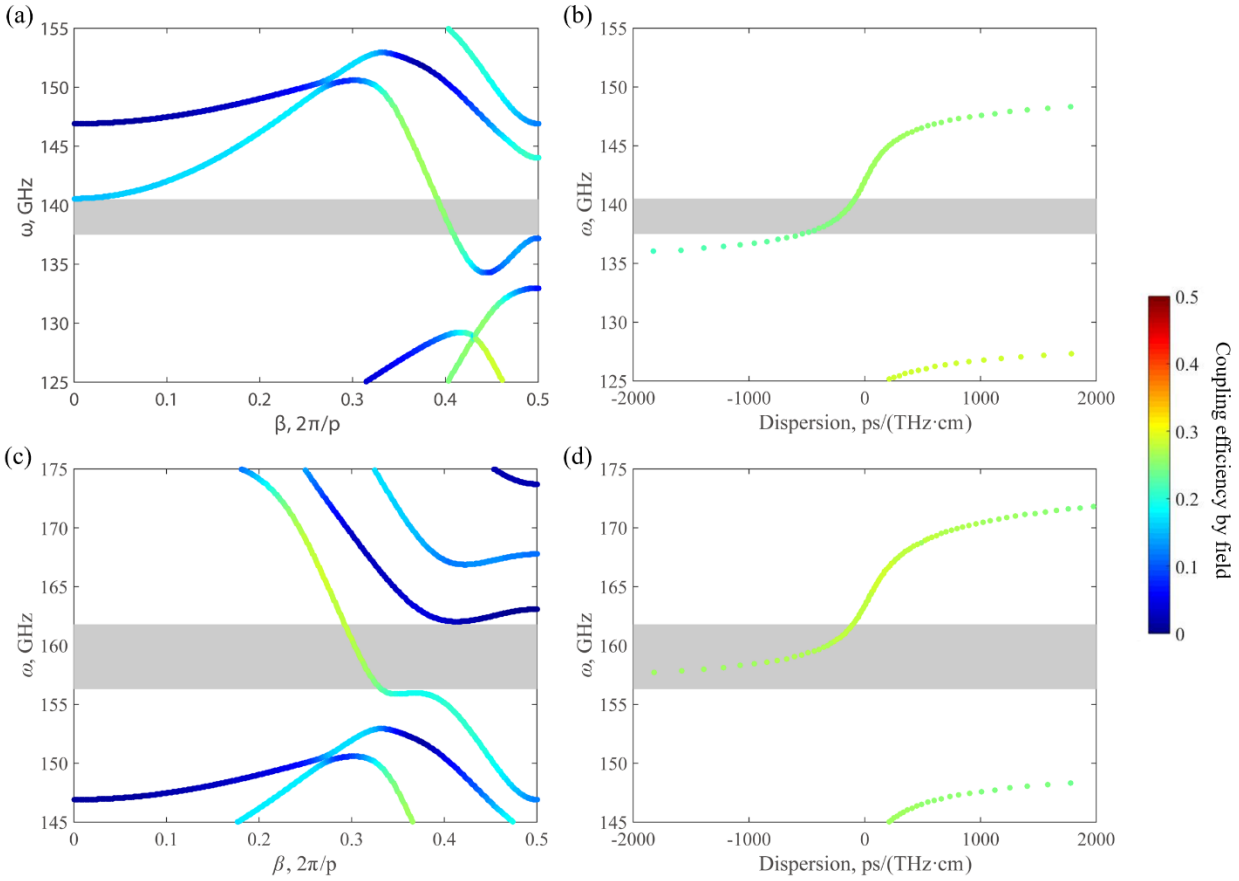

Figure 6.4 (a) Dispersion relations of the guided modes and (b) calculated dispersion relation of the fundamental HE_{11}-like mode in the vicinity of 140 GHz, while (c) and (d) are that in the vicinity of 160 GHz. The gray regions refer to the single mode regime where only the fundamental HE_{11}-like mode is excited. Color of dots is the same as that shown in Figure 6.3.

be extended to the frequency range of 156-167GHz due to the low coupling coefficient to higher order modes in this range, see Figure 4(c).

6.4 Optical Characterization

6.4.2 Transmission Characterization

The characterizations of the fabricated waveguides were carried out using continuous wave Terahertz (CW-THz) spectroscopy system (*Toptica* Photonics), as schematically shown in Figure 6.5. The setup has two distributed feedback (DFB) lasers with slightly different center wavelengths and uniform power (~30mW each) operating in the telecom region. A 50:50 coupler combines and splits the two wavelengths equally into the emitter and detector arms respectively. Two single mode polarization maintaining fibers wounded around piezo actuators that stretch in the opposite directions are connected to both the arms for the phase measurement [160]. The symmetric arrangement of the fiber stretchers provides additional path delay as well as phase noise cancelation that can be caused by the variation in the environment. The path lengths between the emitter and detector arms are balanced (in the empty configuration) to have a flat phase, which is almost frequency independent. The THz waves are generated by the emitter photomixer which emits the frequency difference between the two lasers which are furthermore modulated using the bias voltage for lock-in detection. By tuning the lasing wavelengths, such a system can generate a tunable THz radiation between 50 GHz - 1.2 THz, with bandwidth as narrow as 40MHz. The THz beams were focused and collected from the waveguides using the gold coated reflective optics (flat and parabolic mirrors. Additionally, two metallic apertures were placed at the input and output facets of the waveguide in order to block any stray light and avoid coupling into plastic cladding. The measurements were obtained for the frequency range 100 - 200GHz with 100MHz frequency resolution and 600ms integration time constant. The generated photocurrent in the detector was recorded along with the phase information as a function of frequency.

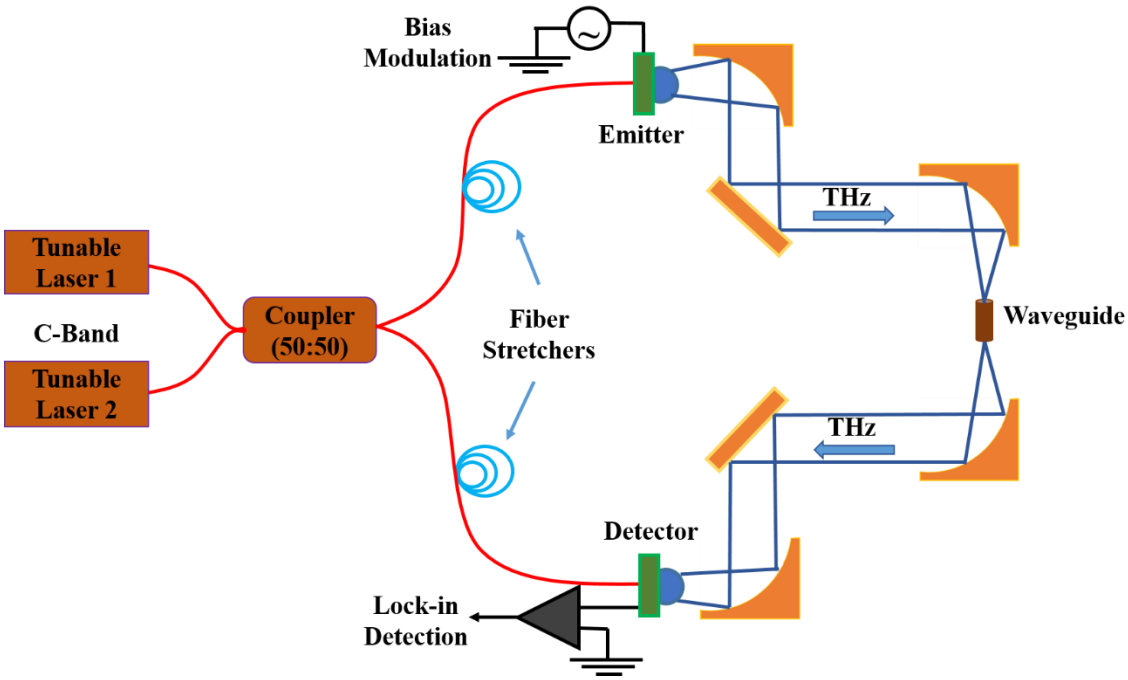

Figure 6.5 Schematic of the experimental setup for optical characterization.

The measured THz electric fields and corresponding transmission spectra are shown in Figure 6.6 (a) and (b), respectively. The reference shown here was acquired by removing the test waveguide, while displacing parabolic mirrors to share the same focal point as the second situationally parabolic mirror. Additionally, at the focal point, we used an aperture whose opening is similar to the core size of the measured waveguide. The measured reference photocurrent in the frequency range of 120-140GHz, shows the prominent standing wave with beat frequency of 4GHz. These standing wave is due to the Fabry–Pérot interference within the silicon lenses of the photomixers. The complex transmission of these waveguides can be computed as

$$T(\omega) = \frac{E_t}{E_r} = t(\omega) \cdot \exp[i\varphi(\omega)] \tag{6.5}$$

where E_t and E_r are the complex electric fields measured with and without the tested waveguide, $t(\omega)$ is the absolute transmission spectrum, and $\varphi(\omega)$ is the measured phase.

Firstly, we characterized the performance of the metal-coated 3D printed plastic tubes by comparing their transmission spectra to those of the commercial copper tubes with the same core size and length. As seen in Figure 6.6 (b), these two waveguides show almost the same transmission

properties in the frequency range of 100-200GHz. From this, we conclude that our metallization recipe was chosen correctly.

Next, we characterize transmission through the waveguide Bragg grating. In the frequency range of 100-200GHz, there are four low transmission windows with center frequencies of 118GHz, 135GHz, 153GHz, and 187GHz that have transmission losses in excess of 15dB. These regions coincide well with the theoretically predicted regions of week excitation of the HE_{11}-like mode shown as orange bands in Figure 6.3 (a). while outside the bandgap, the transmission losses are about 5dB, as shown in Fig. 6(b). We stress again that low transmission regions are not due to high propagation loss of a waveguide, but due to low coupling of the probing Gaussian beam to the waveguide modes.

Finally, we compare theoretical predictions with experimental measurements of the modal group velocity dispersion [see Figure 6.7 (b)]. As shown in the theoretically simulated band diagram [see Figure 6.3 (a)], in the high transmission regions [clear regions in Figure 6.3 (a)], there is always one mode that features a much higher value of the coupling coefficient to the Gaussian beam comparing to other modes. Dispersion of such a mode is shown in orange-red colors. Thus, in the high transmission regions, the output electric field corresponds to that of a mode with highest coupling efficiency:

$$\begin{aligned} \boldsymbol{E}_{output}(\omega) &= C_m \cdot \exp[i\varphi_m] \\ \varphi_m &= L \cdot \left(\beta_m(\omega) - \frac{\omega}{c}\right) \end{aligned} \tag{6.6}$$

where C_m, φ_m and β_m are the calculated coupling efficiency, phase and propagation constant of that mode, and L is the waveguide length. Using this assumption, we calculate the phase of the output electric field, as shown by the black solid line in Figure 6.7 (a). For frequencies within high transmission regions, the theoretical and experimental results show good agreements. We note that the measured phase in Figure 6.7 (a) is with respect to the reference, and therefore $\varphi_m = L \cdot (\beta_m(\omega) - \omega/c)$. Next, in Figure 6.7 (b), we present comparison of the experimentally measured and theoretically predicted group velocity dispersions. Experimentally measured GVD is computed from the phase data as $\partial^2(\varphi/L)/\partial\omega^2$, where φ is the measured phase and L is the waveguide length. Before computing second order derivative, a spline interpolation is used on the experimental data in order to alleviate the noise contribution. Theoretical dispersion is computed using the dispersion relation of the mode with the highest coupling coefficient to the excitation

Gaussian beam shown in Figure 6.3 (a). The results show good match. Finally, in the strict single mode regions, both theoretical and experimental results confirm the strongly negative dispersions. In the 137-141GHz range, dispersion varies from -500 to -100 ps/(THz·cm). At the same time, in the 156-162GHz range, dispersion varies from -2000 to -60 ps/(THz·cm).

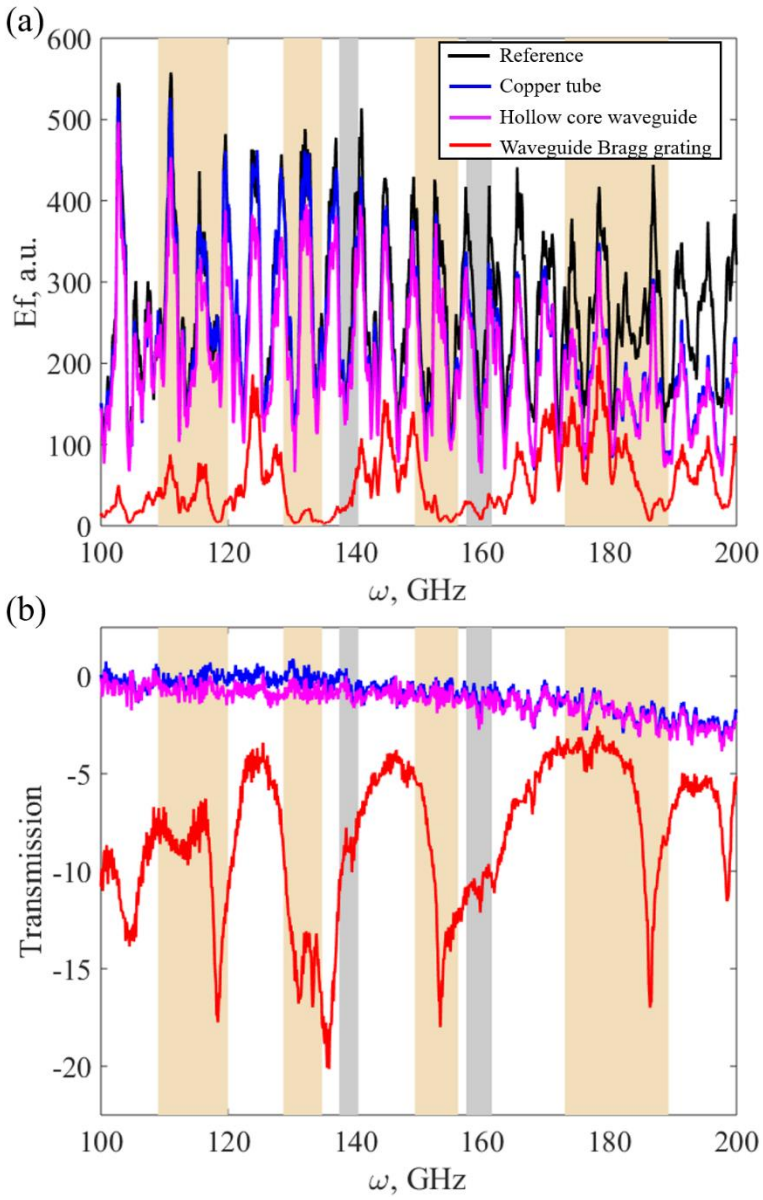

Figure 6.6 (a) Measured electric fields and (b) corresponding transmission spectra of fabricated waveguides.

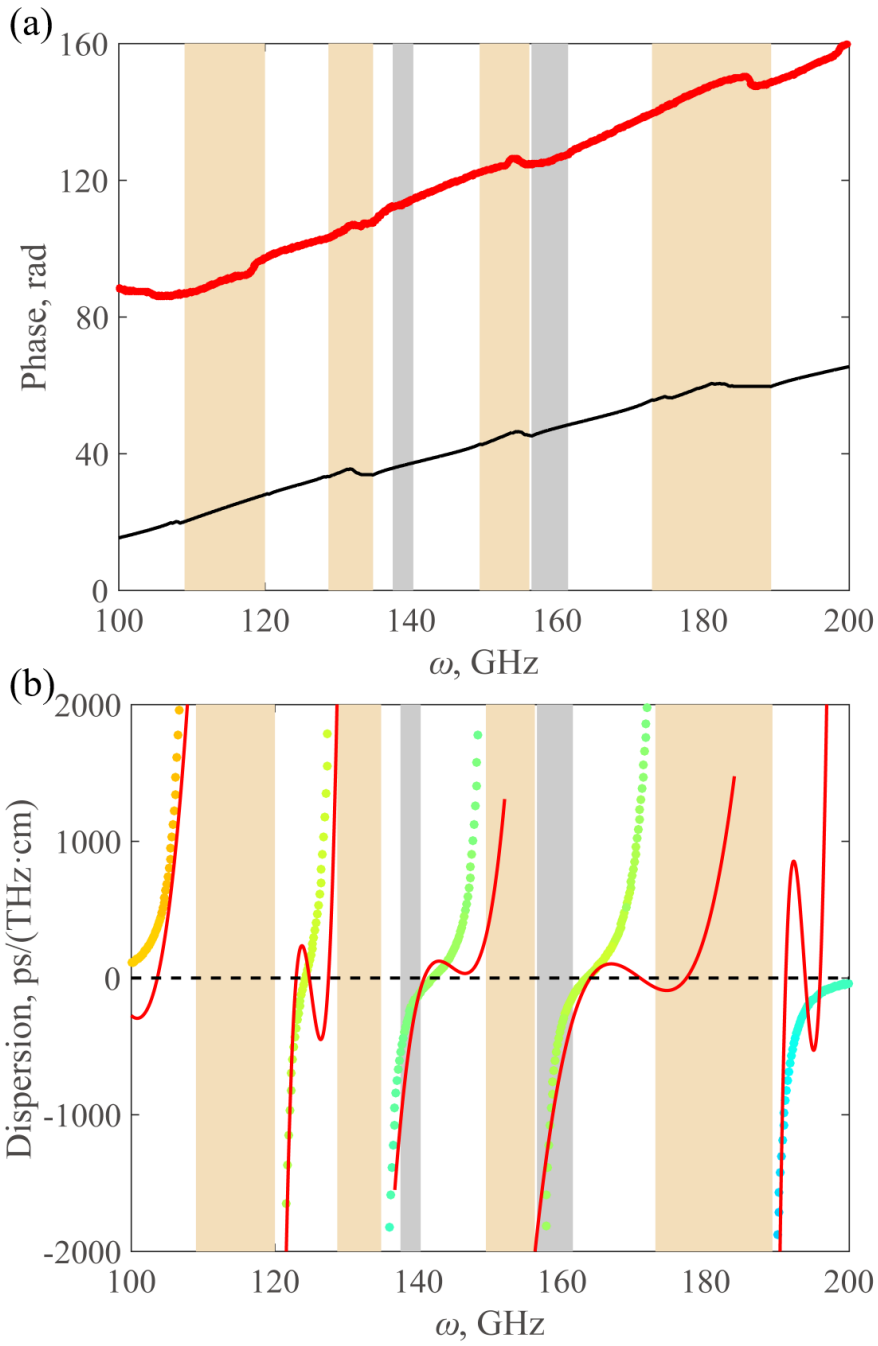

Figure 6.7 (a) Comparison between the experimentally measured phase (red dots) and the theoretically computed phase (black solid line). Region with different colors refer to the frequency regions mention in Figure 6.3 and 6.4. The blue circle highlights errors caused the negligible transmission within the stopbands. (b) The comparison between the experimentally measured dispersion (red solid lines) and the theoretically computed dispersion of the fundamental mode (HE_{11}). The color code of dots is the same as that shown in Figure 6.3.

6.4.2 Near Field Imaging of The Waveguide Output

Next, we investigate the single mode operation of our waveguide Bragg grating. As shown in Figure 6.4, within spectral ranges in the vicinities of 140GHz, only the fundamental HE_{11}-like mode is excited by the external Gaussian beam. Hence, we expect Gaussian-like modal distribution at the waveguide output end in these spectral ranges. To confirm this assumption, we map the near-field distribution of the *x* component of the electric field (E_x). Near field images of the output field profiles was obtained using a terahertz time-domain spectroscopy (THz-TDS) based near field imaging system. The schematic of this imaging system is shown in Figure 6.8. Here, an interdigitated antenna array is used for emitting a parallel THz beam, and then the THz beam is converged into the tested waveguide by a Teflon lens. The detector antenna, sheltered by a metallic pinhole of 1mm diameter, is mounted on a 3D stage and coupled with a polarization maintaining fiber by using an optical lens. The gap between the pinhole and the waveguide output facet is about 0.5mm, which is much smaller than the wavelength at 140GHz ($\sim$2mm). With a scaning range of 9×9mm and step size of 0.25mm, the scanning provides a modal pattern with 37×37 pixels at each frequency.

In the top row of Figure 6.9, we present normalized electric field profiles ($|\boldsymbol{E}|$) at selected frequencies as measured experimentally. For the comparison, in the blow row of Figure 6.9, we correspondingly present theoretical electric profiles at same frequencies numerically computed by using the finite element software COMSOL. The waveguide core region with diameter of $D = 9.0$mm is highlighted by blacksolid circles, while the central region without periodic structures with diameter of $d = D - 2h = 5.2$mm is highlighted by black dashed circles. The near field images show good agreements with the theoretical prediction. In the vicinity of 140GHz, both the experimental imaging and the theoretical prediction show Gaussian-like electric profiles in the central core region without periodical structures, which confirm the single mode operation in this frequency range. Meanwhile, outside the single mode operation spectral range, the results show the hybridization of the fundamental HE_{11}-like mode and higher order modes, as the modal profiles are not Gaussian-like any more [see the first and third columns in Figure 6.9].

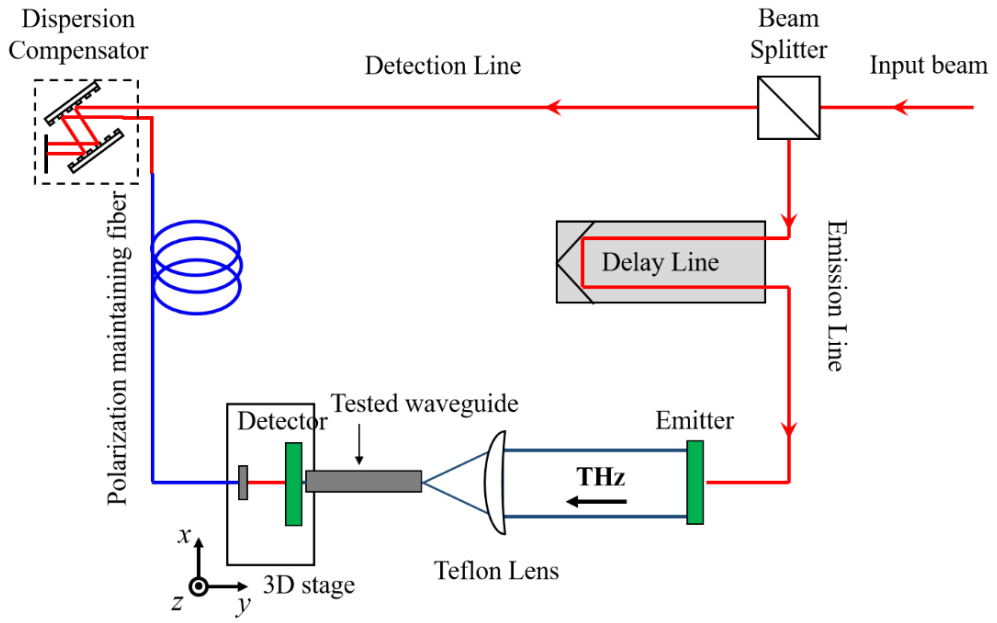

Figure 6.8 Schematic of the setup used for near field imaging.

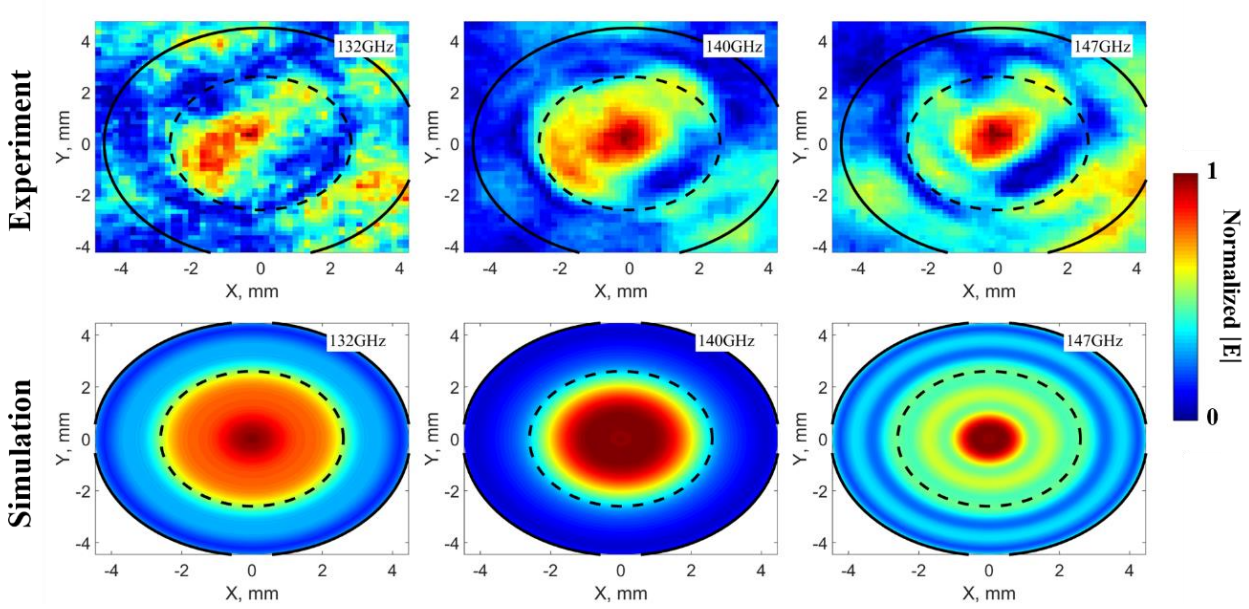

Figure 6.9 Near-field microscopy images (upper row) and corresponding simulations (lower row) of the normalized output $|\boldsymbol{E}|$ field profile of the waveguide Bragg grating for frequencies in the vicinity of 140GHz. The black solid circle refers to the waveguide core edge, while the dashed circle shows the region of the central area of the waveguide core without periodic structures.

6.5 Summary of waveguide Bragg grating results

Hollow core waveguide Bragg grating featuring periodically placed triangular axisymmetric slopes on its inner surface is proposed as a dispersion compensator in the terahertz frequency range. The waveguide structure is designed and optimized for the dispersion compensation in the vicinity of 140GHz, which requires single mode guidance for the HE_{11}-like mode, large negative dispersion, and efficient coupling to the external Gaussian THz beam of waist diameter $\sim 2\lambda$. Theoretical results show that the optimized waveguide Bragg grating supports a single mode operation over the 137-141GHz spectral range, while in the somewhat broader frequency range coupling coefficients to higher order modes are still very low (<20% by field). Within the single mode guiding range, the dispersion of the fundamental HE_{11}-like mode has large negative values. Specifically, the dispersion of the fundamental HE_{11}-like mode is $\sim -130\text{ps}/(\text{THz}\cdot\text{cm})$ at 140GHz, while varying in the $-500 \sim -100\ \text{ps}/(\text{THz}\cdot\text{cm})$ range over 137-141 GHz. In the vicinity of 160GHz, we also obtain a single mode range over the spectral range of 156-162GHz, where the dispersion of the fundamental HE_{11}-mode varies from $-1500\text{ps}/(\text{THz}\cdot\text{cm})$ to $-60\text{ps}/(\text{THz}\cdot\text{cm})$.

Using numerically optimized waveguide structure, we fabricated the prototype of the waveguide Bragg grating using a 3D stereolithography system, and subsequently metallized it using with silver layer using wet chemistry. Then, we have characterized the property of the coated silver layer using various physical and optical approaches, including measuring the resistance of the waveguide inner surface, SEM imaging, as well as comparative analysis of the Ag coated plastic tubes and commercial copper tubes. All these results confirmed that our waveguide was successfully metallized, and resulted optical properties of coated metallic layers were comparable to these of bulk metals. The optical properties of the fabricated waveguide Bragg grating were then measured experimentally using a terahertz continuous wave spectroscopy. Experimental findings reproduced well the theoretically predicted modal properties, including spectral positions of high transmission regions and modal dispersion within these regions. From this, we conclude that presented device shows single mode operation, relatively high coupling efficiency, and strong negative dispersion, which is at least one order of magnitude higher than these of typical THz waveguides. This makes the proposed device suitable for dispersion compensation in free-space and fiber links for terahertz communications.

CHAPTER 7 GENERAL DISCUSSION

In this chapter, I would like to discuss some of the important considerations regarding previous sections. First, I will highlight the limitations of the waveguide fabrication techniques used in this thesis. Then, I will present our attempts at fabricating metallic waveguides using the 3D printer. To conclude, I will discuss the characteristics of the THz systems used to obtain the results presented in this thesis, including their signal to noise ratio, dynamic range, and beam waist size.

7.1 Waveguide fabrication limitations

The THz waveguides mentioned in this thesis were fabricated using two different techniques: thermal drawing and 3D printing. While using these two techniques, the performance of the fabricated waveguides was mainly limited by two factors which were fabrication imperfections and the choice of materials.

During the thermal drawing method, the fiber preforms were first fabricated using a computer numerically controlled (CNC) machine. We had a limited choice of hole sizes as being limited by the diameter of available drill bits. It is impossible for us to obtain air-hole arrays using arbitrary hole sizes. Moreover, the fiber geometry was further affected as the air-holes would collapse during the drawing process. However, this problem can partially be solved by applying air pressure to the air-holes. Although the application of air pressure can prevent air-holes from completely collapsing, it cannot guarantee a uniform cross-section for a fiber with a long length, as the air-holes would still end up either shrunk or inflated. Another factor which limits the performance of the waveguide is the choice of materials suitable for thermal drawing. For the graded index microstructured THz fiber, I chose low density polyethylene (LDPE) as it is cheap and easily used for fabrication (drilling and drawing). However, its applications are limited by its moderate absorption in the terahertz range which is quite high when compared to its more specialized counterparts (such as Topas, Zeonex, etc.).

For the 3D printing method, the accuracy with which we could reproduce the simulated design of a waveguide was limited by multiple factors, including the printer specifications, the printing materials, and the complexity of waveguide geometry. For example, with the hollow core photonic bandgap waveguide with hyperuniform reflectors, to maximize the bandgap width in the

vicinity ot 0.4THz, the bridge thickness of the hyperuniform reflector was optimized to be ~35μm. Although the printer we used (*ProJet® 3500HD Plus*) offers a resolution of ~32μm in both *x*- and *y*-directions, to print a robust structure, the minimum bridge thickness we can obtain is about ~200μm.

For the 3D printed waveguide, the available materials are further limited to polymers which are sensitive to UV lights. These photosensitive polymers are also known as "photoresins". Typically, we would choose a transparent photoresin recommended by the printer manufacturer. However, after being cured by UV light, these photoresins are highly absorptive and unfriendly to post-printing treatments. As shown in Chapter 4, we characterized the optical properties of the reflector material (VisyJet® Crystal) used during waveguide fabrication. The measured material absorption is proportional to ω^2, where ω is the frequency in THz. At 1THz, the measured absorption is ~10.43cm^{-1}, which is even much bigger than that of LDPE.

7.2 3D printed metallic waveguides

It has recently been demonstrated that functional THz materials can be introduced into the 3D stereolithography printing process with a goal of printing functional terahertz devices. The proposed idea is to mix advanced materials, such as nanopowders of ceramics, piezoelectric ceramics, metals, *etc.*, with curable resins, and then use the resulting slush for 3D printing.

Here, I would like to show my attempts at fabricating metallic tubes with a slush of photoresin (*PlasClear*) and nanopoders of copper. The slush was prepared by mixing 10g of copper powder and 150mL of resin. The resulting concentration of the copper powder in the mixture was about 5.65 wt%. To disperse the copper powder into the resin, the mixture was mechanically stirred for 2 hours, and then sonicated by a sonicater at a power of 300W for a duration of 1 hour. During the whole dispersing procedure, the mixture was purged by nitrogen to prevent the copper powder from being oxidized. Meanwhile, the mixture was cooled down in a water bath to release the heat generated by sonication and to prevent the resin from aging. Afterwards, using a 3D printer (*Asiga® FreeForm Pro 2*), the mixture was used to produce hollow core waveguides with a core diameter of 1.67mm and differing lengths (4cm, 6cm, and 8cm). The whole printing process took about 16 hours. For the sake of comparison, I also prepared polymer tubes (using resin only) and commercial copper tubes with the same core size.

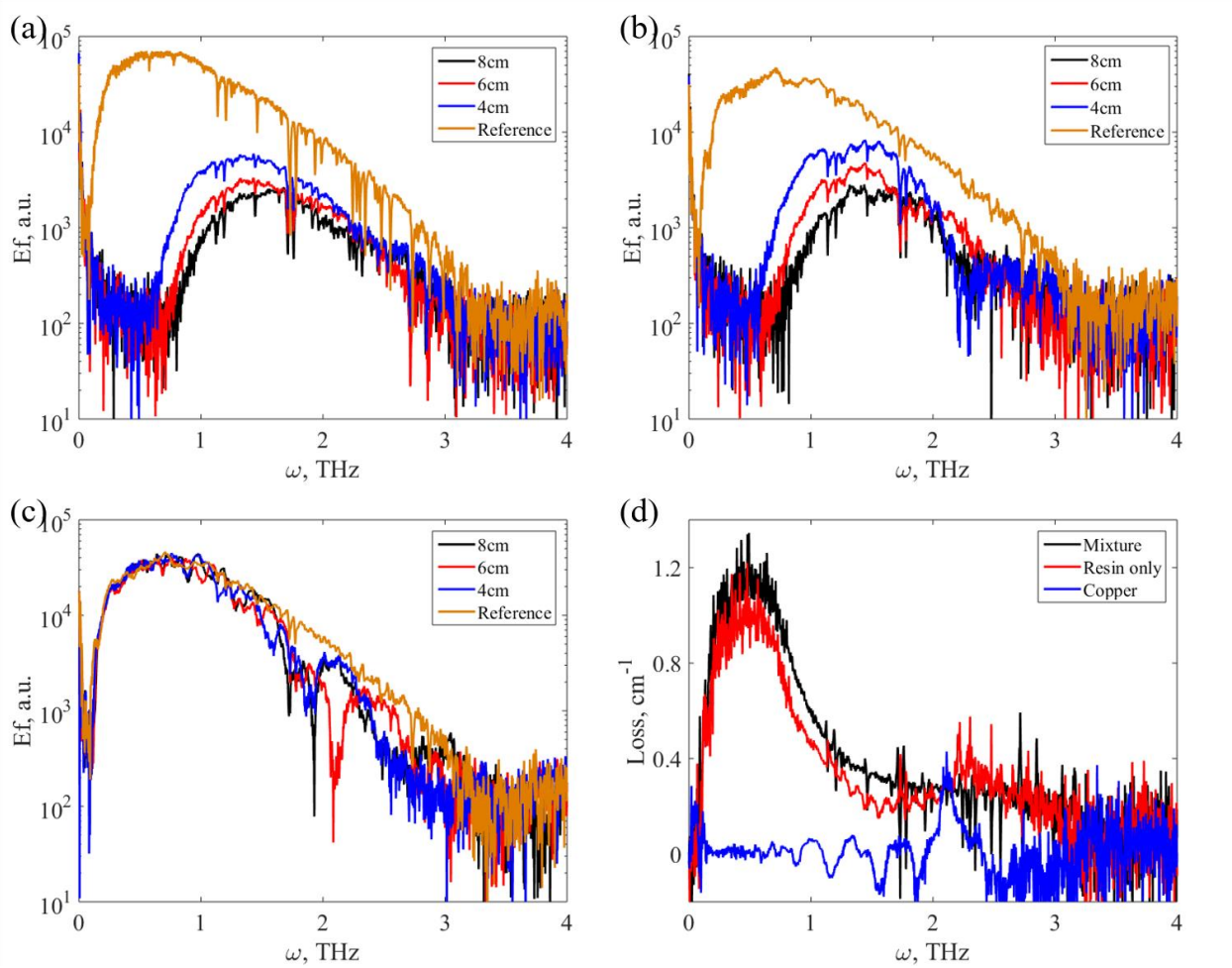

Figure 7.1 Measured frequency domain spectra of (a) hollow core waveguides printed by slush of copper powder and resin, (b) hollow core waveguide printed by resin only, and (c) commercial copper tubes. (d) the measured transmission losses of the measured waveguides.

The transmission properties of these waveguides were characterized using the THz-TDS system. In Figure 7.1, the experimental results show that the transmission of the hollow core waveguides fabricated from the resin and copper powder slush is almost the same as that of the resin-only alternative. Moreover, the losses of both waveguides are inversely proportional to ω^2. Contrarily, the transmission losses of the metal tube with the same core size are negligible when compared with that of the other two waveguides. These experimental results confirmed that the slush is still polymeric, not metallic.

Actually, we can use the Bruggeman formulation to compute the dielectric constant of the resin and copper powder slush [195]:

$$(1-c)\cdot\frac{\varepsilon_p-\varepsilon_{eff}}{\varepsilon_p+2\cdot\varepsilon_{eff}}+c\cdot\frac{\varepsilon_m-\varepsilon_{eff}}{\varepsilon_m+2\cdot\varepsilon_{eff}}=0 \quad (7.1)$$

where ε_{eff} is the dielectric constant of the mixture. ε_p and ε_m are the dielectric constants of the resin and copper powder, respectively. c is the volume concentration of the copper powder in the resin. In the mixture we used for 3D printing, $c = 0.74\%$. Consequently, the resulting dielectric constant of the mixture is very close to that of the resin.

7.3 THz systems characterization

7.3.1 Noise and uncertainties

All of the optical characterizations presented in this thesis were obtained through the use of terahertz time-domain and continuous wave terahertz spectroscopies. For both systems, both noise and uncertainties were significantly limiting factors during the optical characterization process, affecting both system resolution and sensitivity. In this section, I will compare the performance of the THz-TDS and CW-THz systems by analyzing their signal-to-noise ratio (SNR) and dynamic range (DR). SNR and DR define complementary aspects of system performance.

Both the THz-TDS and CW-THz systems measure the amplitude. The SNR and DR of such systems can be defined as [196]

$$\mathrm{SNR}=\frac{\text{mean magnitude of amplitude}}{\text{standard deviation of of amplitude}} \quad (7.1)$$

$$\mathrm{DR}=\frac{\text{maximum magnitude of amplitude}}{\text{mean of noise floor}} \quad (7.2)$$

In this definition, SNR represents the accuracy of the measured amplitude, while DR defines the system response to weak signals. For a THz-TDS system, SNR and DR can be evaluated by examining both the time-domain electric trace and the corresponding frequency dependent spectrum which is calculated using the Fourier transform.

Figure 7.3(a) gives examples of a typical time domain electric trace (red line), which is the average of 25 scans with an integrating time constant of 10ms and the scanning step of 67fs, together with its standard deviation (SD, blue line). While in Figure 7.1(b), I present the SNR analysis of the corresponding frequency domain spectrum. The standard deviation varies with the

temporal position, leading to poor accuracy of the SNR analysis. In order to provide a better evaluation of the SNR for the sake of our optical characterization, I used the peak value of both the time domain traces and the frequency domain spectra, as shown by the dashed lines in Figure 7.1. Using this method, I estimated that the SNR of this typical time-domain trace and its frequency domain spectrum are ~182 and ~110, respectively.

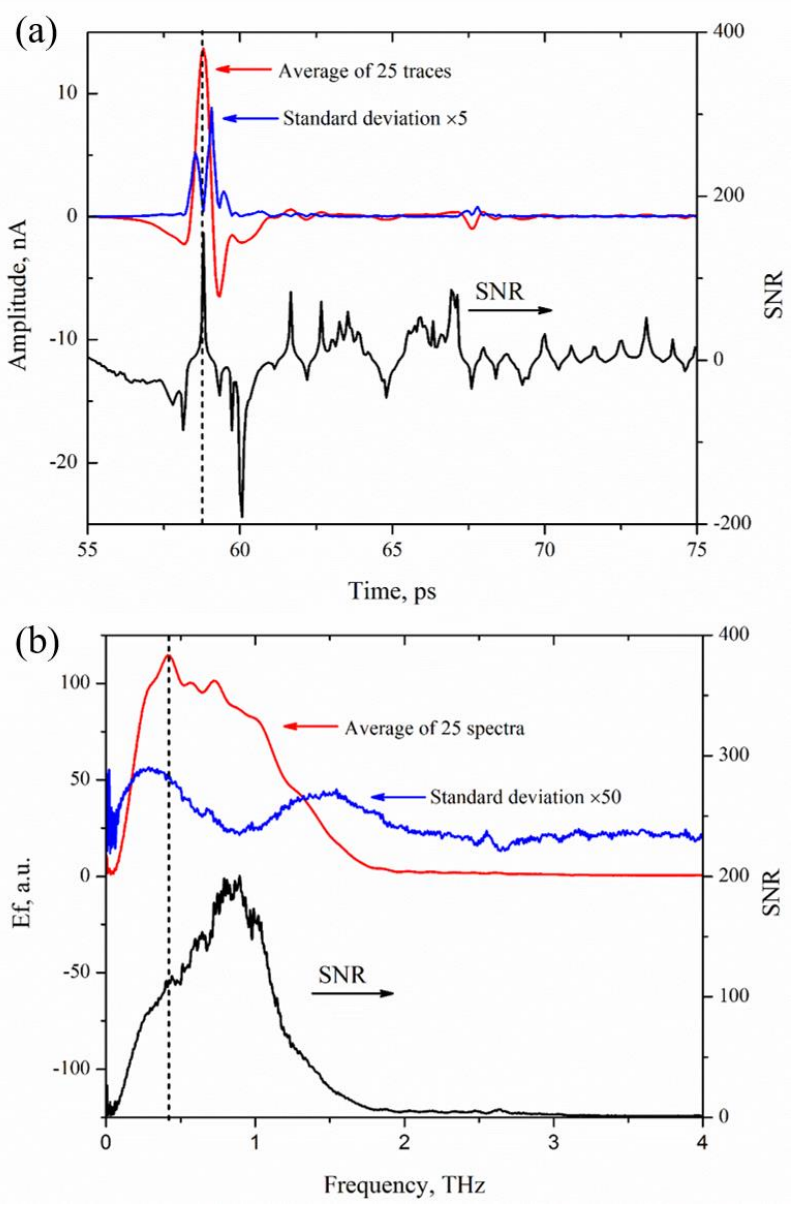

Figure 7.2 SNR analysis of (a) a typical time-domain trace and (b) corresponding frequency domain spectrum. Left ordinate: average of 25 scans (red) and their standard deviation (blue). Red ordinate: calculated SNR as the ratio of the average value to the SD.

Table 5 SNR values of the measurements with different integrated time constant

Time constant	1ms	10ms	100ms
Time domain	153	182	230
Frequency domain	67	110	154

Table 6 DR values of the measurements with different integrated time constant

Time constant	1ms	10ms	100ms
Time domain	4136	4880	4353
Frequency domain	69	211	931

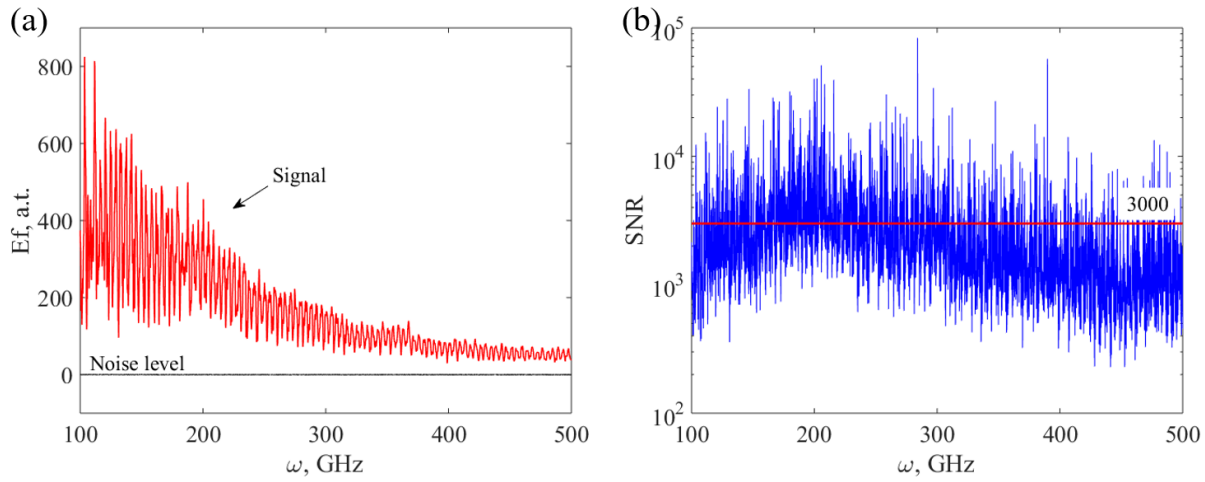

Figure 7.3 (a) Examples of the signal and background noise measured by the CW-THz system with an integrated time constant of 100ms. (b) the computed signal to noise ratio.

In our THz-TDS system, we are using a lock-in amplifier to detect the signal. Both the SNR and DR are dependent on the integrating time constant used in the measurement. In Table 5 and 6, I summarize and compare the SNR and DR of the measurements with different integrating time constants. The results show that with a larger integrating time constant, optical characterizations using the THz-TDS system can be improved as both SNR and DR are enlarged.

In our THz-TDS system, we are using a lock-in amplifier for detecting the signal. Hence, both SNR and DR are dependent on the integrating time constant used in the measurement. In Table 7.1 and 7.2, I summarize and compare SNR and DR of the measurements with different integrating time constants. The results show that with a larger integrating time constant, optical characterizations using the THz-TDS can be improved as both SNR and DR are enlarged.

In the case of the CW THz system, the signal to noise ratio is much larger as its signal is much stronger than that of the THz-TDS system. In Figure 7.4(a), I present a sample of the signal (red line) and background noise (black line), which are measured with an integrated time constant of 100ms. The background noise is measured by blocking the whole THz beam with a non-transparent foil. Its signal to noise ratio, which is computed directly by the ratio of amplitudes of the measured signal and noise, can be larger than 103 and with an average value of 3000 in the frequency range of 100-500GHz, which is 10 times bigger than that of the THz-TDS system.

7.3.2 Beam waist size

The coupling efficiency of guided modes plays a crucial role in the design of waveguide geometry and, consequently, the numerical simulation of its optical properties. This is especially true for waveguides with large core sizes, such as the hollow core photonic bandgap waveguide and waveguide Bragg grating shown in this thesis. The coupling efficiency can be used to identify the fundamental/dominant mode, which occupies the majority of guided power, and theoretically predict the optical properties of the proposed waveguides.

In this thesis, the modal coupling efficiency of a given mode is computed from the overlap integral of the respective flux distribution of this mode with that of the external Gaussian beam used as a source. Hence, the waist size (w_0) of THz Gaussian beams are crucial for coupling efficiency. In both the THz-TDS and CW-THz systems, THz beams are converged by a parabolic mirror and focused to the waveguide input facet. At the focal point of the parabolic mirror, the beam waist size of the Gaussian beam can be approximated by [192]

$$w_0 = \frac{4f\lambda}{\pi D} \tag{7.1}$$

where λ is the waveguide of the THz Gaussian beam, f and D are the focal length and aperture size of the parabolic mirror.

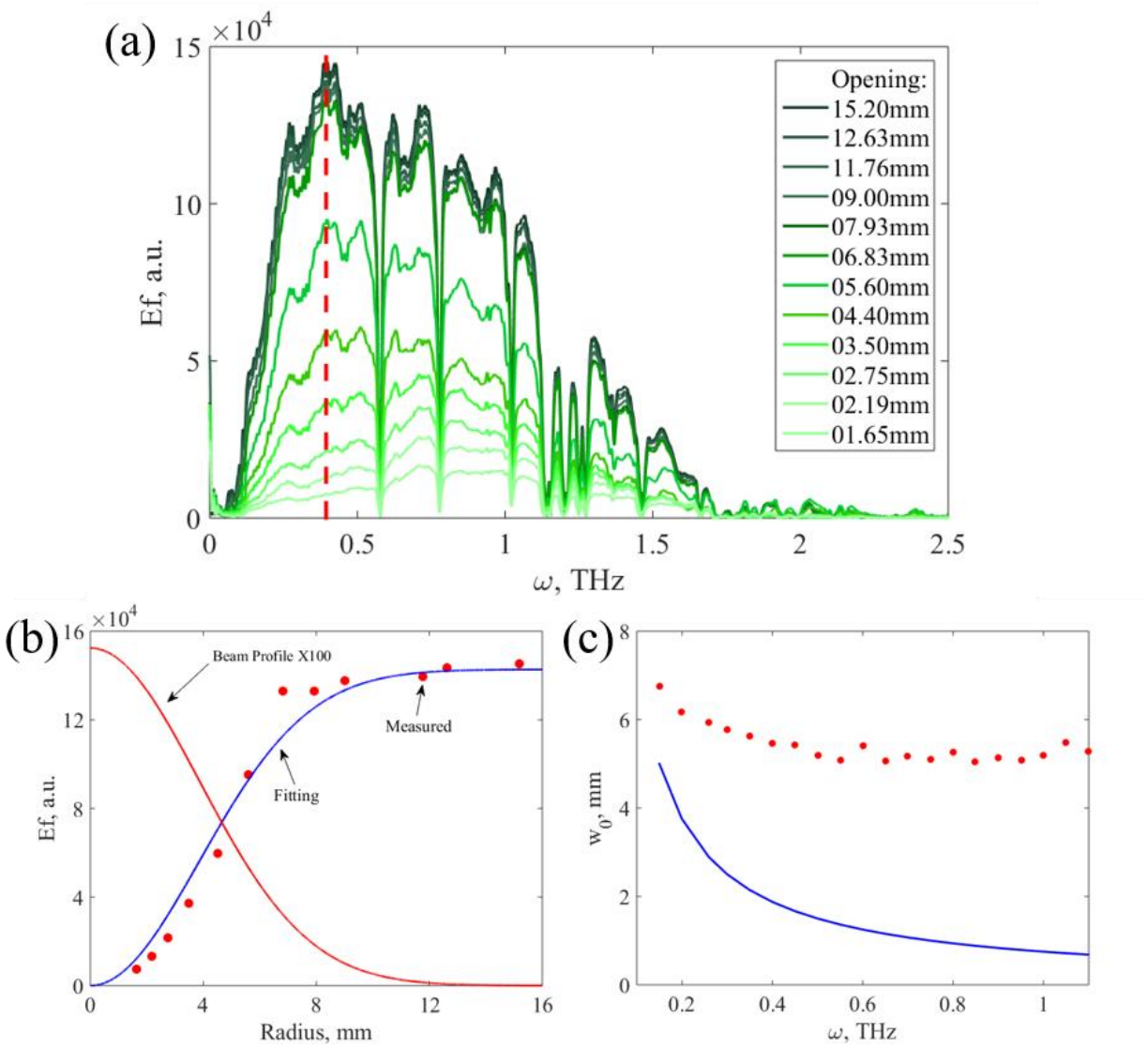

Figure 7.4 (a) The terahertz field amplitude as a function of frequency measured with different aperture opening sizes. (c) The measured THz electric field profile as a function of the aperture opening size (red dots) and the calculated THz beam profile (solid red line) at the frequency labelled by dotted red line in (a). (c) The computed beam waist size of the THz-TDS system in the frequency range of 0.1-1.1THz. The blue solid line shows the theoretical prediction ($w_0 \sim 2.5\lambda$, with $f = 10\text{cm}$ and $D = 5\text{cm}$).

The beam profile of a THz pulse is typically measured by utilizing the knife-edge technique. By placing a non-transparent blade with a sharp rectangular edge in the optical path of the THz beam, part of its transmission is blocked and the rest is measured. The spatial electric field distribution of the THz beam is measured by moving the blade step by step. What we measured is

the integration of the THz beam profile with respect to the position of the blade edge, and the corresponding THz beam profile can be calculated by its differential.

A similar technique can be used to map the THz beam profile by replacing the movable blade with a stationary aperture. By measuring the transmitted electric field with different opening sizes, we can also obtain the THz beam profile. In Figure 7.5(a), I present the experimental results of the beam size measurements of the THz-TDS system used for the optical characterization shown in this thesis. The THz beam profile is calculated by the differential of the measured THz electric field as a function of the aperture opening size. Finally, the waist size of the beam in the THZ-TDS system is estimated to be $\sim 5 - 7\text{mm}$ in the frequency range of 0.1-1.1THz.

I also measured the beam waist size of the CW-THz system which was used for the optical characterization of the waveguide Bragg grating. In this measurement, we followed the steps shown in []. A square metal foil, with sides measuring ~15cm, moves step by step towards the focal point of the parabolic mirror in order to partially block the THz beam. The experimentally measured waist of the beam in the CW-THZ system at different frequencies are shown in Figure 7.5, which is perfectly congruent with the theoretical prediction ($w_0 \sim 2.5\lambda$) estimated at $f = 10\text{mm}$ and $D = 5\text{cm}$.

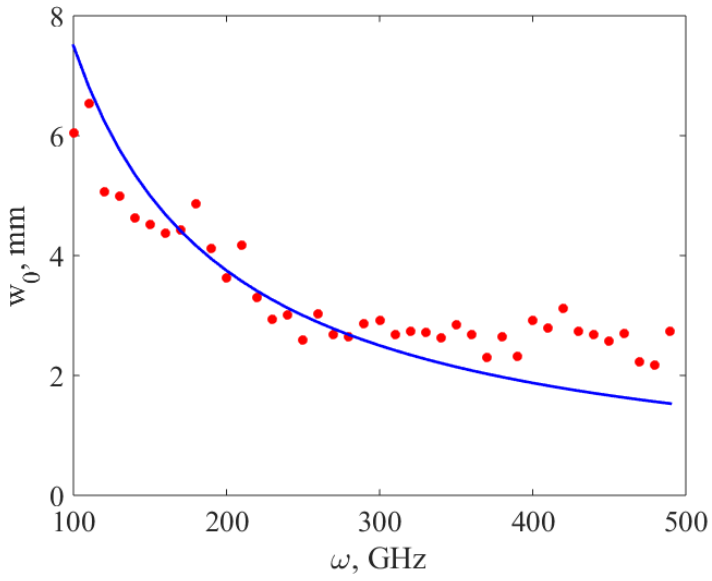

Figure 7.5 The beam waist of the CW-THz system in the frequency range of 100-500GHz. Red dots: the measure beam waist. Blue solid line: the theoretical prediction ($w_0 \sim 2.5\lambda$, with $f = 10\text{mm}$ and $D = 5\text{cm}$).

CHAPTER 8 CONCLUSION AND PERSPECTIVE

In this thesis, I have demonstrated the experimental and theoretical results I obtained in my doctoral study period. In this last chapter, I would like summarize the presented results and highlight some distinctive features of these completed projects.

First, I proposed a novel hollow core waveguide featuring a hyperuniform disordered reflector for applications in the terahertz frequency range. The reflector consists of disorderly positioned dielectric cylinders that are connected with thin dielectric bridges. The center positions of these cylinders follow a hyperuniform disordered point pattern. The proposed reflector structure was further optimized to maximize the photonic bandgap in the vicinity of 0.4THz. Compared with their periodic counterparts with the same refractive index contrast, the proposed hyperuniform reflectors can produce much wider bandgaps. Moreover, it has been shown that hyperuniform reflectors can form a complete bandgap for all polarizations. Further, I proposed two waveguides with different bridge thicknesses (200μm and 250μm) which were fabricated using a 3D stereolithography printer. The optical properties of the fabricated waveguides were numerically investigated using the finite element method, as well as experimentally investigated using THz-TDS spectroscopy. The results confirm that even with sub-optimal structural parameters and a relatively low refractive index contrast (resin/air), the fabricated waveguides still exhibit sizable photonic bandgaps (~15%). The location and the widths of the experimentally measured bandgaps are in agreement with theoretical predictions. Moreover, due to hollow core guidance, the transmission losses (within the bandgap) of the fabricated waveguides are significantly smaller than the bulk absorption loss of the reflector material.

Next, I presented a novel subwavelength graded index porous optical fiber which is specifically designed for applications in the terahertz spectral range (THz GI-mPOF). The radially graded index distribution of the proposed fiber is achieved by an air-hole array featuring deeply subwavelength variable air-hole diameters and inter-hole separations. The simulation results demonstrate that the proposed GI-mPOF design suppresses the excitation of higher order modes and reduces intermodal dispersion. At the same time, both the intermodal and individual dispersion of the designed GI-mPOF are smaller than that of the traditional mPOF, leading to a smaller broadening in the designed graded index fiber. Both transmission and absorption properties of such fibers have been investigated both experimentally using THz-TDS spectroscopy. Experimental

results show that the proposed fiber structure improved the output pulse quality as all the modes reach the output facet of the fiber in one time-domain envelope, and hence the pulse duration is reduced. We also confirmed that the THz pulse broadening in GI-mPOF is considerably smaller than that of the traditional subwavelength porous mPOFs that feature uniform air-hole diameters and inter-hole separations. This characteristic makes these fibers a great asset for THz communications, with GI-mPOFs supporting significantly higher data rates than mPOFs. Moreover, the transmission band of GI-mPOF is significantly wider than that of a porous mPOF due to an enhanced suppression of higher order mode excitation.

Finally, I presented a hollow core waveguide Bragg grating featuring periodically placed triangular axisymmetric slopes on its inner surface. The structure of this waveguide was designed and optimized for dispersion compensation in the vicinity of 140GHz, which required single mode guidance for the HE_{11}-like mode, large negative dispersion, and efficient coupling to the external Gaussian THz beam. Theoretical results showed that the optimized waveguide Bragg grating supports a single mode operation over a spectral range of 137-141GHz. Within this single mode guiding range, the dispersion of the fundamental HE_{11}-like mode can be as large as ~ -130ps/(THz·cm) at 140GHz, while varying in the -500 ~-100 ps/(THz·cm) range over 137-141 GHz. Using a numerically optimized waveguide structure, the prototype of the waveguide Bragg grating was fabricated using a 3D stereolithography system, and was subsequently metallized by applying a silver layer through the use of wet chemistry. The optical properties of the fabricated waveguide Bragg grating were then experimentally measured using terahertz continuous wave spectroscopy. Experimental findings were congruent with the theoretically predicted modal properties, including the spectral positions of high transmission regions and modal dispersion within these regions. I also experimentally mapped the output modal profile at the waveguide output facet using a near field imaging system. The results confirmed a single mode operation in the vicinity of 140GHz, as the output modes featured Gaussian-like profiles in this frequency range. Hence, I concluded that the presented device showed single mode operation, a relatively high coupling efficiency, and strong negative dispersion, which is at least one order of magnitude higher than those of typical THz waveguides, which made the proposed device suitable for dispersion compensation in free-space fiber links used for terahertz communications.

Future research in the area

In this last section, I would like to propose some possibilities for future research effortsrelated to the presented results.

In the chapter 4, I presented a novel hollow core photonic bandgap waveguide with hyperuniform disordered reflectors. As the first attempt, we tried one hyperuniform point pattern with a hyperuniformity of $\chi = 0.5$, and developed it into a 3D hollow core waveguide. For a hyperuniform disordered point pattern, even the same producer will result in total different point patterns, and hence different optical characterizations for the corresponding hollow core waveguides. It is worthy to try other hyperuniform patterns and compare their performances when being developed into 3D waveguides. Also, in the case of planar waveguides, it has been proved the bandgap width can be optimized when the hyperuniformity equal to 0.5. it would be of great benefits if the detailed relationship between the hyperuniformoty and the corresponding bandgap width is studied.

I also covered the management of dispersion using waveguides in the terahertz regime. Using the dispersion reduced graded index optical microstructured fiber (GI-mPOF), it is possible to deliver long distance (several meters) THz radiation. Furthermore, with an appropriately selected length, the proposed waveguide Bragg grating can be used to completely cancel the residual dispersion in a GI-mPOF. Hence, an all-fiber-based THz transmission link can be developed by combining these two waveguides and placing them along a line. This transmission link can be used to deliver THz signals within a moderate length. As the THz signals are guided along a sealed waveguide, the surrounding atmospheric conditions are of little importance. The described all-fiber-based transmission link will be of great importance for THz communications, as it allows access to otherwise physically obstructed areas, and enables compact several mm in diameter communication links with small footprint that can be used as on-chip interconnects

Last but not least, more research into 3D printing of functional THz devices is required in order to achieve printable artificial materials consisting of dielectric and metallic material. As described in this thesis, I attempted to print some tubes with a mixture of copper and resin. However, as the concentration of copper is very small, the printed tubes are still polymeric. To successfully manufacture printable metamaterials, new preparation methods need to be developped.

REFERENCES

1. D. A. Auston, K. P. Cheung, and P. R. Smith, “Picosecond photoconducting Hertzian dipoles,” *Appl. Phys. Lett.*, vol. 45, pp. 284-286, 1984.
2. R. A. Lewis, “A review of terahertz sources,” *J. Phys. D, Appl. Phys*., vol. 47, pp. 374001-1-374001-11, 2014.
3. K. Y. Kim, A. J. Taylor, J. H. Glownia, and G. Rodriguez, “Coherent control of terahertz supercontinuum generation in ultrafast laser—gas interactions,” *Nat. Photon.*, vol. 2, pp. 605-609, 2008.
4. G. K. Kitaeva, “Terahertz generation by means of optical lasers,” *Laser Phys. Lett.*, vol. 5, pp. 559-576, 2008.
5. Y. Chassagneux et al., “Electrically pumped photonic-crystal terahertz lasers controlled by boundary conditions,” Nature, vol. 457, pp. 174-178, 2009.
6. Y. Bai, S. Slivken, S. Kuboya, S. Darvish, and M. Razeghi, “Quantum cascade lasers that emit more light than heat,” *Nat. Photon.*, vol. 4, pp. 99-102, 2010.
7. M. Polini, “Tuning terahertz lasers via graphene plasmons,” Science, vol. 351, pp. 229-231, 2016.
8. Ivan Tretyakov, Sergey Ryabchun, Matvey Finkel, Anna Maslennikova, Natalia Kaurova, Anastasia Lobastova, Boris Voronov, and Gregory Goltsman, “Low noise and wide bandwidth of N_bN hot-electron bolometer mixers,” Appl. Phys. Lett., vol. 98, pp. 033507-1-033507-3, 2011.
9. H. M. Manohara, E. W. Wong, E. Schlecht, B. D. Hunt, and P. H. Siegel, “Carbon Nanotube Schottky Diodes Using Ti−Schottky and Pt−Ohmic Contacts for High Frequency Applications,” Nano Lett., vol. 5, pp. 1469-1474, 2005.
10. L. Vicarelli, M. S. Vitiello, D. Coquillat, A. Lombardo, A. C. Ferrari, W. Knap, M. Polini, V. Pellegrini, and A. Tredicucci, “Graphene field-effect transistors as room-temperature terahertz detectors,” *Nature Mater.*, vol. 11, pp. 865-871, 2012.
11. Y. Kurita, G. Ducournau, D. Coquillat, A. Satou, K. Kobayashi, S. Boubanga Tombet, Y. M. Meziani, V. V. Popov, W. Knap, T. Suemitsu, and T. Otsuji, “Ultrahigh sensitive sub-terahertz detection by InP-based asymmetric dual-grating-gate high-electron-mobility transistors and their broadband characteristics,” *Appl. Phys. Lett.*, vol. 104, pp. 251114-1-251114-4, 2014.

12. I. F. Akyildiz, J. M. Jornet, and C. Han, “Terahertz band: Next frontier for wireless communications,” *Phys. Commun. J.*, vol. 12, pp. 16–32, 2014.
13. T. Nagatsuma, G. Ducournau, and C. C. Renaud, “Advances in terahertz communications accelerated by photonics,” *Nat. Photonics* vol. 10, pp. 371-379, 2016.
14. H. T. Chen, R. Kersting, and G. C. Cho, “Terahertz imaging with nanometer resolution,” *Appl. Phys. Lett.*, vol. 83, pp. 3009-3011, 2003.
15. P. Dean, O. Mitrofanov, J. Keeley, I. Kundu, L. Li, E. H. Linfield, and A. G. Davies, “Apertureless near-field terahertz imaging using the self-mixing effect in a quantum cascade laser,” *Appl. Phys. Lett.*, vol. 108, pp. 091113-1-091113-3, 2016.
16. A. Mazhorova, A. Markov, A. Ng, R. Chinnappan, O. Skorobogata, M. Zourob, and M. Skorobogatiy, “Label-free bacteria detection using evanescent mode of a suspended core terahertz fiber,” *Opt. Express*, vol. 20, pp. 5344-5355, 2012.
17. B. Ng, J. Wu, S. M. Hanham, A. I. Fernández-Domínguez, N. Klein, Y. F. Liew, M. B. H. Breese, M. H. Hong, and S. A. Maier, “Spoof Plasmon Surfaces: A Novel Platform for THz Sensing” *Adv. Opt. Mater*., vol. 1, pp. 543-548, 2013.
18. M. C. Beard, G. M. Turner, and C. A. Schmuttenmaer, “Transient photoconductivity in GaAs as measured by time-resolved terahertz spectroscopy,” *Phys. Rev. B*, vol. 62, pp. 15764-15777, 2000.
19. P. U. Jepsen, D. G. Cooke, and M. Koch, “Terahertz spectroscopy and imaging - modern techniques and applications,” *Laser Photon. Rev.* vol. 5, pp. 124–166, 2011.
20. T. Nagatsuma, S. Horiguchi, Y. Minamikata, Y. Yoshimizu, S. Hisatake, S. Kuwano, N. Yoshimoto, J. Terada, and H. Takahashi, “Terahertz wireless communications based on photonics technologies,” *Opt. Express*, vol. 21, pp. 23736-23747, 2013.
21. S. Koenig, D. Lopez-Diaz, J. Antes1, F. Boes1, R. Henneberger, A. Leuther, A. Tessmann, R. Schmogrow, D. Hillerkuss, R. Palmer, T. Zwick, C. Koos, W. Freude, O. Ambacher, J. Leuthold, and I. Kallfass, “Wireless sub-THz communication system with high data rate,” *Nature Photon.*, vol. 7, pp. 977-981, 2013.
22. F. Pavanello, M. Zaknoune, Y. Yoshimizu, S. Hisatake, J.-F. Lampin, E. Peytavit, G. Ducournau, and T. Nagatsuma, “Coherent Thz communication at 200 Ghz using a frequency comb, UTC-PD and electronic detection,” *Electron. Lett.*, vol. 50, pp. 386–388, 2014.

23. G. Ducournau, P. Szriftgiser, A. Beck, D. Bacquet, F. Pavanello, E. Peytavit, M. Zaknoune, T. Akalin, and J. F. Lampin, "Ultrawide-Bandwidth Single-Channel 0.4-THz Wireless Link Combining Broadband Quasi-Optic Photomixer and Coherent Detection," *IEEE Trans. Terahertz Sci. Technol.*, vol. 4, pp. 328–337, 2014.

24. D. M. Slocum, E. J. Slingerland, R. H. Giles, and T. M. Goyette, "Atmospheric absorption of terahertz radiation and water vapor continuum effects," *J. Quantum Spectrosc. Radiat. Transfer*, vol. 127, pp. 49–63, 2013.

25. K. Tsuruda, M. Fujita, and T. Nagatsuma, "Extremely low-loss terahertz waveguide based on silicon photonic-crystal slab," *Opt. Express*, vol. 23, pp. 31977-31990, 2015.

26. G. P. Agrawal, Lightwave technology: Telecommunication systems, Wiley, 2005.

27. K. Wang and D. Mittleman, "Metal wires for terahertz guiding," *Nature*, vol. 432, pp. 376–379 (2004).

28. J. Zhang, Z. H. Lu, and L. J. Wang, "Precision refractive index measurements of air, N_2, O_2, Ar, and CO_2 with a frequency comb," Appl. Opt., vol. 17, pp. 3143-3251, 2008.

29. Y. Yang, M. Mandehgar, and D. Grischkowsky, "Time domain measurement of the THz refractivity of water vapor," Opt. Express, 20, 26208-26218, 2012.

30. B. Ung, A. Mazhorova, A. Dupuis, M. Rozé, and M. Skorobogatiy, "Polymer microstructured optical fibers for terahertz wave guiding," *Opt. Express*, vol. 19, pp. B848-B861, 2011.

31. K. Nielsen, H. Rasmussen, A. Adam, P. Planken, O. Bang, and P. Jepsen, "Bendable, low-loss Topas fibers for the terahertz frequency range," *Opt. Express*, vol. 17, pp. 8592-8601, (2009).

32. J. Anthony, R. Leonhardt, A. Argyros, and M. C. J. Large, "Characterization of a microstructured Zeonex terahertz fiber," *J. Opt. Soc. Am. B*, vol. 28, pp. 1013–1018, 2011.

33. R. Kashyap, H.-G. Froehlich, A. Swanton, and D. J. Armes, "1.3 m long super-step-chirped fibre Bragg grating with a continuous delay of 13.5 ns and bandwidth 10 nm for broadband dispersion compensation," Electron. Lett. 32, 1807–1809 (1996).

34. K. O. Hill and G. Meltz, "Fiber Bragg Grating Technology Fundamentals and Overview," *J. Lightwave Technol.*, vol. 15, pp. 1263-1276, 1997.

35. K. Kashyap, "Fiber Bragg Gratings," *Academic Press*, 1999.

36. B. J. Eggleton, J. A. Rogers, P. S. Westbook, and T. A. Strasser, “Electrically tunable power efficient dispersion compensation fiber Bragg grating,” *IEEE Photon. Technol. Lett.*, vol. 11, pp. 854–856, 1999.

37. L. Tong, R. R. Gattass, J. B. Ashcom1, S. He, J. Lou, M. Shen, I. Maxwell, and E. Mazur, “Subwavelength-diameter silica wires for low-loss optical wave guiding,” *Nature*, vol. 426, pp. 816-819, 2003.

38. L. J. Chen, H. W. Chen, T. F. Kao, J. Y. Lu, and C. K. Sun, “Low-loss subwavelength plastic fiber for terahertz waveguiding,” *Opt. Lett.*, vol. 31, pp. 308-310, 2006.

39. A. Hassani, A. Dupuis, and M. Skorobogatiy, “Low loss porous terahertz fibers containing multiple subwavelength holes”, *Appl. Phys. Lett.*, vol. 92, pp. 071101-1-071101-3, (2008).

40. A. Dupuis, J. F. Allard, D. Morris, K. Stoeffler, C. Dubois, and M. Skorobogatiy, “Fabrication and THz loss measurements of porous subwavelength fibers using a directional coupler method,” *Opt. Express*, vol. 17, pp. 8012-8028, 2008.

41. S. Atakaramians, S. V. Afshar, B. M. Fischer, D. Abbott, and T. M. Monro, "Porous fibers: a novel approach to low loss THz waveguides," *Opt. Express*, vol. 16, pp. 8845-8854, 2008.

42. A. Dupuis, A. Mazhorova, F. Désévédavy, M. Rozé, and M. Skorobogatiy, “Spectral characterization of porous dielectric subwavelength THz fibers fabricated using a microstructured molding technique,” *Opt. Express*, vol. 18, pp. 13813-13828, 2010.

43. M. Roze, B. Ung, A. Mazhorova, M. Walther, and M. Skorobogatiy, “Suspended core subwavelength fibers: towards practical designs for low-loss terahertz guidance”, *Opt. Express*, vol. 19, pp. 9127-9138, 2011.

44. A. Mazhorova, A. Markov, A. Ng, R. Chinnappan, O. Skorobogata, M. Zourob, and M. Skorobogatiy, “Label-free bacteria detection using evanescent mode of a suspended core terahertz fiber,” *Opt. Express*, vol. 20, pp. 5344-5355, 2012.

45. J. C. Knight, J. Broeng, T. A. Birks, and P. J. Russel, “Photonic band gap guidance in optical fibers,” *Science*, vol. 283, pp. 1476-1478, 1998.

46. J. C. Knight, “Photonic crystal fibres,” *Nature*, vol. 424, pp. 847-851, 2003.

47. L. Vincetti, “Hollow core photonic band gap fiber for THz applications,” Microw. Opt. Technol. Lett., vol. 51, pp. 1711–1714, 2009.

48. R. Islam, G. Hasanuzzaman, S. Habib, S. Rana, and M. Khan, “Low-loss rotated porous core hexagonal single-mode fiber in THz regime,” *Opt. Fiber Technol.*, vol. 24, pp. 38-43, 2015.

49. J. Liang, L. Ren, N. Chen, and C. Zhou, “Broadband, low-loss, dispersion flattened porous-core photonic bandgap fiber for terahertz (THz)-wave propagation,” *Opt. Commun.*, vol. 295, pp. 257–261, 2013.

50. G. Ren, Y. Gong, P. Shum, X. Yu, J. Hu, “Polarization Maintaining Air-core Bandgap Fibers for Terahertz Wave Guiding,” *IEEE J. Quant. Elect.*, vol. 45, pp. 506-513, 2009.

51. K. Nielsen, H. K. Rasmussen, P. U. Jepsen, and O. Bang, “Porous-core honeycomb bandgap THz fiber,” *Opt. Lett.*, vol. 36, pp. 666–668, 2011.

52. H. Bao, K. Nielsen, H. K. Rasmussen, P. U. Jepsen, and O. Bang “Fabrication and characterization of porous-core honeycomb bandgap THz fibers,” *Opt. Express*, vol. 20, pp. 29507–29517, 2012.

53. J. Fan, Y. Li, X. Zhang, M. Hu, L. Chai, and C. Wang., “Predicting mode properties of porous-core honeycomb bandgap THZ fibers by semi-analytical theory,” *J. Lightw. Technol.*, vol. 33, pp. 1931–1936, 2015.

54. M. Skorobogatiy and A. Dupuis, “Ferroelectric all-polymer hollow Bragg fibers for terahertz guidance,” *Appl. Phys. Lett.*, vol. 90, pp. 113514-1-113514-3, 2007.

55. E. Pone, C. Dubois, N. Guo, Y. Gao, A. Dupuis, F. Boismenu, S. Lacroix, and M. Skorobogatiy, “Drawing of the hollow all-polymer Bragg fibers,” *Opt. Express*, vol. 14, pp. 5838- 5852, 2011.

56. D. S. Deng, J.-C. Nave, X. Liang, S. G. Johnson, and Y. Fink, “Exploration of in-fiber nanostructures from capillary instability,” *Opt. Express*, vol. 19, pp. 16273-16290, 2011.

57. B. Ung, A. Dupuis, K. Stoeffler, C. Dubois, M. Skorobogatiy, "High-refractive-index composite materials for terahertz waveguides: trade-off between index contrast and absorption loss," *J. Opt. Soc. Am. B*, vol. 28, pp. 917-921, 2011.

58. A. Dupuis, K. Stoeffler, B. Ung, C. Dubois, and M. Skorobogatiy, "Transmission measurements of hollow-core THz Bragg fibers," *J. Opt. Soc. Am. B*, vol. 28, pp. 896-907, 2011.

59. C. S. Ponseca, R. Pobre, E. Estacio, N. Sarukura, A. Argyros, M. C. Large, and M. A. Eijkelenborg, “Transmission of terahertz radiation using a microstructured polymer optical fiber,” *Opt. Lett.*, vol. 33, pp. 902-904, 2008.

60. A. Hassani, A. Dupuis, andM. Skorobogatiy, “Porous polymer fibers for low-loss Terahertz guiding,” *Opt. Exp.*, vol. 16, pp. 6340-6351, 2008.

61. R. J. Yu, B. Zhang, Y. Q. Zhang, C. Q. Wu, Z. G. Tian, and X. Z. Bai, “Proposal for ultralow loss hollow-core plastic Bragg fiber with cobweb-structured cladding for terahertz waveguiding,” *IEEE Photon. Technol. Lett.*, vol. 19, pp. 910-912, 2007.

62. R. J. Yu, Y. Q. Zhang, B. Zhang, C. R. Wang, and C. Q. Wu, “New cobweb-structure hollow Bragg optical fibers,” *Optoelectronics Lett.*, vol. 3, pp. 10-13, 2007.

63. M. A. Duguay, Y. Kokubun, T. L. Koch, and L. Pfeiffer, “Antiresonant reflecting optical waveguides in SiO_2–Si multilayer structures,” *Appl. Phys. Lett.*, vol. 49, pp. 13-15, 1986.

64. N. M. Litchinitser, A. K. Abeeluck, C. Headley, and B. J. Eggleton, “Antiresonant reflecting photonic crystal optical waveguides,” *Opt. Lett.*, vol. 27, pp. 1592-1594, 2002.

65. C. H. Lai, Y. Hsueh, H. Chen, Y. Huang, H. Chang, and C. Sun, “Low-index terahertz pipe waveguides,” *Opt. Lett.*, vol. 34, pp. 3457-3459, 2009.

66. L. Chen, G. J. Pearce, T. A. Birks, and D. M. Bird, “Guidance in Kagome-like photonic crystal fibres I: analysis of an ideal fibre structure,” Opt. Express, vol. 19, pp. 6945-6956, 2011.

67. Y. Y. Wang, N. V. Wheeler, F. Couny, P. J. Roberts, and F. Benabid, “Low loss broadband transmission in hypocycloid-core Kagome hollow-core photonic crystal fiber,” *Opt. Lett.*, vol. 36, pp. 669–671, 2011.

68. J. Y. Lu, C. P. Yu, H. C. Chang, H. W. Chen, Y. T. Li, C. L. Pan, and C. K. Sun, “Terahertz air-core microstructure fiber,” *Appl. Phys. Lett.*, vol. 92, pp. 2839576-1-2839576-3, 2008.

69. J. Anthony, R. Leonhardt, S. G. Leon-Saval, and A. Argyros, “THz propagation in kagome hollow-core microstructured fibers,” *Opt. Express*, vol. 19, pp. 18470-18478, 2011.

70. D. S. Wu, A. Argyros, and S. G. Leon-Saval, “Reducing the size of hollow terahertz waveguides,” *J. Lightwave Technol.*, vol. 29, pp. 97-103, 2011.

71. L. Vincetti, “Numerical analysis of plastic hollow core microstructured fiber for terahertz applications,” *Opt. Fiber Technol.*, vol. 15, pp. 398-401, 2009.

72. V. Setti, L. Vincetti, and A. Argyros, “Flexible tube lattice fibers for terahertz applications,” Opt. Express, vol. 21, pp. *3388-3399*, 2013.

73. R. W. McGowan, G. Gallot, and D. Grischkowsky, “Propagation of ultra-wideband short pulses of terahertz radiation through submillimeter-diameter circular waveguides,” *Opt. Lett.*, vol. 24, pp. 1431-1433, 1999.

74. G. Gallot, S. P. Jamison, R. W. McGowan, and D. Grischkowsky, “Terahertz waveguides.” J. Opt. Soc. Am. B, vol. 17, pp. 851-863, 2000.

75. B. Bowden, J. A. Harrington, and O. Mitrofanov, “Silver/polystyrene-coated hollow glass waveguides for the transmission of terahertz radiation,” *Opt. Lett.*, vol. 32, pp. 2945-2947, 2007.

76. B. Bowden, J. A. Harrington, and O. Mitrofanov, “Low-loss modes in hollow metallic terahertz waveguides with dielectric coatings,” Appl. Phys. Lett., vol. 93, pp. 181104-1-181104-3, 2008.

77. Y. Matsuura and E. Takeda, “Hollow optical fibers loaded with an inner dielectric film for terahertz broadband spectroscopy,” *J. Opt. Soc. Am. B*, vol. 25, pp. 1949-1954, 2008.

78. O. Mitrofanov, T. Tan, P. R. Mark, B. Bowden, and J. A. Harrington, “Waveguide mode imaging and dispersion analysis with terahertz near-field microscopy,” *Appl. Phys. Lett.*, vol. 94, pp. 171104-1-171104-3, 2009.

79. X. L. Tang, Y. W. Shi, Y. Matsuura, K. Iwai, and M. Miyagi, “Transmission characteristics of terahertz hollow fiber with an absorptive dielectric inner-coating film,” *Opt. Lett.*, vol. 34, pp. 2231-2233, 2009.

80. O. Mitrofanov and J. A. Harrington, “Dielectric-lined cylindrical metallic THz waveguides: mode structure and dispersion,” *Opt. Express*, vol. 18, pp. 1898-1903, 2010.

81. X. Tang, Z. Yu, X. Tu, J. Chen, A. Argyros, B. T. Kuhlmey, and Y. Shi, “Elliptical metallic hollow fiber inner-coated with non-uniform dielectric layer,” *Opt. Express*, vol. 23, pp. 22587-22601, 2015.

82. M. Miyagi and S. Kawakami, “Design theory of dielectric-coated circular metallic waveguides for infrared transmission,” *J. Lightwave Technol.*, vol. 2, pp. 116-126, 1984.

83. K. Wang and D. Mittleman, “Metal wires for terahertz guiding,” *Nature*, vol. 432, pp. 376–379 (2004).

84. V. Astley, J. Scheiman, R. Mendis, and D. M. Mittleman, “Bending and coupling losses in terahertz wire waveguides,” *Opt. Lett.*, vol. 35, pp. 553-555, 2010.

85. M. Mbonye, R. Mendis, and D. Mittleman, “A terahertz two-wire waveguide with low bending loss,” *Appl. Phys. Lett.*, vol. 95, pp. 233506-1-233506-3 (2009).

86. H. Pahlevaninezhad, T. E. Darcie, and B. Heshmat, “Two-wire waveguide for terahertz,” *Opt. Express*, vol. 18, pp. 7415–7420, 2010.

87. H. Pahlevaninezhad, T. E. Darcie, and B. Heshmat, “Coupling of terahertz waves to a two-wire waveguide,” *Opt. Express*, vol. 18, pp. 22614–22624, 2010.

88. A. Markov, M. Skorobogatiy, “Two-wire terahertz fibers with porous dielectric support,” *Opt. Express*, vol. 21, pp. 12729-12743, 2013.

89. A. Markov and M. Skorobogatiy, “Hybrid plasmonic terahertz fibers for sensing applications,” *Appl. Phys. Lett.*, vol. 103, 181118, 2013.

90. A. Markov, H. Guerboukha, A. Argyros, and M. Skorobogatiy, “A complementary study to ‘Hybrid hollow core fibers with embedded wires as THz waveguides’ and ‘Two-wire terahertz fibers with dielectric support’, comment,” *Opt. Express*, vol. 21, pp. 27802-27803, 2013.

91. M. K. Mridha, A. Mazhorova, M. Clerici, I. Al-Naib, M. Daneau, X. Ropagnol, M. Peccianti, C. Reimer, M. Ferrera, L. Razzari, F. Vidal, and R. Morandotti, “Active terahertz two-wire waveguides,” Opt. Express, vol. 22, pp. 22340-22348, 2014.

92. H. Gao, Q. Cao, D. Teng, M. Zhu, and K. Wang, “Perturbative solution for terahertz two-wire metallic waveguides with different radii,” *Opt. Express*, vol. 23, pp. 27457-27473, 2015.

93. J. Anthony, R. Leonhardt, and A. Argyros, “Hybrid hollow core fibers with embedded wires as THz waveguides,” *Opt. Express*, vol. 21, pp. 2903-2912, 2013.

94. N. Yudasari, J. Anthony, and R. Leonhardt, “Terahertz pulse propagation in 3D-printed waveguide with metal wires component,” *Opt. Express*, vol. 22, pp. 26042-26054, 2014.

95. H. Li, S. Atakaramians, R. Lwin, X. Tang, Z. Yu, A. Argyros, and B. T. Kuhlmey, “Flexible single-mode hollow-core terahertz fiber with metamaterial cladding,” *Optica*, vol. 3, pp. 941-947, 2016.

96. S. Atakaramians, A. Argyros, S. C. Fleming, and B. T. Kuhlmey, “Hollow core waveguides with uniaxial metamaterial cladding: modal equations and guidance conditions,” *J. Opt. Soc. Am. B*, vol. 29, pp. 2462–2477, 2012.

97. H. Li, S. Atakaramians, R. Lwin, X. Tang, Z. Yu, A. Argyros, and B. T. Kuhlmey, “Flexible single-mode hollow-core terahertz fiber with metamaterial cladding,” *Optica*, vol. 3, pp. 941-947, 2016.

98. H. Li, G. Ren, S. Atakaramians, B. T. Kuhlmey, and S. Jian, “Linearly polarized single TM mode terahertz waveguide,” *Opt. Lett.*, vol. 41, pp. 4004-4007, 2016.

99. J. C. Knight, T. A. Birks, P. St. J. Russell, and D. M. Atkin, “All-silica single-mode optical fiber with photonic crystal cladding,” *Opt. Lett.*, vol. 21, pp. 1547-1549, 1996.

100. P. J. Russel, “Photonic Crystal Fibers,” *Science*, vol. 299, pp. 358-362, 2003.

101. D. Mogilevtsev, T. Birks, and P. Russell, “Group-velocity dispersion in photonic crystal fibers,” *Opt. Lett.*, vol. 23, pp. 1662-1664, 1998.

102. J. Broeng, D. Mogilevstev, S. E. Barkou, A. Bjarklev, “Photonic Crystal Fibers: A New Class of Optical Waveguides,” *Opt. Fiber Technol.*, vol. 5, pp. 305-330, 1999.

103. A. Ferrando, E. Silvestre, and P. Andres, “Designing the properties of dispersion-flattened photonic crystal fibers,” *Opt. Express*, vol. 9, pp. 687-697, 2001.

104. K. Saitoh, M. Koshiba, T. Hasegawa, and E. Sasaoka, “Chromatic dispersion control in photonic crystal fibers: application to ultra-flattened dispersion,” *Opt. Express*, vol. 11, pp. 843-852, 2003.

105. T. L. Wu and C. H. Chao, “A novel ultraflattened dispersion photonic Crystal fiber,” *IEEE Photonics Technol. Lett.*, vol. 17, pp. 67-69, 2004.

106. F. Poletti, V. Finazzi, T. Monro, N. Broderick, V. Tse and D. Richardson, “Inverse design and fabrication tolerances of ultra-flattened dispersion holey fibers,” *Opt. Express*, vol. 13, pp. 3728-3736, 2005.

107. K. P. Hansen, “Dispersion flattened hybrid-core nonlinear photonic crystal fiber,” *Opt. Express*, vol. 11, pp. 1503-1509, 2003.

108. K. Saitoh, N. Florous, and M. Koshiba, “Ultra-flattened chromatic dispersion controllability using a defected-core photonic crystal fiber with low confinement losses,” *Opt. Express*, vol. 13, pp. 8365-8371, 2005.

109. M. Skorobogatiy and N. Guo, “Bandwidth enhancement by differential mode attenuation in multimode photonic crystal Bragg fibers,” *Opt. Lett.*, vol. 32, pp. 900-902, 2007.

110. R. Olshansky and D. B. Keck, “Pulse broadening in graded-index optical fibers,” *Appl. Opt*., vol. 15, pp. 483-491, 1976.

111. K. Miura, J. Qiu, H. Inouye, T. Mitsuyu, and K. Hirao, “Photowritten optical waveguides in various glasses with ultrashort pulse laser,” *Appl. Phys. Lett*., vol. 71, pp. 3329-3331, 1997.

112. Y. Koike, “High-bandwidth graded-index polymer optical fiber,” *Polymer*, vol. 32, pp. 1737-1745, 1991.

113. Y. Koike, T. Ishigure, E. Nihei, “High-bandwidth graded-index polymer optical fiber,” *J. Lightwave Technol.*, vol. 13, pp. 1475–1489, 1995.

114. G. Giaretta, W. White, M. Wegmuller, and T. Onishi, “High-Speed (11 Gbit/s) Data Transmission Using Perfluorinated Graded-Index Polymer Optical Fibers for Short Interconnects (<100 m),” *IEEE Photon. Technol. Lett.*, vol. 12, pp. 347 – 349, 2000.

115. Y. Akimoto, M. Asai, K. Koike, K. Makino, and Y. Koike, “Poly(styrene)-based graded-index plastic optical fiber for home networks,” *Opt. Lett.*, vol. 37, pp. 1853-1855, 2012.

116. R. Lwin, G. Barton, L. Harvey, J. Harvey, D. Hirst, S. Manos, M. C. J. Large, L. Poladian, A. Bachmann, H. Poisel, and K.-F. Klein, “Beyond the bandwidth-length product: Graded index microstructured polymer optical fiber,” *Appl. Phys. Lett*., vol. 91, pp. 191119-1-191119-3 (2007).

117. C. Lin, H. Kogelnik, and L. Cohen, “Optical-pulse equalization of low-dispersion transmission in single-mode fibers in the 1.3-1.7μm spectral region,” *Opt. Lett.*, vol. 5, pp. 476-478, 1980.

118. U. Peschel, T. Peschel, and F. Lederer, “A compact device for highly efficient dispersion compensation in fiber transmission,” *Appl. Phys. Lett.*, vol. 16, pp. 2111-2113, 1995.

119. F. Gérôme, J. Auguste, J. Maury, J. Blondy, and J. Marcou, ‘Theoretical and Experimental Analysis of a Chromatic Dispersion Compensating Module Using a Dual Concentric Core Fiber,’ *J. Lightwave. Technol*., vol. 24, pp. 442-448, 2006.

120. V. Rastogi, R. Kumar, and A. Kumar, “Large effective area all-solid dispersion compensating fiber,” *J. Opt.*, vol. 13, pp. 125707-1-125707-6, 2011.

121. C. Poole, J. Wiesenfeld, and A. McCormick, “Broadband dispersion compensation by using the higher-order spatial mode in a two-mode fiber,” *Opt. Lett.*, vol. 17, pp. 985-987, 1992.

122. C. Poole, J. Wiesenfeld, and D. DiGiovanni, ‘Elliptical-Core Dual-Mode Fiber Dispersion Compensator,’ *IEEE Photonic Tech. Lett.*, vol. 5, pp. 194-197, 1993.

123. A. M. Vengsarkar and W. A. Reed, “Dispersion-compensating single-mode fibers: efficient designs for first- and second-order compensation,” *Opt. Lett.*, vol. 18, pp. 924-926, 1993.

124. F. Gérôme, J. L. Auguste, and J. M. Blondy, “Design of dispersion compensating fibers based on a dual-concentric-core photonic crystal fiber,” *Opt. Lett.*, vol. 29, pp. 2725–2727, 2004.

125. T. Fujisawa, K. Saitoh, K. Wada, and M. Koshiba, “Chromatic dispersion profile optimization of dual-concentric-core photonic crystal fibers for broadband dispersion compensation,” *Opt. Express*, vol. 14, pp. 893-900, 2006.

126. F. Gérôme, J. L. Auguste, and J. M. Blondy, “Design of dispersion-compensating fibers based on a dual-concentric-core photonic crystal fiber,” *Opt. Lett.*, vol. 29, pp. 2725-2727, 2004.

127. X. Zhao, G. Zhou, S. Li, Z. Liu, D. Wei, Z. Hou, and L. Hou, “Photonic crystal fiber for dispersion compensation,” *Appl. Opt.*, vol. 47, pp. 5190-5196, 2008.

128. D. C. Zografopoulos, C. Vázquez, E. E. Kriezis, and T. V. Yioultsis, “Dual-core photonic crystal fibers for tunable polarization mode dispersion compensation,” *Opt. Express*, vol. 19, pp. 21680-21691, 2011.

129. D. Modotto, M. Andreana, K. Krupa, G. Manili, U. Minoni, A. Tonello, V. Couderc, A. Barthélémy, A. Labruyère, B. M. Shalaby, P. Leproux, S. Wabnitz, and A. B. Aceves, “Efficiency of dispersive wave generation in dual concentric core microstructured fiber,” *J. Opt. Soc. Am. B*, vol. 32, pp. 1676-1685, 2015.

130. T. A. Birks, D. Mogilevtsev, J. C. Knight, and P. J. Russell, “Dispersion Compensation Using Single-Material Fibers,” *IEEE Photon. Technol. Lett.*, vol. 11, pp. 674-676, 1999.

131. L. P. Shen, W. P. Huang, G. X. Chen, and S. S. Jian, “Design and Optimization of Photonic Crystal Fibers for Broad-Band Dispersion Compensation,” *IEEE Photon. Technol. Lett.*, 15, 540-542, 2003.

132. E. Silvestre, T. Pinheiro-Ortega, P. Andrés, J. J. Miret, and Á. Coves, “Differential toolbox to shape dispersion behavior in photonic crystal fibers,” *Opt. Lett.*, vol. 31, pp. 1190-1192, 2006.

133. S. Yang, Y. Zhang, L. He, and S. Xie, “Broadband dispersion-compensating photonic crystal fiber,” *Opt. Lett.*, vol. 31, pp. 2830-2832, 2006.

134. A. Islam and S. Alam, “Design Optimization of Equiangular Spiral Photonic Crystal Fiber for Large Negative Flat Dispersion and High Birefringence,” *J. Lightwave Technol.*, vol. 30, pp. 3545-3551, 2012.

135. D. C. Tee, M. H. Bakar, and N. Tamchek, “Photonic crystal fiber in photonic crystal fiber for residual dispersion compensation over E + S + C + L + U wavelength bands,” *IEEE Photon. J.*, vol. 5, 2013.

136. R. Hasan, S. Anower, and I Hasan, “A Polarization Maintaining Single-Mode Photonic Crystal Fiber for Residual Dispersion Compensation,” *IEEE Photon. Technol. Lett.*, vol. 28, pp. 1782-1785, 2016.

137. J. Marcou, F. Brechet and P. H. Roy, “Design of weakly guiding Bragg fibres for chromatic dispersion shifting towards short wavelengths,”

138. G. Ouyang, Y. Xu, and A. Yariv, “Theoretical study on dispersion compensation in air-core Bragg fibers,” *Opt. Express*, vol. 10, pp. 899–908, 2002.

139. S. Dasgupta, B. Pal, and M. Shenoy, “Design of dispersion-compensating Bragg fiber with an ultrahigh figure of merit,” *Opt. Lett*., vol. 30, pp. 1917-1919, 2005.

140. S.G. Johnson, M. Ibanescu, M. Skorobogatiy, O. Weiseberg, T.D. Engeness, M. Soljacic, S.A. Jacobs, J.D. Joannopoulos, and Y. Fink, “Low-Loss Asymptotically Single-Mode Propagation in Large Core OmniGuide Fibers,” *Opt. Express*, vol. 9, pp. 748-779, 2001.

141. T. D. Engeness, M. Ibanescu, S. G. Johnson, O. Weisberg, M. Skorobogatiy, S. Jacobs, and Y. Fink, “Dispersion tailoring and compensation by modal interactions in OmniGuide fibers,” *Opt. Express*, vol. 11, pp. 1175-1198, 2003.

142. B. J. Eggleton, R. E. Slusher, C. M. de Sterke, P. A. Krug, and J. E. Sipe, “Bragg Grating Solitons,” *Phys. Rev. Lett.*, vol. 76, pp. 1627-1637, 1996.

143. A. Othonos, “Fiber Bragg Gratings,” *Rev Sci. Instrum.*, vol. 68, pp. 4309-4341, 1997.

144. Z. Wei, H. M. H. Shalaby, H. Ghafouri-Shiraz, “Modified quadratic congruence codes for fiber Bragg-grating-based spectral-amplitude-coding optical CDMA systems,” *J. Lightwave Technol.*, vol. 19, pp. 1274-1281, 2002.

145. F. Ouellette, “Dispersion cancellation using linearly chirped Bragg grating filters in optical waveguides,” *Opt. Lett.*, vol. 12, pp. 847-849, 1987.

146. K. O. Hill, F. Bilodeau, B. Malo, T. Kitagawa, S. Thériault, D. C. Johnson, J. Albert, and K. Takiguchi, “Chirped in-fiber Bragg gratings for compensation of optical-fiber dispersion,” *Opt. Lett.*, vol. 19, pp. 1314-1316, 1994.

147. J. Lauzon, S. Thibault, J. Martin, and F. Ouellette, “Implementation and characterization of fiber Bragg gratings linearly chirped by a temperature gradient,” *Opt. Lett.*, vol. 19, pp. 2027-2029, 1994.

148. K. M. Feng, J. X. Chai, V. Grubsky, D. S. Starodubov, M. I. Hayee, S. Lee, X. Jiang, A. E. Willner, J. Feinberg, “Dynamic dispersion compensation in a 10-Gb/s optical system using a novel voltage tuned nonlinearly chirped fiber Bragg grating,” *IEEE Photon. Technol. Lett.*, vol. 16, pp. 849-851, 2004.

149. N. M Litchinitser, B. J. Eggleton, D. B. Patterson, “Fiber Bragg gratings for dispersion compensation in transmission: theoretical model and design criteria for nearly ideal pulse recompression,” *J. Lightwave Technol.*, vol. 8, pp. 1303-1313, 1997.

150. B. Ortega, J. L. Cruz, J. Capmany, M. V. Andres, D. Pastor, “Analysis of a microwave time delay line based on a perturbed uniform fiber Bragg grating operating at constant wavelength,” *J. Lightwave Technol.*, vol. 18, pp. 430-436, 2000.

151. S. Pandey, B. Gupta, and A. Nahata, “Terahertz plasmonic waveguides created via 3D printing,” *Opt. Express*, vol. 21, pp. 24422-24430, 2013.

152. N. Yudasari, J. Anthony, and R. Leonhardt, “Terahertz pulse propagation in 3D-printed waveguide with metal wires component,” *Opt. Express*, vol. 22, pp. 26042-26054, 2014.

153. K. Cook, J. Canning, S. Leon-Saval, Z. Reid, M. A. Hossain, J. E. Comatti, Y. H. Luo, and G. D. Peng, “Air-structured optical fiber drawn from a 3D-printed preform,” *Opt. Lett.*, 2015.

154. J. Pyo, J. T. Kim, J. Lee, J. Yoo, and J. Ho, “3D Printed Nanophotonic Waveguides,” *Adv. Opt. Mater.*, vol. 4, pp. 1190-1195, 2016.

155. P. F. Jacobs, Rapid prototyping and manufacturing: fundamentals of stereolithography, *The Society of Manufacturing Engineers*, 1992.

156. F. P. W. Melchels, J. Feijen, D. W. Grijpma, "A review on stereolithography and its applications in biomedical engineering," *Biomaterials*, vol. 31, pp. 6121–6130, 2010.

157. M. Skorobogatiy, Nanostructured and Subwavelength Waveguides: fundamentals and applications, *Wiley*, 2012.

158. A. Markov, A. Mazhorova, M. Skorobogatiy, "Planar porous THz waveguides for low-loss guidance and sensing applications," *IEEE Trans. Terahertz Sci. Technol.*, vol. 3, pp. 96-102, 2013.

159. H. H. Rose, Geometrical Charged-Particle Optics, *Springer*, 2009.

160. A. Roggenbuck, K. Thirunavukkuarasu, H. Schmitz, J. Marx, A. Deninger, I. C. Mayorga, R. Güsten, J. Hemberger, and M. Grüninger, "Using a fiber stretcher as a fast phase modulator in a continuous wave terahertz spectrometer," *J. Opt. Soc. Am. B*, vol. 29, pp. 614-620, 2012.

161. T. Ma, H. Guerboukha, M. Girard, A.D. Squires, R.A. Lewis, and M. Skorobogatiy, "3D Printed Hollow-Core Terahertz Optical Waveguides with Hyperuniform Disordered Dielectric Reflectors," *Advanced Optical Materials*, vol. 4, pp. 1-10, 2016. DOI: 10.1002/adom. 201600171

162. E. Yablonovitch, "Inhibited Spontaneous Emission in Solid-State Physics and Electronics," *Phys. Rev. Lett.*, vol. 58, pp. 2059-2062, 1987.

163. P. J. Russell, "Photonic-Crystal Fibers," *J. Lightwave Technol.*, vol. 24, pp. 4729-4749, 2006.

164. M. Florescu, S. Torquato, and P. J. Steinhardt, "Designer disordered materials with large, complete photonic band gaps," *Proc. Natl. Acad. Sci.*, vol. 106, pp. 20658- 20663, 2009.

165. K. Vynck, M. Burresi, F. Riboli, and D. S. Wiersma, "Photon management in two-dimensional disordered media," *Nat. Mater.*, vol. 11, pp. 1017-1022, 2012.

166. T. Amoah, and M. Florescu, "High-Q optical cavities in hyperuniform disordered materials," *Phys. Rev. B*, vol. 91, pp. 020201, 2015.

167. W. Man, M. Florescu, E. P. Williamson, Y. He, S. R. Hashemizad, B. Y.C. Leung, D. R. Liner, S. Torquato, P. M. Chaikin, and P. J. Steinhardt, "Isotropic band gaps and freeform waveguides observed in hyperuniform disordered photonic solids," *Proc. Natl. Acad. Sci.*, vol. 110, pp. 15886-15891, 2013.

168. W. Man, M. Florescu, K. Matsuyama, P. Yadak, G. Nahal, S. Hashemizad, E. Williamson, P. Steinhardt, S. Torquato, and P. Chaikin, "Photonic band gap in isotropic hyperuniform disordered solids with low dielectric contrast," *Opt. Express*, vol. 21, pp. 19972-19981, 2013.

169. S. Tsitrin, E. P. Williamson, T. Amoah, G. Nahal, H. L. Chan, M. Florescu, and W. Man, "Unfolding the band structure of non-crystalline photonic band gap materials," *Sci. Rep.*, vol. 5, pp. 13301, 2015.

170. R. D. Batten, F. H. Stillinger, and S. Torquato, "Classical disordered ground states: Super-ideal gases and stealth and equi-luminous materials," *J. Appl. Phys.*, vol. 104, pp. 033504, 2008.

171. S. Torquato and F. H. Stillinger, "Local density fluctuations, hyperuniformity, and order metrics," *Phys. Rev. E*, vol. 68, pp. 041113, 2003.

172. A. D. Squires, E. Constable, and R. A. Lewis, "3D printed terahertz diffraction gratings and lenses," *J. Infrared. Milli. Terahz. Wave*, vol. 36, pp. 72, 2015.

173. M. Naftaly, "Metrology Issues and Solutions in THz Time-Domain Spectroscopy: Noise, Errors, Calibration," *IEEE Sensors J.*, vol. 13, pp. 8-17, 2013.

174. J. Li, H. Qu, and M. Skorobogatiy, "Squeezed hollow-core photonic Bragg fiber for surface sensing applications," *Opt. Express*, vol. 24, pp. 15687-15701, 2016.

175. S. Wu, C. Yang, W. Hsu, L. Lin, "3D-Printed Microelectronics for Integrated Circuitry and Passive Wireless Sensors," *Microsys. & Micro. Eng.*, vol. 1, pp. 1501310-1-1501310-1, 2015.

176. S. Pandey, B. Gupta, and A. Nahata, "Terahertz plasmonic waveguides created via 3D printing," *Opt. Express*, vol. 21, pp. 24422-24430, 2013.

177. N. Yudasari, J. Anthony, and R. Leonhardt, "Terahertz pulse propagation in 3D-printed waveguide with metal wires component," *Opt. Express* vol. 22, pp. 26042-26054, 2014.

178. J. Lu, C. Yu, H. Chang, H. Chen, Y. Li, C. Pan, and C. Sun, “Terahertz air-core microstructure fiber,” *Appl. Phys. Lett.*, vol. 92, pp. 064105-1-064105-3, 2008.

179. T. Ma, A. Markov, L. Wang, M. Skorobogatiy, “Graded index porous optical fibers – dispersion management in terahertz range,” *Opt. Express*, vol. 23, pp. 7856-7869, 2015.

180. J. Wang, X. H. Yang, L. L. Wang, “Fabrication and experimental observation of monolithic multi-air-core fiber array for image transmission,” *Opt. Express*, vol. 16, pp. 7703-7708, 2008.

181. T. Ma, A. Markov, L. Wang, M. Skorobogatiy, “Graded index porous optical fibers – dispersion management in terahertz range,” *Optics Express*, vol. 23, pp. 7856-7869, 2015.

182. M. Cho, J. Kim, H. Park, Y. Han, K. Moon, E. Jung, and H. Han, “Highly birefringent terahertz polarization maintaining plastic photonic crystal fibers,” *Opt. Express*, vol. 16, pp. 7–12, 2008.

183. H. Han, H. Park, M. Cho, and J. Kim, “Terahertz pulse propagation in a plastic photonic crystal fiber,” *Appl. Phys. Lett.*, vol. 80, pp. 2634-1-2634-3, 2002.

184. I. P. Kaminow, T. Li, and A. E. Willner, Optical Fiber Telecommunications Volume VIA: Components and Subsystems, *Academic Press*, 2013.

185. G. Fiol, J. A. Lott, N. N. Ledentsov, and D. Bimberg, “Multimode optical fibre communication at 25 Gbit/s over 300 m with small spectral-width 850 nm VCSELS,” *Electron. Lett.*, vol. 47, pp. 810–811, 2011.

186. J. D. Downie, J. E. Hurley, D. V. Kuksenkov, C. M. Lynn, A. E. Korolev, and V. N. Nazarov, “Transmission of 112 Gb/s PM-QPSK signals over up to 635 km of multimode optical fiber,” *Opt. Express*, vol. 19, pp. B363–B369, 2011.

187. D. S. Montero and C. Vázquez, “Analysis of the electric field propagation method: theoretical model applied to perfluorinated graded-index polymer optical fiber links,” *Opt. Lett.*, vol. 36, pp. 4116–4118, 2011.

188. M. A. Illarramendi, J. Arrue, I. Ayesta, F. Jiménez, J. Zubia, I. Bikandi, A. Tagaya, and Y. Koike, “Amplified spontaneous emission in graded-index polymer optical fibers: theory and experiment,” *Opt. Express*, vol. 21, pp. 24254–24266, 2013.

189. Y. Yang, M. Mandehgar, and D. Grischkowsky, “Understanding THz pulse transmission in the atmosphere,” *IEEE Trans. THz Sci. Technol.*, vol. 2, pp. 406–415, 2012.

190. Y. Yang, M. Mandehgar, and D. Grischkowsky, “Time domain measurement of the THz refractivity of water vapor,” *Opt. Express*, vol. 20, pp. 26208-26218, 2012.

191. J. D. Jackson, Classical Electrodynamics, *John Wiley*, 1999.

192. *T. Hattori, R. Rungsawang, K. Ohta and K. Tukamoto, “Gaussian Beam Analysis of Temporal Waveform of Focused Terahertz Pulses,” J. Appl. Phys., vol. 41, pp. 5198-5204, 2002.*

193. S. Jiang, E. Newton, C. Yuen, and C. Kan, “Chemical silver plating on cotton and polyester fabrics and its application on fabric design, *Text. Res. J.*, 76, 57–65, 2006.

194. H. H. Rose, Geometrical Charged-Particle Optics, *Springer*, 2009.

195. C. Tuck, Effective Medium Theory: Principles and Applications, *Oxford University Press*, 1999.

196. M. Naftaly, “Metrology issues and solutions in THz time-domain spectroscopy: Noise, errors, calibration,” *IEEE Sensors J.*, vol. 13, no. 1, pp. 8–17, 2013.